THESIS FOR THE DEGREE OF DOCTOR OF PHILOSOPHY

Design and Characterisation of Terahertz Schottky Barrier Diode Mixers

Divya Jayasankar

Terahertz and Millimetre wave Laboratory
Department of Microtechnology and Nanoscience - MC2
Chalmers University of Technology
Gothenburg, Sweden, 2024

Design and Characterisation of Terahertz Schottky Barrier Diode Mixers

Divya Jayasankar
ORCID: 0000-0002-5726-327X

ISBN 978-91-8103-131-7
Doktorsavhandlingar vid Chalmers tekniska högskola
Ny serie nr: 5589
ISSN 0346-718X
Acknowledgements, dedications, and similar personal statements in this thesis, reflect the author's own views.

This thesis has been prepared using LaTeX.
Terahertz and Millimetre wave Laboratory
Department of Microscience and Nanotechnology - MC2
Chalmers University of Technology
SE-412 96 Gothenburg, Sweden
Phone: +46 (0)31 772 1000
www.chalmers.se

Cover picture: (Left) Experimental setup for characterising 3.5/4.7-THz harmonic mixer, (Centre) Broadband conversion loss measurement setup for THz harmonic mixers, (Right) Near-field THz antenna measurement setup.

Printed by Chalmers Reproservice
Gothenburg, Sweden, November 2024

To my Amma, Appa - Balasaraswathy & Jayasankar

Abstract

Efficient and compact terahertz frequency converters operating at ambient temperatures are essential for long lifetime space/air-borne missions. Yet, realising mixers in the 3–5 THz range remains challenging due to the lack of stable local oscillator sources, complexities in circuit fabrication, and the need for high-precision machining of E-plane split blocks.

This dissertation addresses these challenges with a focus on developing 3.5-THz and 4.7-THz harmonic and fundamental mixers. First, the effect of idler terminations on the harmonic mixer's performance was evaluated. Based on this theoretical study, 3.5-THz, $\times$6-harmonic mixers were designed, featuring a planar, single-ended Schottky-barrier diode with a sub-micron anode on a 2-μm GaAs membrane. The mixers exhibited a conversion loss of 60 dB at 3.5 THz and 76 dB at 4.7 THz. This was followed by a successful demonstration of phase-locking of quantum-cascade lasers, representing the state-of-the-art wide-band harmonic mixers using planar diodes in the 3-5 THz range.

In addition, this research focused on the design and experimental characterisation of 3.5-THz and 4.7-THz fundamental mixers. The initial video detection and noise temperature measurements indicated significant losses and poor RF coupling. To address these issues, a scaled-down experiment was performed to analyse the impact of E-plane misalignment on diagonal horn antennas in the WM-570 frequency band. An E-plane misalignment of approximately 8% of the wavelength led to a 3-dB degradation in the optical coupling to a Gaussian beam (Gaussicity) in the middle of the waveguide band. Based on this, an optimised design for a 4.7-THz, $\times$8-harmonic mixer with an integrated pyramidal horn, less susceptible to E-plane asymmetry, is presented. Finally, an alternate measurement technique which enables broadband characterisation of THz harmonic mixers is demonstrated. These results represent the first broadband characterisation of THz harmonic mixers from 2.2 to 3 THz.

This thesis presents essential findings that will enable the realisation of THz heterodyne receivers for detecting atomic and molecular species such as hydroxyl radical (OH) and atomic oxygen (OI), which are crucial for atmospheric and planetary science research.

Keywords: Harmonic mixers, Heterodyne receivers, Horn antennas, Phase locking, Schottky-barrier diodes, Terahertz electronics.

List of Publications

This thesis is based on the following papers:

[A] **D. Jayasankar**, J. Stake and P. Sobis, "Effect of Idler Terminations on the Conversion Loss for THz Schottky Diode Harmonic Mixers," in Proceedings of the *44th Int. Conf. on Infrared, Millimeter, and Terahertz waves (IRMMW-THz)*, Paris, Sep. 2019, pp. 1-2, DOI: 10.1109/IRMMW-THz.2019.8873938.

[B] **D. Jayasankar**, V. Drakinskiy, N. Rothbart, H. Richter, X Lü, L Schrottke, H T. Grahn, M. Wienold, H-W. Hübers, P. Sobis, and J. Stake, "A 3.5-THz, ×6-Harmonic, Single-Ended Schottky Diode Mixer for Frequency Stabilization of Quantum-Cascade Lasers," *IEEE Transactions on Terahertz Science and Technology*, vol. 11, no. 6, pp. 684-694, Nov. 2021, DOI: 10.1109/TTHZ.2021.3115730.

[C] **D. Jayasankar**, T. Reck, S. Durant, J. Stake and J. Hesler, "A Broadband Conversion Loss Measurement Technique for Terahertz Harmonic Mixers", in *IEEE Transactions on Terahertz Science and Technology*, vol. 14, no. 3, pp. 424-427, May 2024, DOI: 10.1109/TTHZ.2024.3368660.

[D] **D. Jayasankar**, N. Rothbart, H. Richter, V. Drakinskiy, P. Sobis, H.-W. Hübers and J. Stake "Design and Characterisation of a 3.5-THz Fundamental Schottky Mixers", in Proceedings of the *32nd Int. Symp. on Space Terahertz Technology (ISSTT)*, Baeza, Oct. 2022.

[E] **D. Jayasankar**, J. Hesler, A. Koj, and J. Stake, "Impact of E-plane Misalignment on THz Diagonal Horns," *IEEE Transactions on Terahertz Science and Technology*, Aug. 2024, DOI: 10.1109/TTHZ.2024.3368660.

[F] **D. Jayasankar**, N. Rothbart, H.-W. Hübers and J. Stake "4.7-THz Schottky Diode Harmonic Mixer: Design, Fabrication, and Performance Optimization", in Proceedings of the *33rd Int. Symp. on Space Terahertz Technology (ISSTT)*, Charlottesville, USA, Apr. 2024.

The following papers are not included since the content overlaps or is beyond the scope of this thesis:

[a] H. Richter, N. Rothbart, M. Wienold, X Lü, L Schrottke, H T. Grahn, **D. Jayasankar**, V. Drakinskiy, P. Sobis, J. Stake, and H-W. Hübers, "Phase-Locking of Quantum-Cascade Lasers Operating Around 3.5 THz and 4.7 THz With a Schottky-Diode Harmonic Mixer", *IEEE Transactions on Terahertz Science and Technology*, vol. 14, no. 3, pp. 346-353, May 2024, DOI:10.1109/TTHZ.2024.3385379.

[b] R. Voigt, M. Wienold, **D. Jayasankar**, V. Drakinskiy, J. Stake, P. Sobis, L. Schrottke, X. Lü, H. T. Grahn, and H.-W. Hübers, "Frequency stabilization of a terahertz quantum-cascade laser to the Lamb dip of a molecular absorption line," *Opt. Express 31*, pp. 13888-13894, Apr. 2023. DOI: 10.1364/OE.483883

[c] **D. Jayasankar**, V. Drakinskiy, P. Sobis and J. Stake, "A 4.7-THz fundamental Schottky diode mixer", in Proceedings of the *47th Int. Conf. on Infrared, Millimeter, and Terahertz waves (IRMMW-THz)*, Delft, Aug. 2022, pp. 1-2, DOI: 10.1109/IRMMW-THz50927.2022.9895685.

[d] **D. Jayasankar**, V. Drakinskiy, P. Sobis, and J. Stake, "Development of Supra-THz Schottky Diode Harmonic Mixers," in proceedings of the *46th Int. Conf. on Infrared, Millimeter, and Terahertz waves (IRMMW-THz)*, Chengdu, Sep. 2021, DOI: 10.1109/IRMMW-THz50926.2021.956.

[e] **D. Jayasankar**, V. Drakinskiy, P. Sobis, and J. Stake, "Design and development of 3.5 THz Schottky-based fundamental mixer", in Proceedings of the *2020 50th European Microwave Conference (EuMC)*, Utrecht, Jan. 2021, pp. 595-598, DOI: 10.23919/EuMC48046.2021.9338204.

[f] F. Mubarak, G. Phung, U. Arz, I. Jeune, G. Ducournau, K. Haddadi, T. Flisgen, R. Doerner, D. Allal, **D. Jayasankar**, J. Stake, R. Schmidt, G. Fisher, N. Ridler, X. Shang, "Interlaboratory investigation of on-wafer S-parameter measurements from 110 GHz to 1.1 THz", European microwave conference (EuMc), Berlin, Germany, 2023, pp. 624-627, DOI: 10.23919/EuMC58039.2023.10290550.

[g] F. Mubarak, G. Phung, U. Arz, I. Jeune, G. Ducournau, K. Haddadi, T. Flisgen, R. Doerner, D. Allal, **D. Jayasankar**, J. Stake, R. Schmidt,

G. Fisher, N. Ridler, X. Shang, "An Interlaboratory Comparison of On-Wafer S-Parameter Measurements up to 1.1 THz", submitted to *IEEE Transactions on Terahertz Science and Technology*, 2024.

[h] **D. Jayasankar**, A. I. Hernandez-Serrano, R. A. Hand, J. Stake and E. MacPherson, "Investigation of Hydrogel Skin Phantoms Using Terahertz Time-domain Spectroscopy," in Proceedings of the *2022 52nd European Microwave Conference (EuMC)*, Milan, Italy, Sep. 2022, pp. 401-403, DOI: 10.23919/EuMC54642.2022.9924308.

[i] J. Skinner, M. J. Salter, N. M. Ridler, Y. Wang, M. Salek, J. Stake, **D. Jayasankar**, J. Hesler and S. Durant, "Interlaboratory comparison of S-parameter measurements in WM-380 waveguide at frequencies from 500 GHz to 750 GHz" *Tech. Report*, National Physical Laboratory (NPL), Aug. 2022. DOI: 10.47120/npl.tqe23.

[j] **D. Jayasankar**, "Design and Characterisation of Terahertz Schottky Diode Harmonic Mixers" *Licentiate thesis*, Department of Microtechnology and Nanoscience (MC2), Chalmers University of Technology, Dec. 2021. URL: https://research.chalmers.se/en/publication/527034

Acknowledgments

'If I have seen further, it is by standing on the shoulders of giants'
- Isaac Newton

First, I want to convey my heartfelt appreciation to Prof. Jan Stake for his mentorship and support throughout my master's and PhD studies. I enjoy all our discussions and brainstorming sessions. Thanks for encouraging me to apply for scholarships, supporting my research visits, pushing me beyond my comfort zone, and always being available for discussions. I wouldn't have made it this far without your guidance, for which I will forever be grateful. It's an honour and privilege to be part of your team.

I also want to thank Dr. Jeffrey Hesler, my co-supervisor, and Jody Hesler. Their support during my research visit to Virginia Diodes Inc. (VDI) in Charlottesville in 2023 was invaluable. I am grateful for all our discussions about THz mixers, especially while writing this thesis. I am grateful to Dr. Peter Sobis, Mr. Vladimir Drakinskiy, and Mr. Mats Myremark for their remarkable expertise. I also appreciate Dr. Per Olof Hedekvist from the Research Institutes of Sweden (RISE), Borås, for supporting me throughout my PhD and Warwick research visit. Thanks to my manager Dr. Karin Cedergren from RISE. I also appreciate Dr. Helena Rodilla for carefully reviewing my manuscripts and all the impromptu discussions about semiconductor physics. I am grateful to Prof. Tom Wenckebach for his compendium on 'Noise at THz frequencies'. The support from my colleagues Dr. Tomas Bryllert, Dr. Josip Vukusic, Andre Koj, Dr. Olivier Auriacombe, and Jonathan Westin has been invaluable. I would also like to thank my teachers from the Wireless, Photonics, and Space Engineering program, with a special mention to Prof. Thomas Rylander for the computational electromagnetics course and Prof. Christian Fager, my examiner, for your continued support.

Thanks to colleagues Dr. Nick Rothbart and Prof. Heinz-Wilhelm Hübers from the German Aerospace Center (DLR) for their support and encouragement during my research visit in 2021. I sincerely thank Prof. Holger T. Grahn and colleagues from the Paul-Drude Institute for Semiconductor Physics (PDI) for their insightful comments and suggestions. I enjoyed working with Prof. Emma Macpherson and her colleagues during my internship at the University of Warwick, Coventry, in 2022, who generously shared their expertise in THz time-domain spectroscopy. I'd also like to acknowledge Dr. Theodore Reck,

Mr. Steven Durant, and colleagues from VDI for their support and assistance during THz mixer measurements. Thanks to Dr. Elena Saenz, ESTEC, for fruitful discussions during ESA project meetings.

Special thanks to Sara Catteau for being the shoulder I always depend on. Thanks to our Bamse's Kompisklubben Nelson Rebelo, Malte Dornieden, and Patrik Blomberg for making this journey more fun and exciting. I will forever cherish our trip to Lund, cykla dressin, and fika sessions. Looking back on these past seven years in Sweden, Dr. Junjie Li, you've been my constant, and I hope we both will become experts in foraging kantareller. Thanks to all my friends and colleagues, Aditya Goturu, Francesco, Pengpeng, Roger, Yin, Yu Yan, Serguei, Nirmal, Rakhee and Debbie.

To my beloved Amma and Appa, Balasaraswathy, and Jayasankar, to whom I dedicate this thesis with all my heart. Your countless sacrifices and support have been the foundation of my journey. Amma, thank you for nurturing my interest in science from an early age. You both have always managed to calm my mind, especially during the challenging final months of this work. To my husband, Prabhu, your love and belief in me have been my anchor through difficult times. I am looking forward to more hiking and visiting K-Pg impact sites. Thanks to my in-laws and family in India for their support and encouragement.

In memory of the late Dr. Heiko Richter from DLR —a remarkable colleague, mentor, and friend. He taught me everything about THz spectroscopy and guided me through quasi-optical measurements. We shared an 'experiment wish list' we wanted to work on. I aspire to tick off experiments from that list in the future.

My PhD project is supported by the Swedish Foundation for Strategic Research (SSF) project number FID17-0040 and the Swedish Innovation Agency (Vinnova) project 2022-02967. This work was supported in part by the Swedish Research Council (Vetenskapsrådet) under grant 2020-06187 and the WiTECH centre in a project financed by VINNOVA, Chalmers University of Technology, Omnisys, LNF, RISE and VDI.

Divya Jayasankar
Göteborg, Nov. 2024

List of abbreviations

ALMA	Atacama Large Millimetre Array
AWS	Arctic Weather Satellite
CAD	Computer Aided Design
CW	Continuous Wave
DC	Direct Current
DLR	Deutsches zentrum für Luft- und Raumfahrt
DSB	Double Side-Band
DUT	Device Under Test
EM	Electromagnetic
ESA	European Space Agency
HB	Harmonic Balance
HBV	Heterostructure Barrier Varactor
HEB	Hot electron bolometer
HSO	Herschel Space Observatory
IF	Intermediate Frequency
JPL	Jet Propulsion Laboratory
JUICE	Jupiter Icy moon Explorer
LERMA	Laboratoire d'Etudes du Rayonnement et de la Matière en Astrophysique et Atmosphères
LNA	Low Noise Amplifier
LO	Local Oscillator
METOP-SG	Meteorological Operational Satellite - Second Generation
MIRO	Microwave Instrument for the Rosetta Orbiter
MMIC	Microwave Monolithic Integrated Circuit
MLT	Mesosphere Lower Thermosphere
NASA	National Aeronautics and Space Administration
PDI	Paul-Drude-Institut für Festkörperelektronik
PLL	Phase Locked Loop
QCL	Quantum-Cascade Laser
RF	Radio Frequency
S-parameter	Scattering parameter
SOFIA	Stratospheric Observatory for Far-Infrared Astronomy
SWI	Sub-millimetre-Wave Instrument
TPX	Polymethylpentene
VNA	Vector Network Analyser

List of notations

α	Attenuation constant
N_{buf}	Buffer layer doping concentration
Φ_B	Barrier height
ψ_{bi}	Built-in potential
Z_c	Characteristic impedance
γ	Complex propagation factor
E_c	Conduction band
L	Conversion loss
I_d	Diode current
η	Diode ideality factor
V_d	Diode voltage
w_d	Depletion width
Z_{IF}	Diode embedding impedance at IF
Z_{LO}	Diode embedding impedance at LO
Z_{RF}	Diode embedding impedance at RF
m_e^*	Effective electron mass
m_h^*	Effective hole mass
σ_{buf}	Electrical conductivity of buffer layer
σ_{epi}	Electrical conductivity of epi-layer
χ_s	Electron affinity
E_g	Energy bandgap
N_{epi}	Epi-layer doping concentration
V_F	Forward bias voltage
f	Frequency
λ_g	Guide wavelength
C_j	Junction capacitance
V_j	Junction voltage
μ_n	Low-field electron mobility
μ_p	Low-field hole mobility
μ_0	Magnetic permeability of free space
ϕ_m	Metal work function
L	Mixer conversion loss

β	Propagation phase constant
R_{anode}	Schottky anode radius
ϵ_r	Relative permittivity
V_R	Reverse bias voltage
S	Schottky contact area
Z_s	Series impedance
R_s	Series resistance
δ_s	Skin depth
t_{epi}	Thickness of epi-layer
E_v	Valence band
λ	Wavelength
C_{j0}	Zero-bias junction capacitance

Physical constants

c	$2.9979 \times 10^{8}\,\text{m/s}$
h	$6.6260 \times 10^{-34}\,\text{m}^2\,\text{kg/s}$
k_B	$1.3806 \times 10^{-23}\,\text{J/K}$
μ_0	$4\pi \times 10^{-7}\,\text{H m}^{-1}$
ϵ_0	$8.8541 \times 10^{-12}\,\text{F m}^{-1}$
q	$1.6021 \times 10^{-19}\,\text{Coulombs}$

Contents

Chapter 1

Introduction

Terahertz heterodyne spectroscopy is an invaluable tool for detecting and mapping the thermal emission and absorption of atomic and molecular gases [1]–[3]. By analysing these spectral signatures at THz frequencies, we can probe the origin and composition of the early universe and gain insights into dynamic processes within Earth's atmosphere [4]. For instance, detecting gas species such as atomic oxygen (OI) at 4.7 THz [5], [6] and hydroxyl radical (OH) at 3.5 THz in the mesosphere-lower thermosphere (MLT) region is crucial for enhancing climate and weather prediction models [7], [8]. Future scientific objectives and instrument requirements for Earth observation missions necessitate THz spectrometers with a high spectral resolution capable of operating at ambient temperature over long flight durations.

Schottky barrier diodes are the workhorse behind sub-millimetre wave heterodyne spectrometers both as mixers and multipliers in local oscillator (LO) chains of ground-based observatory, high-altitude balloons and space-borne missions such as ALMA [20], STO [21], MIRO [22], ODIN [23], HSO [24], METOP-SG [25], JUICE [15] and AWS. Compared to ultra-low noise THz detectors, such as hot electron bolometer (HEB) or superconductor-insulator-superconductor (SIS), Schottky barrier diodes operate at ambient temperature and have wide instantaneous bandwidth [26]. Hence, it is well-suited for long-duration missions and detecting wide spectral ranges simultaneously.

In 1996, Betz *et al.* demonstrated a 4.7-THz whisker-contact Schottky diode in a corner reflector mount with an epi-layer doping concentration of

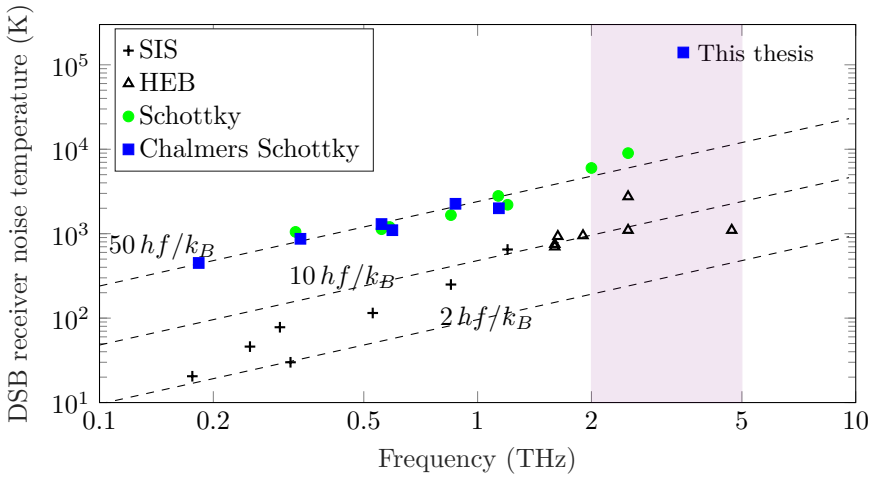

Figure 1.1: Sensitivity of THz mixers. Planar Schottky data is from [9]–[18], Paper [D] and the superconducting HEB and SIS mixers are from [19]. Note: hf/k_B is the quantum limit where h is Planck's constant, f frequency and k_B Boltzmann's constant.

10^{18} cm^{-3} with DSB noise temperature of 70,000 K [27], [28]. However, whisker-contacted diodes are sensitive to vibrations, making them unreliable for space missions [29]. The development of integrated and planar Schottky barrier diode technology during the 1990s by Bishop *et al.* from the University of Virginia (UVA) led to more reliable and advanced terahertz mixers and multipliers over the whisker-contacted devices [30]. In 1999, Siegel *et al.* from NASA-JPL demonstrated membrane-based technology that allows for low electrical parasitics and operation at terahertz frequencies [31]. Based on this monolithic membrane diode technology, the first planar 2.5-THz Schottky-based heterodyne receiver was built for NASA's Aura mission, which exhibited a 9000-K receiver noise temperature when pumped by far-infrared gas laser with high LO power of about 8 mW [32]. Recent advancements include the launch of the JUICE mission in April 2023, which is currently on its way to Jupiter. The sub-millimetre wave instrument aboard JUICE is equipped with two receiver channels, operating at 600 GHz and 1.2 THz, featuring GaAs Schottky detectors fabricated at Chalmers [10] and LERMA [15], respectively. In 2024, a 2-THz Schottky receiver front-end with a double side-band (DSB)

noise temperature of about 8000 K was demonstrated by NASA-JPL. Despite these advancements, the realisation of planar, integrated Schottky mixers operating in the 2-5 THz range remains a grand challenge, which this work aims to address, refer Fig. 1.1.

Thanks to the development of far-infrared quantum cascade lasers (QCLs), detectors beyond 3 THz are now feasible. QCLs, with a few mW of output power and continuous-wave operation, are ideal as LO sources for THz detectors [33], [34]. However, they are sensitive to cryocooler vibrations, temperature, and bias current variations, causing frequency drifts and instabilities. Stabilizing the QCL is essential for resolving fine details in gas emission spectra [35], underscoring the need for THz harmonic mixers at 3.5/4.7 THz.

The main focus of this dissertation is the development of planar Schottky-barrier diode receivers operating in the frequency range of 3-5 THz. A comprehensive large-signal analysis was conducted on harmonic mixers operating between 2-5 THz. The impact of idler terminations (Z- and Y-mixers) on harmonic mixer performance was presented in [**Paper A**]. Building this theoretical foundation, a 3.5-THz, $\times 6$ harmonic mixer was designed and fabricated. The resulting conversion loss at 3.5 THz under various pump and bias conditions aligned with simulation results as presented in [**Paper B**] and followed by successful phase-locking of 3.5/4.7-THz QCLs that was demonstrated in [36]. However, the lack of wideband and tunable sources presents a significant challenge for characterising mixers across a broad frequency range. An alternative measurement technique for wide-band characterisation of THz harmonic mixers was demonstrated from 2.2 THz to 3 THz in [**Paper C**].

A key aspect of this research is the design and characterisation of fundamental mixers [**Paper D**]. The preliminary DSB noise temperature measurements of the 3.5-THz fundamental mixers are about 140,000 K, and discrepancies were attributed to poor Gaussian beam coupling and high losses in the RF chain. Therefore, a scaled-down experiment was conducted to investigate the impact of E-plane misalignment on a diagonal horn antenna in the WM570 frequency band (330-500 GHz), as presented in [**Paper E**]. Based on the results, we optimised the 4.7-THz, $\times 8$-harmonic mixer with an integrated pyramidal horn, summarising the design in [**Paper F**].

The thesis starts with an overview of the critical components for building a THz Schottky-based heterodyne detector and provides a detailed summary of planar Schottky-barrier diode technology. Chapter 3 delves into the design

and modelling of THz harmonic and fundamental mixers and concludes with a discussion of the fabrication and assembly of integrated circuits in the mixer housing. Chapter 4 presents the DC/RF characterisation methods. Chapter 5 presents the RF characterisation results of harmonic and fundamental mixers, highlighting the promising potential and challenges in realising THz mixers. Finally, Chapter 6 summarises the critical findings of this work and provides a future outlook.

Chapter 2

Terahertz diode receivers

This chapter begins with an introduction to heterodyne receivers, followed by an overview of crucial front-end components such as feed horns and mixers. It includes a detailed discussion on the operation of diode mixers, various design topologies, including the single-ended mixer configuration used in this thesis, and an overview of harmonic balance simulation for analysing nonlinear circuits. The chapter then focuses on the metal-semiconductor interface, particularly the formation of Schottky-barrier diodes. It presents the series resistance and junction capacitance model for planar air-bridged Schottky diodes. Finally, it describes the material properties and frequency-dependent permittivity model of GaAs.

2.1 Heterodyne receivers

Heterodyne detectors operate by down-converting both the phase and amplitude of the incoming THz signal to a much lower intermediate frequency (IF) signal, typically in the GHz range. This is in contrast to the direct detectors, which only measure amplitude information [37]. Heterodyne receivers utilise two signals: an RF signal that carries the information and a LO pump signal to generate the IF signal, $f_{IF} = |f_{RF} - f_{LO}|$ as illustrated in Fig. 2.1.

Heterodyne receivers are ideal for spectroscopic applications, as they maintain spectral information and allow for a high resolution of about $\Delta f/f \geq 10^6$, which corresponds to a velocity resolution of $v = 0.03$ km s^{-1}. This is cru-

cial for resolving the fine spectral features and Doppler shifts of atomic and molecular transitions. The down-converted IF signal is amplified using a low-noise amplifier (LNA) and later analysed in the receiver back-end spectrometer as depicted in Fig. 2.1. Due to atmospheric attenuation, primarily from different scattering mechanisms and water vapour absorption, ground-based observations at frequencies above 2 THz are impractical. Hence, we require high-altitude balloons [6] or space-based missions to detect THz signals [26].

Receiver noise temperature, sensitivity, and stability are crucial parameters for evaluating the performance of a receiver. Superconducting detectors, such as Superconductor-Insulator-Superconductor (SIS) or Hot Electron Bolometer (HEB) devices, achieve receiver noise temperatures closer to the quantum limit, (hf/k_B), where h is the Planck's constant, f is the frequency, and k_B is the Boltzmann's constant. [19]. Nevertheless, Schottky-based receivers are attractive for long-duration flight missions as they provide wide instantaneous bandwidth, fast response time, and operate without cryogenic cooling [26].

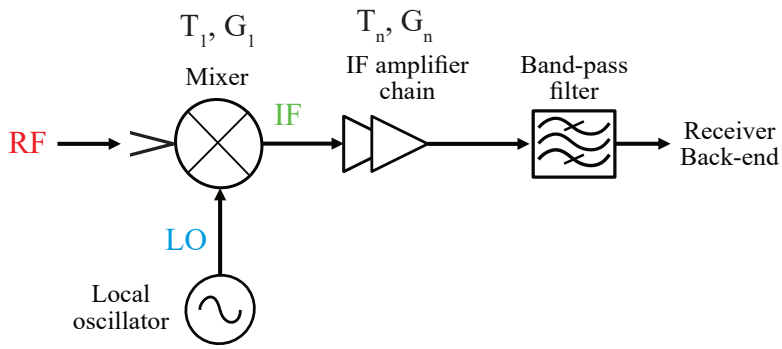

Figure 2.1: Simplified schematic of a double sideband (DSB) heterodyne detection scheme. IF signal frequency is the difference between the RF and LO signals.

The overall equivalent receiver noise temperature of a multi-stage, cascaded system can be evaluated using Friis' formula [38], which is given by:

$$T_{rec} = T_1 + \frac{T_2}{G_1} + \frac{T_3}{G_1 G_2} + .. + \frac{T_n}{G_1 ... G_{n-1}} \tag{2.1}$$

where, T_{rec} is the receiver noise temperature, T_1,.., T_n represent the noise

temperature, and G_1,.., G_n are the gain or loss of each stage. Improving the first stage's noise performance will significantly impact T_{rec}. Therefore, it is crucial to have sensitive mixers and low-noise amplifiers in the first few stages.

For an ideal radiometer system, assuming no instabilities in the receiver noise temperature and system gain, sensitivity is given by [39],

$$\Delta T = \frac{T_A + T_{rec}}{\sqrt{\tau B}} \tag{2.2}$$

where, ΔT is the sensitivity, T_A and T_{rec} are antenna and receiver temperature, respectively. The system noise temperature is given by, $T_{sys} = T_A + T_{rec}$, τ is the integration time, and B is the bandwidth [39]. For a fixed bandwidth, better sensitivity can be achieved by decreasing the receiver noise temperature or increasing the measurement integration time. However, any instabilities in the receiver chain (for example, gain fluctuations) will set an upper limit on the integration time, thereby affecting the instrument's resolution. System stability is measured via the Allan variance plot initially developed to study the noise and stability of atomic clocks by D. Allan [40]. A detailed note on stability experiments can be found here [41].

2.1.1 Local oscillator

The need for high LO power to drive the mixers is one limiting factor in realising THz Schottky diode receivers. Fig. 2.2 shows the available signal power from solid-state terahertz sources. Trendlines are indicated with a $1/f^2$ and a $1/\lambda^2$ dependence, respectively. The highest output power from electronic sources is achieved by combining several diode circuits. The heterostructure barrier varactor (HBV) [42] data are taken from [43]–[47]; the Schottky varactors are from [18], [48], [49]; the resonant-tunnelling diodes (RTD) are from [50]–[52]; and the quantum-cascade lasers (QCLs) are from [53]–[55]. Superconducting detectors such as HEB typically require LO power in the μW - nW [56]. However, Schottky-barrier diode-based mixers require much higher LO power in the milli-watts (mW) range.

QCLs are an ideal LO source, delivering a few mW output power and supporting continuous-wave (CW) operation. However, QCLs are prone to frequency instabilities caused by cryocooler vibrations, fluctuations in bias current, and temperature variations [57]. Therefore, frequency stabilisation is crucial for achieving high-spectral resolution [Paper B] and [36]. A compre-

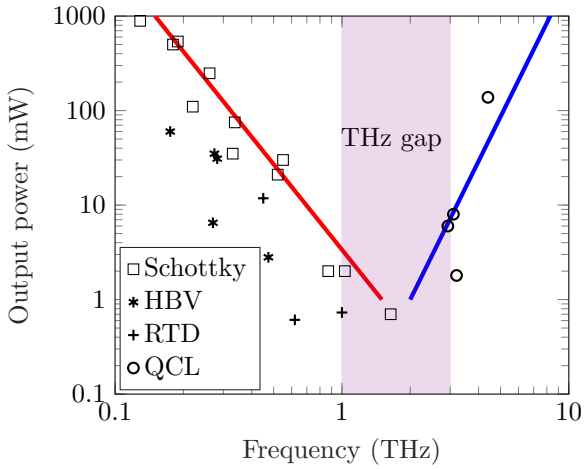

Figure 2.2: Available signal power from solid-state terahertz and optical sources.

hensive discussion on output power and frequency characterisation, including a current-temperature map of the QCLs that illustrates mode jumps, can be found in [36].

2.2 Feed horns

Feed horns are an integral part of a receiver that couples the incoming signal to the non-linear detector elements like diodes. Various THz quasi-optical applications such as astronomy [58], imaging, and spectroscopy [11] utilise detectors with integrated horns to couple the incoming signal to the diode [59] or allow signal sources to radiate into free space [60]. Some critical performance metrics of horn antennas are return loss, bandwidth, directivity, radiation pattern, and polarisation [61].

In addition, the optical coupling to a Gaussian beam (Gaussicity) is an essential parameter for quasi-optical system design [62]. Gaussicity is defined as the maximum power coupling of the beam produced by the horn to a linearly polarised Gaussian beam, and it can be calculated from aperture E-fields as shown in Eq. 2.3 [63], [64].

$$\eta_{gauss} = \frac{\left|\left\langle \hat{E}_{ap} \mid \hat{g} \right\rangle\right|^2}{\left\langle \hat{E}_{ap} \mid \hat{E}_{ap} \right\rangle \left\langle \hat{g} \mid \hat{g} \right\rangle} \tag{2.3}$$

where, E_{ap} is the E-field distribution at the aperture and g is the Gaussian function. Gaussicity of various commonly used horns are: diagonal - 84%, pyramidal - 85% and corrugated antennas - 98% [63].

Corrugated feed horns are an ideal candidate for astronomical applications due to low cross-polarisation and high Gaussicity of about 98% [65], [66]. Corrugated horns are realised using electroforming, which involves machining single-use mandrels later coated with copper through electrodeposition. However, achieving uniform $\lambda/4$ corrugations and coating becomes difficult and expensive at sub-millimetre wavelengths. Other horn profiles offer easier fabrication compared to electroforming, such as Pickett-Potter horns [67], [68] and conical horns [69].

However, a key challenge in realising components above 2 THz is their sensitivity to machining tolerances, even in the order of a few microns. Hence, this thesis uses more straightforward profiles, such as diagonal and pyramidal horns, due to their simplified manufacturing processes and seamless integration with rectangular waveguides.

2.2.1 Diagonal horn

The 'square-aperture' horn first introduced by Li in 1952, consists of a rectangular to circular waveguide transition that converts the dominant transverse electric mode TE_{10} to TE_{11} and a second transition that converts TE_{11} to

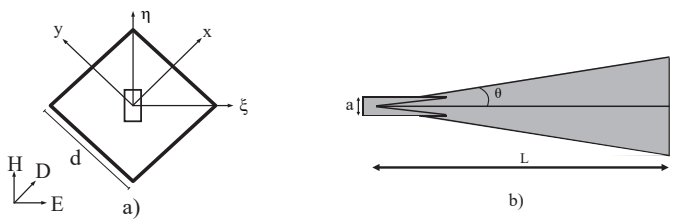

Figure 2.3: Schematic of a diagonal horn antenna.

a diagonally polarised wave in the square waveguide - a superposition of two TE_{10} and TE_{01} waveguide modes. Later, A.W. Love experimentally verified its radiation pattern and coined the term 'Diagonal horn' [70]. Later, in 1992, Johansson and Whyborn omitted the intermediate circular waveguide transition and demonstrated an integrated diagonal horn with rectangular waveguide feed in an E-plane split block at sub-millimetre wave frequencies, see Fig. 2.3. The aperture E-field distribution is given as,

$$E_{ap} = \left[E_{01}\cos\left(\frac{\pi y}{d}\right)\hat{x} + E_{10}\cos\left(\frac{\pi x}{d}\right)\hat{y} \right] \cdot e^{jk\rho} \tag{2.4a}$$

$$k\rho = \frac{2\pi}{\lambda_o}\left[\frac{d^2 - 2x^2 - 2y^2}{4L}\right] \tag{2.4b}$$

where λ_o is the free space wavelength and k_ρ is the spherical phase front [71]. The corresponding co- and cross-polarisation components are given as,

$$E_\eta = \hat{\eta} \cdot E_{ap} = \frac{1}{\sqrt{2}}\left[E_{01}\cos\left(\frac{\pi y}{d}\right) + E_{10}\cos\left(\frac{\pi x}{d}\right) \right] \cdot e^{jk\rho} \tag{2.5a}$$

$$E_\xi = \hat{\xi} \cdot E_{ap} = \frac{1}{\sqrt{2}}\left[E_{01}\cos\left(\frac{\pi y}{d}\right) - E_{10}\cos\left(\frac{\pi x}{d}\right) \right] \cdot e^{jk\rho} \tag{2.5b}$$

The far-field radiation pattern is computed using a 3D-EM model in the finite-element method (FEM) solver, refer to Fig. 2.4. The diagonal horns have high side-lobe levels in the D-plane ($\approx$ 15 dB). By integrating the power in the aperture E-field in Eq. 2.5, the power radiated to the cross-polar component can be computed, and it is relatively high $\approx$ 10% [72].

The performance of diagonal horns depends on the phase and amplitude balance between the TE_{10} and TE_{01} modes. Any asymmetry, such as E-plane misalignment, can lead to mode imbalance, increasing cross-polarisation levels, and result in an elliptically polarised beam. Fabricating these components at high frequencies (>2 THz) with micron-level precision presents significant challenges. A detailed discussion of the problem, as mentioned above, and experimental verification is presented in Chapter 4.

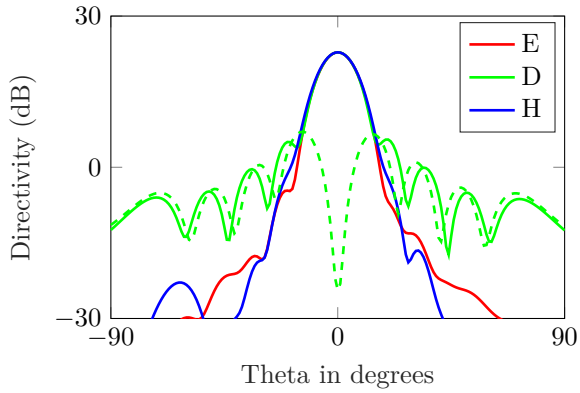

Figure 2.4: Simulated far-field radiation pattern of a diagonal horn. Solid lines represent the copolar directivity in the following ϕ cuts: E ($\phi = 0°$), D ($\phi = 45°$) and H ($\phi = 90°$) planes. The dashed line represents cross-polar directivity in the D-plane.

2.2.2 Pyramidal horn

Pyramidal horns are widely used in many applications, including communication systems and as a standard-gain antenna for calibration [61]. It is easier to construct and can be fed with a rectangular waveguide, as shown in Fig. 2.5. The E- and H- fields over the horn's aperture are approximated in Eq. 2.6. Due to the 'single-mode' operation, they are less susceptible to

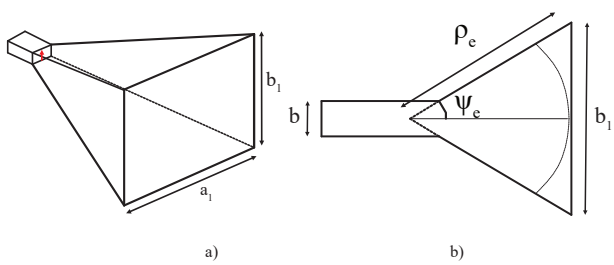

Figure 2.5: Schematic of a pyramidal horn antenna.

geometrical asymmetries. Section 5 presents simulations comparing aligned and misaligned pyramidal horns. Pyramidal horns exhibit Gaussicity of about 85%, and co- and cross-polar directivity in E-, D- and H-planes obtained from 3D-EM simulation is presented in Fig. 2.6.

$$E_y = E_{10}\cos\left(\frac{\pi}{a_1}x\right)e^{-j[k(x^2/\rho_2+y^2/\rho_1)]} \tag{2.6}$$

$$H_x = -\frac{E_{10}}{\eta}\cos\left(\frac{\pi}{a_1}x\right)e^{-j[k(x^2/\rho_2+y^2/\rho_1)]} \tag{2.7}$$

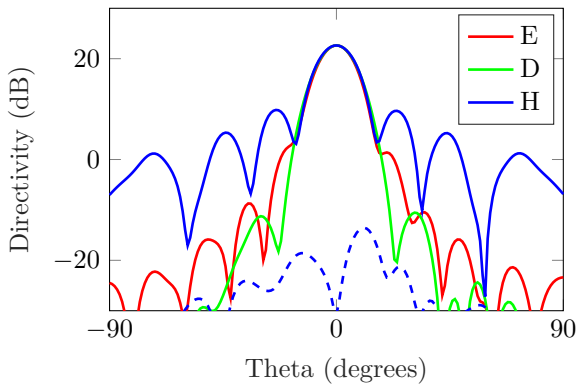

Figure 2.6: Simulated far-field radiation pattern of a Pyramidal horn. Solid lines represent the copolar directivity in the following ϕ cuts: E ($\phi = 0°$), D ($\phi = 45°$) and H ($\phi = 90°$) planes. The dashed line represents cross-polar directivity in the H-plane.

2.3 Diode mixers

Mixers, also called frequency converters, are used to convert high-frequency signals to low-frequency signals (down-conversion) using a LO signal which is commonly used in receivers $f_{IF} = |f_{RF} - f_{LO}|$. In contrast to an up-converting mixer, which generates an RF signal from a low-frequency signal ($f_{RF} = f_{LO} \pm f_{IF}$). The frequency conversion occurs due to the diode's non-linear I-V characteristic. When the frequency conversion or mixing process is achieved using non-linear resistance, the device is referred to as a resistive

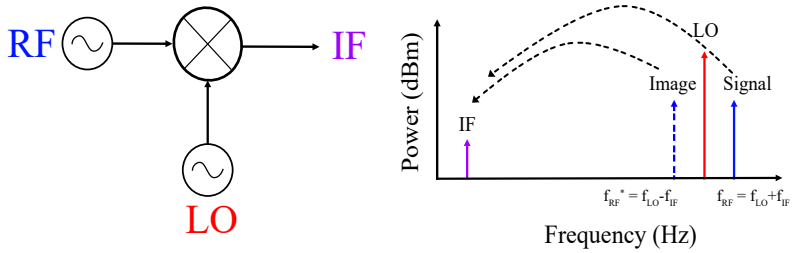

Figure 2.7: Frequency down-conversion process in a DSB mixer.

mixer [73].

In double-sideband (DSB) mixers, both the upper and lower sidebands are down-converted to the same IF as shown in Fig. 2.7. Conversely, if one of the sidebands is filtered out, leaving the IF with only one sideband, the mixer is referred to as a single sideband (SSB) mixer. Some common topologies used for designing THz mixers are discussed, and the pros/cons of each topology are discussed in detail in this section.

Single-ended fundamental mixer

A single-ended mixer topology consists of a non-linear mixing element (diode) and filters for transmission and suppression of the signals, as shown in Fig. 2.8.

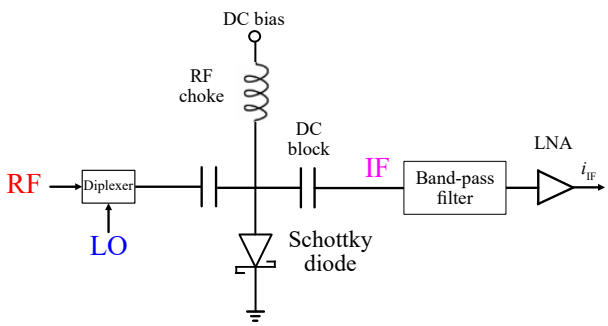

Figure 2.8: Schematic of a single-ended diode mixer.

The input RF and LO signals are expressed as,

$$V_{\mathrm{RF}}(t) = V_{\mathrm{RF}}\cos(\omega_{\mathrm{RF}}t) \tag{2.8}$$

$$V_{\mathrm{LO}}(t) = V_{\mathrm{LO}}\cos(\omega_{\mathrm{LO}}t) \tag{2.9}$$

where, $\omega_{\mathrm{RF}} = 2\pi f_{\mathrm{RF}}$ and $\omega_{\mathrm{LO}} = 2\pi f_{\mathrm{LO}}$. Using Taylor series expansion, the diode current can be expressed as,

$$i(t) = a_0 + a_1 v(t) + a_2 v^2(t) + a_3 v^3(t) + ... \tag{2.10}$$

and $v(t)$ is given by,

$$v(t) = V_{\mathrm{RF}}(t) + V_{\mathrm{LO}}(t) \tag{2.11}$$

and Eq. 2.10 is expanded as,

$$\begin{aligned} i(t) = a_1 &+ a_2[V_{\mathrm{RF}}(t) + V_{\mathrm{LO}}(t)] \\ &+ a_3[V_{\mathrm{RF}}(t) + V_{\mathrm{LO}}(t)]^2 \\ &+ a_4[V_{\mathrm{RF}}(t) + V_{\mathrm{LO}}(t)]^3 \end{aligned} \tag{2.12}$$

The third term is rewritten using trigonometric identities as follows:

$$i(t) = a_3[V_{\mathrm{RF}}(t)^2 + V_{\mathrm{LO}}(t)^2 + 2V_{\mathrm{LO}}(t)V_{\mathrm{RF}}(t)] \tag{2.13}$$

$$\begin{aligned} i(t) = a_3[&V_{\mathrm{RF}}^2(1 + \cos(2\omega_{\mathrm{RF}}t)) \\ &+ V_{\mathrm{LO}}^2(1 + \cos(2\omega_{\mathrm{LO}}t)) \\ &+ 2V_{\mathrm{LO}}V_{\mathrm{RF}}(\cos\omega_{\mathrm{RF}}t\ \cos\omega_{\mathrm{LO}}t)] \end{aligned} \tag{2.14}$$

The capacitor will block the two DC terms, and the other mixing products $2\omega_{RF}$, $2\omega_{LO}$ and $\omega_{RF} + \omega_{LO}$ will be filtered by the IF filter. The desired IF output is,

$$i_{IF}(t) = a_3 V_{\mathrm{RF}} V_{\mathrm{LO}}[\cos(\omega_{RF} - \omega_{LO})t] \tag{2.15}$$

Balanced fundamental mixer

A balanced mixer consists of two or more single-ended diodes that are excited differentially, as shown in Fig. 2.9.

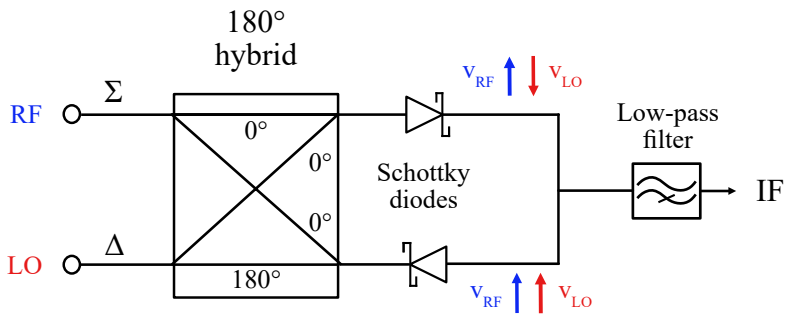

Figure 2.9: Schematic of a balanced diode mixer.

The RF signal is applied to the sigma port (Σ) and is in phase at the two diodes, which are indicated by arrows in blue, whereas the LO signal is applied at the delta port (Δ), and there is a 180° phase difference and indicated by arrows in red. Since the applied RF voltage is at phase, the IF currents combine at the node joining the diodes in phase [74]. However, the amplitude modulated (AM) noise and spurious signals are 180° out-of-phase and cancel at the IF output [75].

Sub-harmonic mixer

The sub-harmonic pumped mixers are realised using anti-parallel diode topology as shown in Fig. 2.10. It was first proposed by Cohn *et. al* in 1975 [76]. It utilises the second-harmonic of the LO signal ($f_{LO} = f_{RF}/2$), which is useful at THz frequencies where available LO power is scarce, as shown in Fig. 2.2. The desired IF is generated by mixing the RF signal with the second harmonic of the LO signal [18].

$$f_{\mathrm{IF}} = |f_{\mathrm{RF}} - 2\ f_{\mathrm{LO}}| \tag{2.16}$$

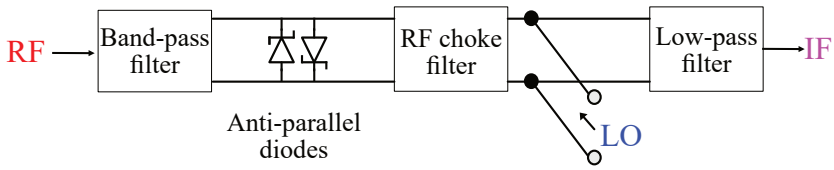

Figure 2.10: Schematic of the sub-harmonic mixer

The external current is $I = I_1 + I_2$ and $I = 2aV + 2cV^3 + ...$ and the loop current is given by $I_{loop} = I_1 = -I_2 = bV^2 + dV^4 + ...$ The odd-order current components are in the external circuit, and the even-order components circulate within the loop [74]. The fundamental mixing product is suppressed; therefore, the anti-parallel diode mixers have low conversion loss and improved noise performance as the LO noise sidebands are suppressed. Since the DC term is also part of the diode loop current, direct video detection cannot be made with the anti-parallel diode mixers [76].

Single-ended harmonic mixers

The harmonic mixer utilises the n^{th} harmonic of the LO signal to generate the IF signal [77]. One challenge with the high harmonic mixer is that the un-

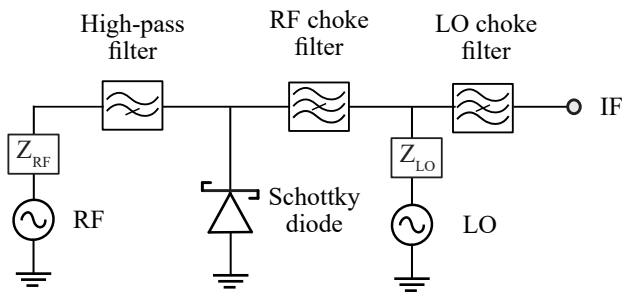

Figure 2.11: Schematic of the single-ended diode harmonic mixer topology implemented in [Paper B and F]. Z_{RF} and Z_{LO} are the optimum embedding impedance at the RF and LO frequencies, respectively.

wanted mixing harmonics (idlers) reduce the mixer sensitivity [78]. Unlike the anti-parallel/balanced diode topology discussed in the previous section. 2.3, they do not offer inherent cancellation of mixing products. It is possible to terminate the idlers reactively, but this is at the cost of increased design complexity [79]. The influence of different idler terminations on mixer conversion loss is discussed later in section 2.3.2.

$$f_{\mathrm{IF}} = |f_{\mathrm{RF}} - n f_{\mathrm{LO}}|, \tag{2.17}$$

where n is the harmonic index.

2.3.1 Non-linear circuit analysis

Harmonic balance is a commonly used technique to evaluate the mixer's performance [80]. It partitions a circuit of linear and non-linear elements into subcircuits, as shown in Fig. 2.12. The linear circuits are analysed using a multi-port network representation in the frequency domain, and the non-linear circuits are modelled using their I-V and Q-V characteristics are analysed in the time domain. A harmonic balance simulation aims to find a set of voltage

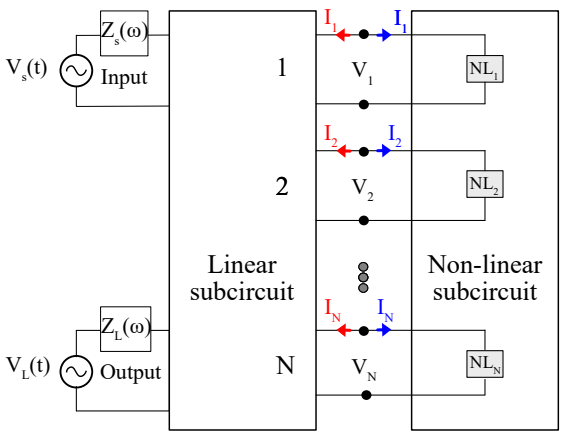

Figure 2.12: Harmonic balance. A non-linear circuit is divided into linear (frequency domain) and non-linear subcircuits (time domain).

waveforms that give the same current in the linear and non-linear subcircuits and satisfies Kirchhoff's current law at all harmonics [74], ω_p is the excitation frequency, and K is the harmonic number.

$$I_L(k\omega_p) + I_{NL}(k\omega_p) = 0 \tag{2.18}$$

2.3.2 Idler terminations

Saleh [73] has proposed different schemes and mixer topologies based on reactive idler terminations. Out-of-band frequencies that considerably influence the mixers' performance are called idlers. Based on the type of terminations that are presented to the idlers, mixers' performance can be improved.

Table 2.1: Mixer classification system based on out-of-band frequency terminations

Idlers ω_{2n}	Idlers ω_{2n+1}	Assigned name
Short	Short	Y-mixer
Open	Open	Z-mixer
Open	Short	G-mixer
Short	Open	H-mixer

Suppose the idlers are grouped into one and terminated by an open or short circuit in the unitary division scheme. These mixers are called Z- and Y-mixers, respectively. The binary division scheme divides the idler frequencies into odd and even frequencies. Grouping even and odd idler frequencies and terminating them with a short and open circuit are called an H-mixer; vice-versa is a G-mixer Table. 2.1. However, the Z- and Y-mixers represent best and worst-case scenarios. Hence, it is studied in detail in [Paper A], which discusses the effect of idlers (unitary division scheme) on harmonic mixer conversion loss and presents the embedding impedances at RF and LO frequencies for open and short circuit idler terminations.

2.4 Schottky-barrier diodes

Schottky diode is a two-terminal device with a metal-semiconductor (M-S) junction. Fig. 2.13a shows the schematic of the diode. The first work on metal-semiconductor diodes was reported in 1874 by Ferdinand Braun, who

observed the current rectification effect while probing a galena crystal (lead sulphide) with a metal wire [81]. Crystal detectors played an essential role in developing wireless telegraphy, for which he was awarded the Nobel prize in 1909 together with Marconi [82]. Around the same time, crystal detectors operating up to 60 GHz were developed by J. C. Bose [83].

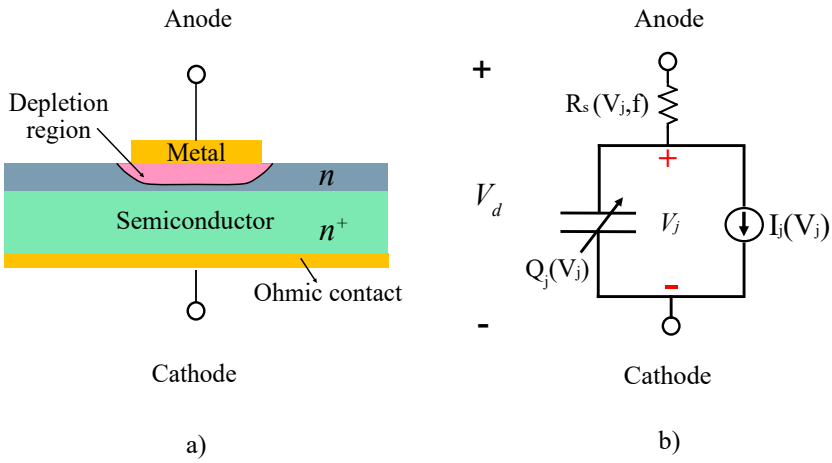

Figure 2.13: Schottky barrier diode a) Cross section of the metal-semiconductor junction b) Diode equivalent circuit.

Walter H. Schottky [84] postulated the concept of depletion layer; majority charge carrier conduction over the barrier; the relation between the barrier height and work function of metal and semiconductor; image-force lowering effect [85]. A metal-semiconductor junction can act as a Schottky barrier depending upon the metal work function ϕ_m and electron affinity χ_s in the semiconductor [86]-[87].

$$\Phi_b = \phi_m - \chi_s \tag{2.19}$$

Schottky-barrier diodes are uni-polar devices. For high-frequency applications, n-doped semiconductors are preferred due to electrons' high mobility and velocity [88]. Typical metals used as an anode contact are titanium (Ti), platinum (Pt), and gold (Au). For n-type semiconductors, the most commonly

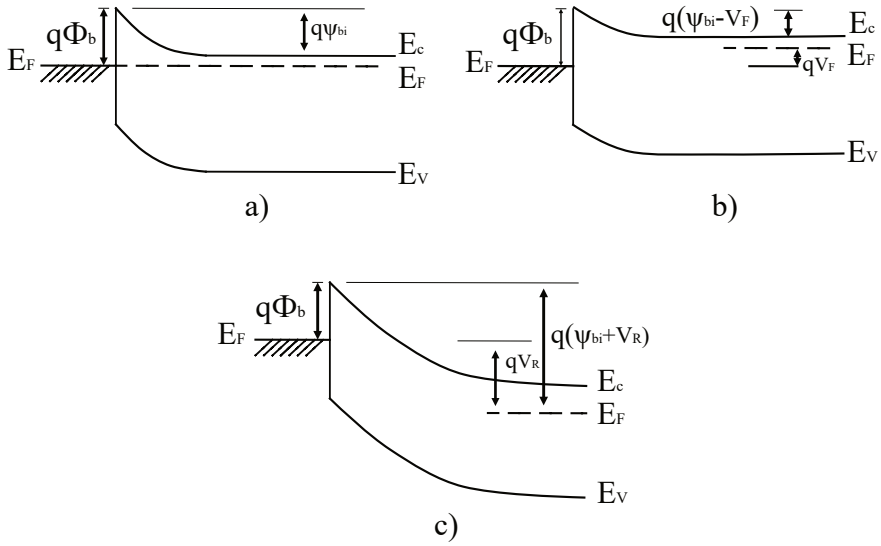

Figure 2.14: Energy band diagram of a metal and n-type semiconductor junction. (a) Zero bias, (b) Forward bias V_F, and (c) Reverse bias V_R.

used ohmic metal is gold-germanium (Au-Ge) [89]. A quasi-static equivalent circuit model for a Schottky diode is shown in Fig. 2.13b. It consists of three elements: a series resistance (R_s), a non-linear junction capacitance (C_j), and a current source. With quasi-static assumption, all non-linear elements are assumed to change instantaneously when their control voltage varies. It allows the representation of the equivalent circuit of a solid-state device by lumped linear and non-linear elements. For insights on advanced simulations that consider the microscopic origin of transport mechanisms (e.g.) Monte-Carlo (MC) based simulations for diode modelling, refer to [90].

Under thermal equilibrium conditions, a depletion region of width W_d is created due to the flow of electrons from the n-type semiconductor to the metal. Further transport of electrons is prevented due to the built-in potential (ψ_{bi}) created between the metal and semiconductor junction as shown in Fig. 2.14a. Under forward bias conditions see Fig. 2.14b, the diode operates in a voltage-controlled resistor mode, also known as a varistor. Under reverse

bias conditions, as shown in Fig. 2.14c, it acts as a voltage-controlled capacitor, or varactor [91]. Schottky-barrier diodes are operated in varactor mode for highly efficient frequency multiplication applications [92].

2.4.1 Planar Schottky barrier diodes

The traditional 'vertical' whisker contact Schottky diodes offer low parasitic capacitance but are mechanically sensitive and unreliable as the Schottky contact diameter decreases [93].

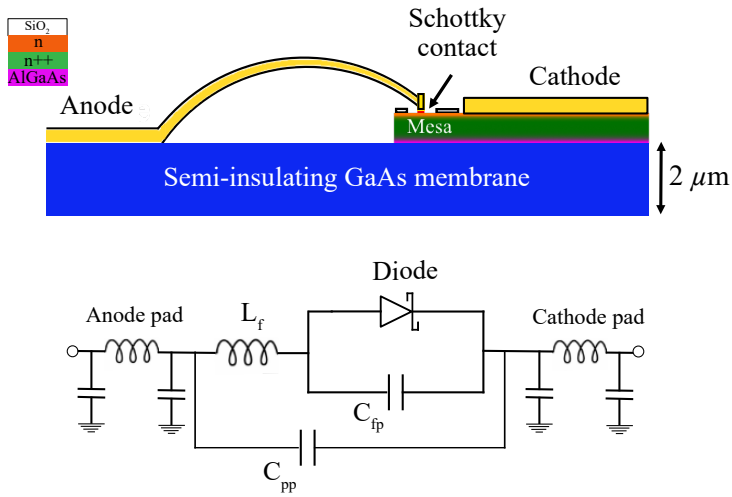

Figure 2.15: Planar air-bridged Schottky-barrier diode. a) Illustration of a planar diode realised on a 2-μm-thin semi-insulating GaAs membrane (Drawing not to scale). b) Planar lumped equivalent circuit model.

In 1987, Bishop *et al.* from the University of Virginia proposed a 'planar' surface channel etched Schottky diode technology, paving the way for the development of robust, reliable, and mechanically stable Schottky-barrier diodes [94]. For up to 300 GHz, discrete GaAs Schottky diodes were mounted by flip-chip technology on a low-loss quartz substrate ($\epsilon_r = 4.2$) [9], [95]. However, above 300 GHz, it is advantageous to build the integrated mixer circuitry on the same substrate, which allows for a high level of integration and improved design of coupling probes and filters. Since then, considerable research has

focused on improving Schottky diode performance by accurately modelling parasitic effects and reducing substrate loss, which led to the planar monolithic membrane diode (MOMED) process [31]. This technique is widely used in constructing mixers and multipliers above 1 THz [Paper B and D].

In this thesis, the integrated mixer circuitry was realised on a 2-μm-thin GaAs membrane [31], [96] as shown in Fig. 2.15. The parasitic elements of anode and cathode pad, finger inductance (L_f) and finger-to-pad capacitance (C_{fp}), are part of the embedding circuit, and the pad-to-pad capacitance is negligible, thanks to the ultra-thin GaAs membrane. The Schottky contact area of about 0.1 μm^2 and the epi-layer stack shown in Fig. 2.16 were used to realise the harmonic and fundamental mixers.

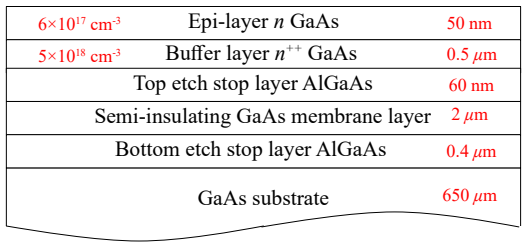

Figure 2.16: Epitaxial material layer stack of a typical THz Schottky diode mixer

2.4.2 Current-voltage characteristic

The current flow in a Schottky-barrier diode is governed by the following carrier transport mechanisms: thermionic emission, tunnelling, and drift-diffusion. For n-type semiconductors, current due to the minority charge carriers can be neglected. For GaAs Schottky-barrier diodes with a high carrier mobility, the majority of carrier transport is dominated by thermionic emission. Richardson was the first to explain the process of thermionic emission in vacuum tubes [97]. Later, Bethe proposed that it is also applicable to Schottky-barrier diodes [98]. The ideal current-voltage (I-V) characteristic of a diode is,

$$I_j(V_j) = I_s \left[\exp\left(\frac{qV_j}{\eta k_B T} \right) - 1 \right] \tag{2.20}$$

where I_s is the reverse saturation current, V_j is the junction voltage and η is the ideality factor. For an ideal diode with conduction dominated by thermionic emission, the ideality factor η equals 1. However, a high epi-layer doping concentration can narrow the depletion width.

$$W_d = \sqrt{\frac{2\epsilon_s \psi_{bi}}{qN_{\text{epi}}}} \tag{2.21}$$

Thereby causing the electrons to tunnel through the barrier, which degrades the ideality factor [85]. When the diode is highly forward-biased ($V_j \geq 3kT/q$), the diode current expression is simplified to,

$$I_j(V_j) = I_s \exp\left(\frac{qV_j}{\eta k_B T}\right) \tag{2.22}$$

where, $V_j = V_d - I_d R_s$. The small-signal conductance (g_j) is found by taking the partial derivative of the *I-V*,

$$r_j = \frac{1}{g_j} = \left(\frac{\partial I_j}{\partial V_j}\right)^{-1} = \frac{\eta kT}{qI_j} \tag{2.23}$$

2.4.3 Junction capacitance

The diode capacitance-voltage (C-V) relation is derived using Poisson's equation, which gives the voltage-dependent junction charge (Q_j) and capacitance (C_j) as

$$Q_j = SqN_{\text{epi}}W_d = S\sqrt{2q\epsilon_s N_{\text{epi}}(\psi_{bi} - V_j)} \tag{2.24}$$

$S = \pi R_{anode}^2$ is the Schottky contact area and V_j is the junction voltage

$$C_j \equiv \frac{dQ_j(V_j)}{dV_j} = \frac{\epsilon_s}{W_d} = S\sqrt{\frac{q\epsilon_s N_{\text{epi}}}{2(\psi_{bi} - V_j)}} \tag{2.25}$$

When the voltage applied across the diode is varied, the depletion width W_d will also vary as a function of the junction voltage. The zero-bias junction capacitance is then given by,

$$C_{j0} = S\sqrt{\frac{q\epsilon_s N_{\text{epi}}}{2\psi_{bi}}} \tag{2.26}$$

The potential of the epi-layer is curved near the periphery of the anode, as shown in Fig. 2.13. This lateral extension of the depletion region starts to play a role in Schottky contact with the sub-micron anode area; hence, it is important to include the first-order fringing effect [99],

$$C_j \simeq \frac{\epsilon_s S}{W_d(V_j)} + \frac{3\epsilon_s S}{D_{\text{anode}}} \tag{2.27}$$

$$C_j \simeq \frac{\epsilon_s S}{W_d}\left(1 + 1.5\left(\frac{W_d}{R_{\text{anode}}}\right)\right) \tag{2.28}$$

Where R_{anode} and D_{anode} are the radius and diameter of the Schottky contact, respectively. Detailed analysis of Schottky diodes' junction capacitance with realistic geometries implemented in a 2-D ensemble Monte Carlo simulator can be found in [100].

2.4.4 High-frequency series impedance

At high frequencies, carrier inertia results in degradation of conductivity and the frequency-dependent, complex AC conductivity is given by $\sigma_{\text{ac}} = \frac{\sigma_o}{1+j\omega\tau_{el}}$, where $\sigma_o = qN\mu$ is the DC conductivity and τ_{el} is the electron relaxation time [101]. In addition, due to skin-effect, the current is confined to the surface of the buffer layer, thus increasing the spreading resistance and becomes complex [102]. The overall series impedance is estimated by [103],

$$Z_s(V_j, f) \approx Z_{epi}(V_j, f) + Z_{spread}(f) + R_c \tag{2.29}$$

2.4.4.1 Epi-layer impedance

The undepleted epitaxial impedance can be approximated as

$$Z_{\text{epi}} = \frac{t_{\text{epi}} - W_d}{S\ \sigma_{\text{ac}}} \tag{2.30}$$

where t_{epi} is the total thickness of the epi-layer. Due to the voltage dependence of W_d, Z_{epi} also varies with voltage. At zero bias, $W_d = t_{\text{epi}}$, and there

is no impedance contribution from the epi-layer. Note: Varactor diodes used in frequency multipliers typically have low epi-layer doping concentration, and the conduction current in the undepleted epi-layer is limited by the velocity saturation current, resulting in a non-linear series impedance [104].

2.4.4.2 Buffer layer spreading impedance

Due to the high doping concentration and large ohmic contact, the current in the buffer layer spreads out. For a planar geometry, current flows laterally, see Fig. 2.17, and the calculation is geometry dependent.

Dickens presented the high-frequency bulk spreading resistance for a point contact diode, accounting for the skin effect [102]. Champlin later modified this expression to incorporate the carrier mass inertia effect and the displacement current term $j\omega\epsilon$ [101]. In a typical planar diode geometry, the ohmic contact partially surrounds the Schottky contact [103]. Consequently, the buffer spreading impedance is approximately double that of the whisker contact configuration, resulting in:

$$Z_{bulk} = 2\left(\frac{1}{4\sigma_o R_{anode}}\left[\frac{1}{1+j\left(\frac{\omega}{\omega_s}\right)}+j\left(\frac{\omega}{\omega_d}\right)\right]^{-1}\right) \tag{2.31}$$

$$Z_{skin} = 2\left(\frac{\ln(b/R_{anode})}{2\pi}\left(\frac{j\omega\mu_o}{\sigma_o}\right)^{1/2}\left[\frac{1}{1+j(\omega/\omega_s)}+j(\omega/\omega_d)\right]^{-1/2}\right) \tag{2.32}$$

Where b is the distance between the Schottky anode and ohmic contact, the total spreading impedance in the buffer layer is $Z_{spread} = Z_{bulk} + Z_{skin}$.

2.4.4.3 Ohmic contact resistance

The ohmic contact resistance can be calculated from the specific contact resistivity ρ_c and the effective ohmic contact area, S_{ohmic}.

$$R_c = \frac{\rho_c}{S^*_{ohmic}} \tag{2.33}$$

Murrman proposed the transmission line model of a planar contact in 1969 [105], which provides the transfer length that determines the effective ohmic contact area. The frequency dependence can be added, as shown by Bhau-

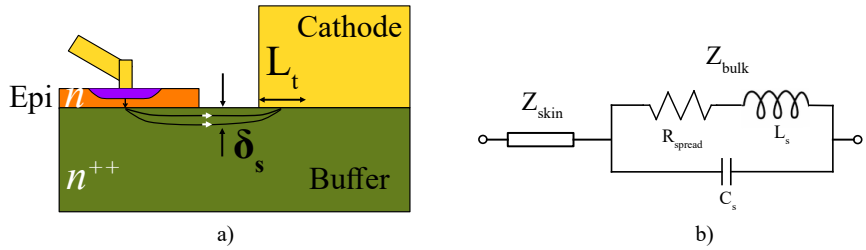

Figure 2.17: Spreading impedance in the buffer layer. a) Current flow in the highly conductive buffer layer is limited by the skin depth δ_s at high frequencies and transfer length L_t. b) Equivalent circuit of the buffer layer.

mik [103]. However, there is little experimental research to verify the high-frequency dependence. Therefore, this work uses the DC contact resistance, which is determined experimentally using transfer length test structures.

2.4.4.4 Plasma frequency

The parallel resonance caused by the charge carrier inertia (inductive) and dielectric relaxation (capacitive) corresponds to the classical plasma frequency and is given by [101],

N_d (cm^{-3})	$\frac{\omega_s}{2\pi}$ (THz)	$\frac{\omega_d}{2\pi}$ (THz)	$\frac{\omega_p}{2\pi}$ (THz)
$3\,\mathrm{x}10^{17}$	1.2	23.8	5.5
$4\,\mathrm{x}10^{17}$	1.3	29.8	6.3
$5\,\mathrm{x}10^{17}$	1.4	35.6	7.0
$6\,\mathrm{x}10^{17}$	1.5	40.9	7.7

Table 2.2: Scattering, dielectric relaxation frequency, and plasma frequency for different doping concentration

$$w_p = 2\pi f_p = \sqrt{\omega_s \omega_d} \tag{2.34}$$

where $f_s = \omega_s/2\pi$ and $f_d = \omega_d/2\pi$ are the scattering and dielectric relaxation frequency, respectively, and is given by $\omega_d = \sigma_o/\epsilon_s$ and $\omega_s = 1/\tau_{el} = q/m^*\mu_n$. Table. 2.2 summarises the scattering, dielectric relaxation and plasma fre-

quency for different doping concentrations. High epi-layer doping is preferred for high-frequency operation to avoid operating at the plasma resonance.

2.4.5 Noise

Noise is an essential figure of merit for mixers. The significant noise contributors in Schottky-barrier diodes are

- Thermal noise, also called Johnson or Nyquist noise, originates from the random motion of electric charge [106]-[107].
- Shot noise is due to the discrete nature and random variations of electrons generated due to current flow across the junction [108].

The shot noise current can be modelled as a current source parallel to I_j, and thermal noise associated with the series resistance of the diode can be modelled as a series voltage source [109] as shown in Fig. 2.18.

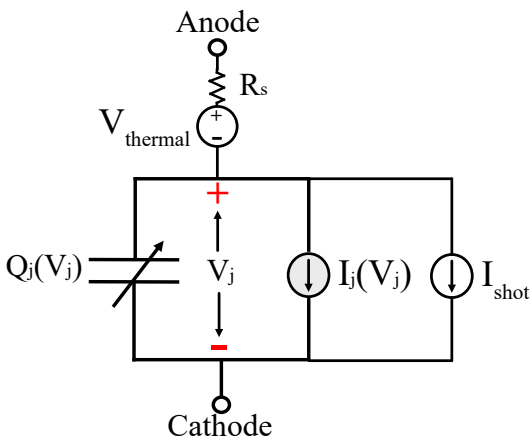

Figure 2.18: Equivalent circuit of noise sources in a Schottky diode

The mean-square shot-noise current in a forward-biased diode is,

$$\bar{I}^2_{\text{shot}} = 2qI_jB \tag{2.35}$$

Where I_j is the current in the resistive part of the junction. The mean square open-circuit noise voltage of a resistor is,

$$\bar{V}^2_{\text{thermal}} = 4k_BTBR \tag{2.36}$$

where B is the bandwidth in Hz, and R is the resistance.

2.5 Material properties

A summary of the critical material properties of GaAs at room temperature, the low-field electron mobility model, and the frequency-dependent permittivity model of GaAs are presented in this section.

Table 2.3: GaAs material properties at 300 K [110]–[112]

Symbol	Description	Value
E_g	Bandgap energy	1.42 eV
ϵ_s	Relative permittivity	12.9
m_e^*	Effective electron mass	$0.063{*}m_o$
μ_n	Phonon-limited electron mobility	8000 cm^2/V.s
v_{sat}	Saturation velocity	2.2×10^5 m/s

2.5.1 Low-field mobility model

With increasing doping concentration, scattering due to impurities increases, thereby reducing electron mobility. An empirical low-field mobility model that describes the influence of doping concentrations and ambient temperatures is given by [112],

$$\mu(N,T) = \mu_{min} + \frac{\mu_{max}(\frac{T_0}{T})^{\theta_1} - \mu_{min}}{1 + \left(\frac{N}{N_{ref}(\frac{T}{T_0})^{\theta_2}}\right)^{\lambda}} \tag{2.37}$$

Where $T_0 = 300\ K$ (room temperature), the fitting parameters are summarised in Table.2.4.

Table 2.4: Fitting parameters for low-field mobility model of GaAs and InGaAs [112]

Parameters	GaAs	$In_{0.53}Ga_{0.47}As$
μ_{min} (cm^2/V.s)	500	300
μ_{max} (cm^2/V.s)	9400	14000
N_{ref} (cm^{-3})	6×10^{16}	1.3×10^{17}
λ	0.394	0.48
θ_1	2.1	1.59
θ_2	3	3.68

A comparison of low-field electron mobility of GaAs and $In_{0.53}Ga_{0.47}As$ versus doping concentration using the empirical model by Sotoodeh [112] is presented in Fig. 2.19.

2.5.2 Dispersion model of GaAs

The dielectric function $\epsilon(\omega)$ of GaAs is modelled by the classical Lorentzian resonance function [111],

$$\epsilon(\omega) = \epsilon_\infty \left[1 + \frac{\omega_L^2 - \omega_T^2}{\omega_T^2 - \omega^2 + i\Gamma\omega}\right] \tag{2.38}$$

where, ω_L and ω_T are the longitudinal and optical phonon frequencies and

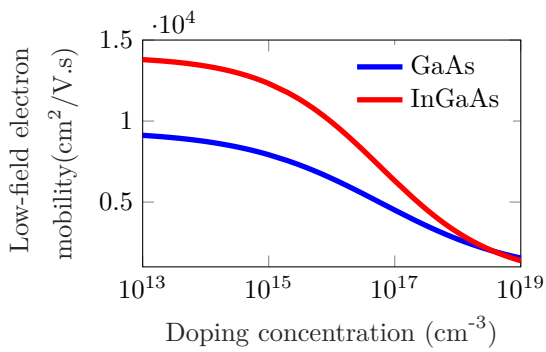

Figure 2.19: Electron mobility vs. doping concentration calculated using the empirical low-field mobility model at room temperature (300 K) [112].

ω_L = 292.1 cm^{-1}, ω_T = 268.7 cm^{-1}, damping factor Γ = 2.4 cm^{-1} and ϵ_∞ = 10.63. In the frequency range between ω_T and ω_L indicated by dotted lines, the real part of the permittivity, ϵ_r, becomes negative, and this band is referred to as the reststrahlen band. This band indicates a frequency region where energy is absorbed in the material.

Approaching the DC limit, the permittivity of GaAs is 12.9. In contrast, in the infrared regime, the permittivity is reduced to ϵ_r = 10.63 due to the inertial mass of the electrons as it cannot follow the rapid oscillations of the electric field, so polarisation effects become minimal. Thus, ϵ_r^∞ reflects the residual permittivity excluding atomic and displacement polarisation. This is of interest because this transition occurs at THz frequencies, and this section presents a simple model to calculate the frequency dependence at 3.5 THz, ϵ_r = 13.5 and 4.7 THz, ϵ_r = 14.1. However, since the suspended stripline circuit utilises ultra-thin dielectric GaAs membrane, this effect is minimal, as shown in section 3.1.3.

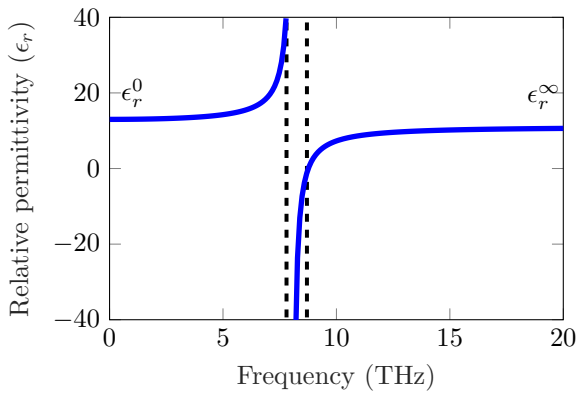

Figure 2.20: Frequency dependence of the relative permittivity ϵ_r for GaAs calculated from [111].

Chapter 3

Design and assembly of terahertz diode mixers

This chapter begins with an overview of waveguide-based mixers. Section 3.1.1 introduces a general approach to designing THz mixers, followed by determining the optimum embedding impedances for the diode at different frequencies in Section 3.1.2. The realisation of the mixer circuitry in a shielded suspended stripline and the suppression of higher-mode propagation in the channel are discussed in Section 3.1.3. Subsequently, the design of external components, such as integrated feed horns, IF impedance transformers, and high-precision machining of mixer blocks, are presented. Finally, a brief overview of the integrated circuit assembly in the mixer block is presented.

3.1 Design approach

A general guideline for designing THz mixers is presented here:

- Couple RF and LO power to the diode
- Present optimum embedding impedances at different frequencies to achieve low mixer conversion loss
- DC path for biasing the mixer if needed

- Design of planar filters that provide isolation between RF/LO and IF signals
- IF impedance transformer
- Evaluate mixer performance in terms of conversion loss, return loss for various bias and pump power conditions as well as frequency

For simplicity, a constant series resistance model was used in the large-signal harmonic-balance simulation while evaluating the mixers' performance. The rest of this chapter discusses how these sub-circuits and external components are implemented. The RF, LO and IF signal interfaces were assigned with wave ports as indicated in Fig. 3.1. A 50-Ω lumped port was used to obtain the diode's embedding impedance from the 3D-EM model. Alternatively, a coaxial waveguide probe could be used to measure the impedance [113].

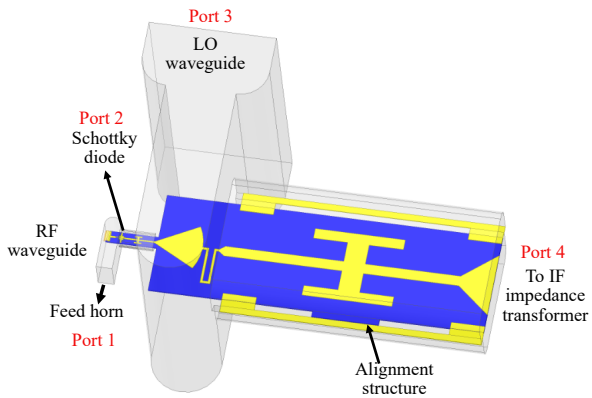

Figure 3.1: THz waveguide-based mixer [Paper F].

3.1.1 Waveguide-based mixers

The available output power in the THz frequency regime is scarce; refer to Fig. 2.2. Hence, finding a compact solution with low loss and good antenna coupling is critical. Open-structure mounts that integrate a planar antenna with the detector element are often preferred [114]. Since machining closed-structure mounts above 3 THz, where waveguide and channel dimensions

range from 25 to 50 μm, is generally considered challenging. However, advances in computer-aided design (CAD) tools and high-precision machining have enabled the realisation of waveguide-mounted mixers up to 4.7 THz [115], [116].

RF and LO signals can be efficiently coupled to the diode by directly integrating a feed horn with the waveguide, enabling excellent Gaussian beam coupling to external optical components [113]. The harmonic and fundamental mixers discussed in this thesis are waveguide-based, with the integrated GaAs membrane circuit suspended within an E-plane split block [Papers B-D], as shown in Fig. 3.1. The mixer blocks were machined in two halves; after assembling the IF impedance transformer components (quartz, PCB) and the integrated mixer circuitry, both blocks are fastened together as illustrated in Fig. 3.2. Since the waveguide is split along the maximum E-field of the fundamental mode in the waveguide TE_{10} as shown in the inset of Fig. 3.2, the blocks are referred to as E-plane split-blocks [117]. In this approach, the RF current along the split is zero, not affecting the waveguide performance.

In addition, it eases the machining process, as the waveguide is formed in two parts: each block has a channel with a 1:1 aspect ratio, which, put together, forms a standard rectangular waveguide (2:1). Another advantage of the E-plane split blocks is that they provide easier circuit integration. By inserting an E-field probe that couples the TE_{10} mode from the input waveguide to a quasi-transverse electromagnetic (TEM) mode in the planar circuit.

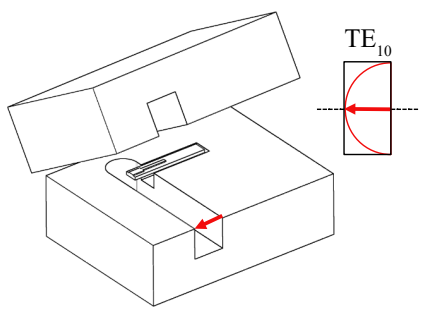

Figure 3.2: Illustration showing the mechanical housing of E-plane split blocks. Inset shows the maximum E-field of dominant TE_{10} mode in a rectangular waveguide.

3.1.2 Embedding impedances

Embedding impedances presented to the diode that offer low conversion loss at RF and LO frequencies were estimated using a large-signal harmonic balance simulation in a circuit simulator [Paper A]. Both diode geometry and the surrounding mixer circuitry influence the embedding impedance considerably. Hence, it is essential to tune the parameters to present an impedance closer to the ideal values estimated in large-signal modelling [Paper A, B]. Due to the diode's non-linear junction capacitance, optimum conversion loss and noise temperature occur at different operating conditions [74].

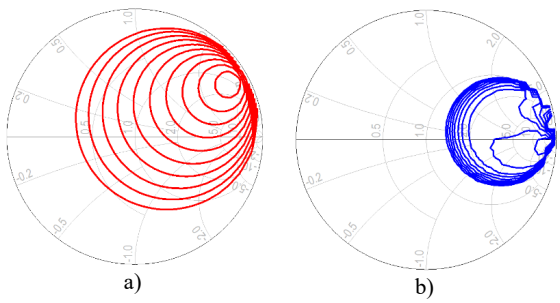

Figure 3.3: Embedding impedance. Smith chart showing the conversion loss L contours and the optimum embedding impedance at RF-3.5 THz (left) and LO-600 GHz (right).

Constant conversion loss and noise temperature contours computed using Siegel-Kerr code can be found here [118]. However, this work optimised the embedding impedances using constant conversion loss contours. The out-of-band frequencies or idlers were considered open-circuited (Z-mixer topology). Note: This is an ideal case; Z-mixers offer the lowest conversion loss since there is no current flow in the idlers. In Fig. 3.3a-b, the embedding impedances at RF and LO frequencies for an LO power of 2 dBm are presented here. A simulated conversion loss of 30 dB was obtained for an ideal Z-mixer with the following diode parameters: $\eta = 1.2$, $R_s = 50\ \Omega$ and $C_{j0} = 0.3$ fF and IF of 200 Ω. Note: No DC bias was applied, and mixer circuit losses were excluded from this analysis.

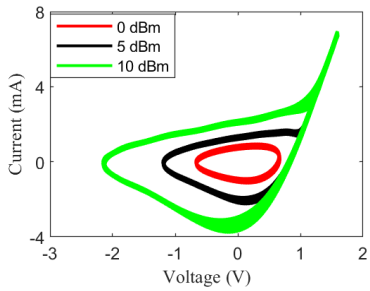

Figure 3.4: Time-dependent voltage and current waveforms for an ideal Y-mixer.

Time-domain voltage versus current is plotted for a Y-mixer with the same diode parameters described earlier for different LO power, as shown in Fig. 3.4, to ensure the mixer is not operated beyond the forward and reverse breakdown voltage. The reactive part dominates (capacitive current) for low LO pump power, and as the pump power increases, the resistive contribution increases in the forward bias region. [Paper A] also shows conversion nulls in Y-mixers arising from competing mixing products [119]. This phenomenon is later varied in the experimental characterisation of harmonic mixers and presented in Chapter 5 and [Paper B].

3.1.3 Shielded suspended stripline

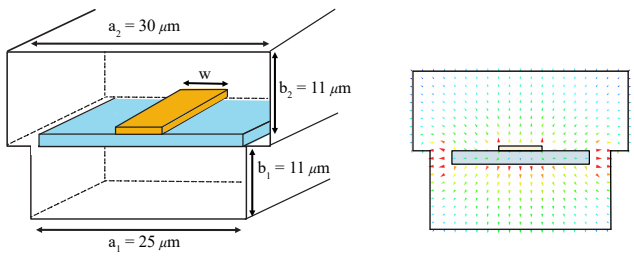

Figure 3.5: a) Schematic of the shielded suspended stripline of width w in the 3.5-THz RF channel. b) E-field distribution of the fundamental mode.

The cross-sectional view of the shielded stripline suspended in the channel is shown in Fig. 3.5. It consists of two conductors and, therefore, supports TEM wave propagation. However, due to the thin dielectric membrane, the wave propagates with different phase velocities, resulting in a quasi-TEM mode within the channel. The top channel was wider than the bottom to make the design less sensitive to misalignment between two halves.

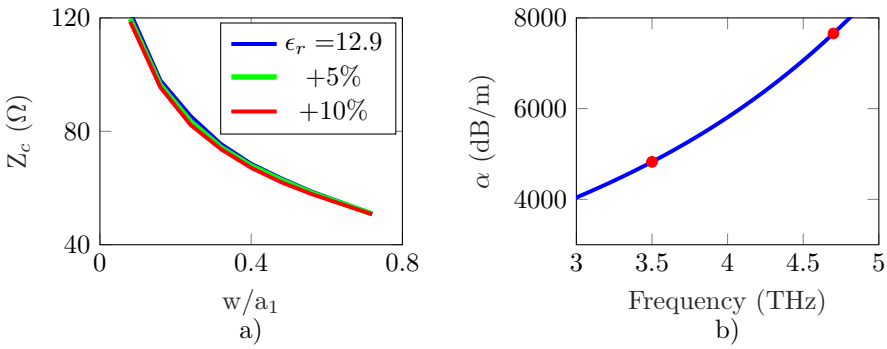

Figure 3.6: Suspended stripline a) Characteristic impedance versus stripline width normalised to the channel width (w/a_1). b) Attenuation versus frequency for a stripline of $w/a_1 = 0.32$ in the channel Fig. 3.5.

Based on the GaAs dispersion model presented in Chapter 2, the relative permittivity ϵ_r of the membrane was varied by up to 10%, as illustrated in Fig. 3.6a. The stripline's characteristic impedance Z_c (power-current definition [120]) was then calculated for various stripline widths w, normalised by the channel width a_1. The estimated loss tangent was approximately 0.0009 and 0.001 at 3.5 THz and 4.7 THz, respectively and was not included in this study.

3.1.3.1 Suppression of higher-order modes

To ensure only the fundamental mode propagates in the channel, the width of the channel is designed to be smaller than $\lambda/2$, which restricts the propagation of higher-order waveguide modes. Fig. 3.7 shows the E-field distribution of the 2^{nd} mode and 3^{rd} mode in the channel.

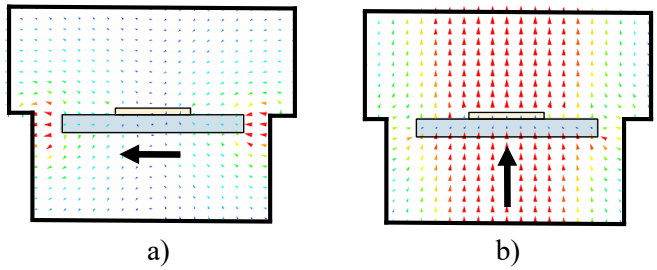

Figure 3.7: E-field distribution of first two waveguide modes in the channel.

The width of the stripline determines the onset of the 2nd mode in the channel. The cut-off frequency of the higher-order modes is plotted versus the stripline width normalised to the channel width as shown in Fig. 3.8a. Since the E-field distribution of the 3rd mode is perpendicular to the stripline, it is not sensitive to the width variation. Hence, the cut-off frequency of the 3rd mode is constant, as shown in Fig. 3.8a. Figure 3.8b shows the cut-off frequency of the first three propagating modes in the channel for a particular case ($w/a_1 = 0.32$).

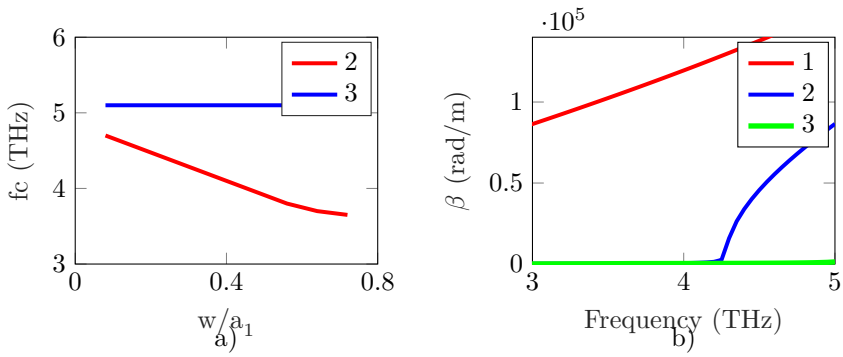

Figure 3.8: Higher-order modes. a) Cut-off frequencies of the 2nd and 3rd modes in the channel versus stripline width. b) Phase constant versus frequency for fundamental, 2nd, and 3rd modes for stripline $w/a_1 = 0.32$ in the 3.5-THz channel.

3.1.3.2 Conductor loss

Due to the ultra-thin GaAs membrane, variations in ϵ_r have a minimal impact on the transmission line characteristics. For $w/a_1 = 0.32$, attenuation was calculated from the 3D-EM model as a function of frequency and is presented in Fig. 3.6b.

As depicted in Fig. 3.5b, the fundamental mode's E-field distribution is concentrated along the centre conductor, with weaker field strength at the periphery. Therefore, the surface roughness of the stripline has a significant effect than that of the channel's surface roughness, which arises from machining. The following equation approximates the effect of surface roughness,

$$\alpha_c' \approx \alpha_c \left(1 + \frac{2}{\pi} \arctan\left[1.4 \left(\frac{\Delta_{\mathrm{RMS}}}{\delta_s}\right)^2\right]\right) \tag{3.1}$$

where δ_s is the conductor skin depth (42 nm at 3.5 THz and 36 nm at 4.7 THz). This surface roughness approximation is based on microstrip lines [121].

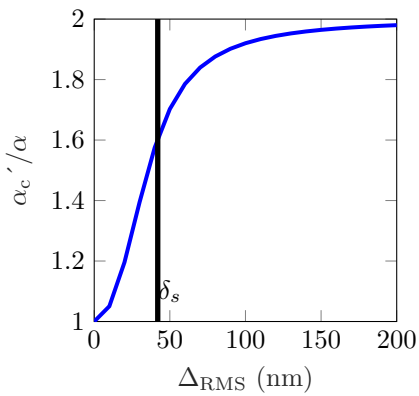

Figure 3.9: Conductor loss as a function of surface roughness of gold stripline at 3.5 THz.

3.1.4 Planar band-stop filters

Broadband filters are essential to maximise the coupling of incoming signals to the diode and enhance mixer sensitivity. They prevent signal leakage and

ensure isolation between the RF, LO, and IF chains. Stepped-impedance filters feature a simple topology with alternating high- and low-impedance sections. Alternatively, hammer-head sections can provide efficient rejection with a compact layout.

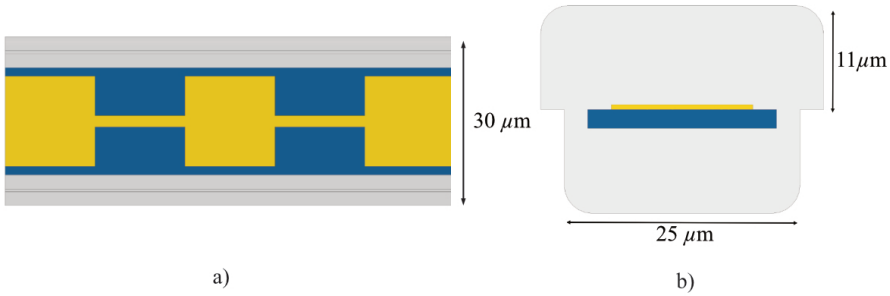

Figure 3.10: Stepped-impedance filter. a) Picture of the EM model. b) Cross-section of the RF channel.

3.1.4.1 Stepped impedance filter

Stepped impedance filters consist of alternating high- and low-impedance line sections, as shown in Fig. 3.10. To achieve high isolation, the ratio between the high and low impedances should be as high as possible, and the length of each section should be approximately ($\lambda_g/4$). The 5^{th} order stepped impedance provided isolation of about 18 dB at the centre frequency (3.5 THz) [Paper B]. Fig. 3.10 shows the cross-section of the RF channel showing the stepped impedance filter defined on a 2-μm GaAs membrane. The top and bottom channels have different widths to account for the misalignment of the top and bottom split blocks. The rounded corners arising from the milling process are considered in the 3D-EM model design. The cut-off frequency of the 2^{nd} mode is $\approx$ 3.6 THz and is determined by the stripline width of the low-impedance line, refer Fig. 3.8.

3.1.4.2 Hammerhead filter

Higher-order stepped-impedance filters offer improved signal suppression but result in an electrically long circuit, which contributes to high loss in the

passband. Therefore, the hammer-head filter is suitable for meeting these requirements using only one section [Paper B, F]. Figure 3.11 displays a top view of the planar hammer-head filter suspended within the channel using beam leads.

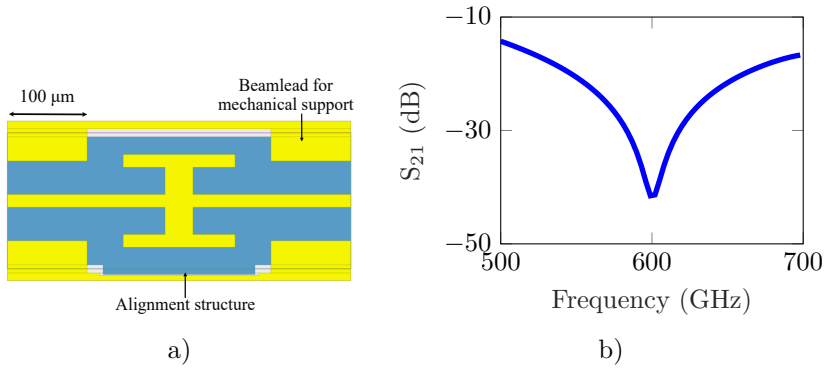

Figure 3.11: Hammer-head filter. a) 3D-EM model of the hammer-head filter. The gold beam leads provide grounding, heat transfer, and mechanical support. The asymmetrical GaAs membrane aids in precisely aligning the circuit in the block. b) S_{21} versus frequency.

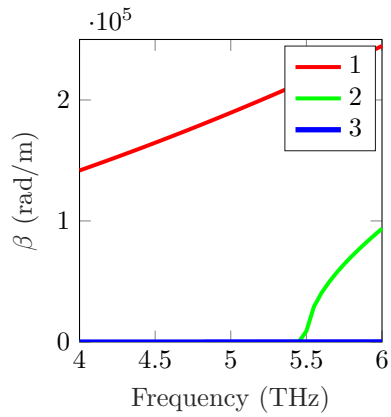

Figure 3.12: 4.7-THz hammer-head filter. Phase constant of fundamental and higher-order modes versus frequency.

Beamleads provide efficient support, heat transfer, electrical grounding, and precise circuit alignment in the E-plane mixer split block. Fig. 3.11 (right) shows the filter response of the designed hammer-head filter with suppression better than -20 dB between 550 GHz to 650 GHz and isolation of about 40 dB at the centre frequency. For a 4.7-THz harmonic mixer, see Fig. 5.27, the hammer-head filter was implemented as an RF choke, and Fig. 3.12 shows the phase constant first three higher-order modes in the RF channel, Paper [F] and [116].

3.1.5 IF impedance transformer

An impedance transformer is needed to match the mixer IF impedance to the 50-Ω. As discussed in paper [A], the optimal IF impedance was approximately 1000 Ω, but realising this as a microstrip line on a Rogers 4003B PCB is impractical; therefore, 150 Ω was selected as IF impedance instead.

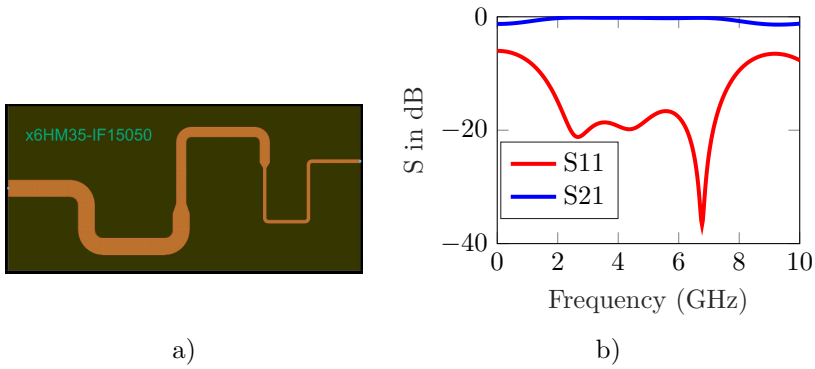

Figure 3.13: IF impedance transformer. a) Picture showing the layout of the three-section Chebyshev 150 to 50-Ω impedance transformer. b) Return loss and insertion loss of the three-section Chebyshev impedance transformer.

A quarter-wavelength impedance transformer would provide a very narrow bandwidth, so to broaden the bandwidth, multi-section impedance transformers like Chebyshev and binomial are commonly employed [122]. The simulated insertion loss of the three-section Chebyshev transformer was under 0.3 dB across the 1.5 GHz to 7 GHz frequency range, with a return loss better than

15 dB from 2 GHz to 7.5 GHz, as shown in Fig. 3.13. Integrating the LNA with the mixer module, as demonstrated in [123], is advantageous to achieve a compact front-end receiver module. This integration helps minimise ripples caused by the mismatch between the mixer and LNA.

3.1.6 Integrated feed horns

In this thesis, two RF feed horn designs were employed: diagonal and pyramidal horns due to their seamless integration with rectangular waveguides and ease of machining at THz frequencies. For the diagonal horn, the standard design described by Johansson and Whyborn [124]. The 3.5-THz diagonal horn with an aperture size of 384×384 μm^2, corresponding to a flare angle of 5.4°, resulted in a simulated directivity of about 23 dBi as shown in Fig. 3.14a and return loss below 30 dB as shown in Fig. 3.14b. The aperture dimensions correspond to a theoretical Gaussian beam waist of 165 μm [63].

The pyramidal horn had an aperture size of 330×230 μm^2, and a length of 1.6 mm was integrated with a WM-48 rectangular waveguide. The peak copolar directivity was about 22.5 dBi, and return loss was about 30 dB at the centre frequency, as shown in Fig. 3.15a-b. The copolar radiation pattern of both diagonal and pyramidal horn antennas is presented in Fig. 3.16a-b. Diagonal horns have side-lobe levels (15 dB) in the D-plane ($\phi = 45°$) and the

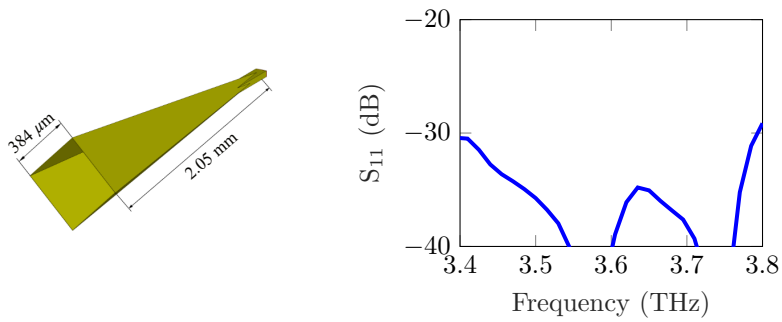

Figure 3.14: 3.5-THz diagonal horn. a) 3D-EM model of the feedhorn. b) Simulated return loss versus frequency.

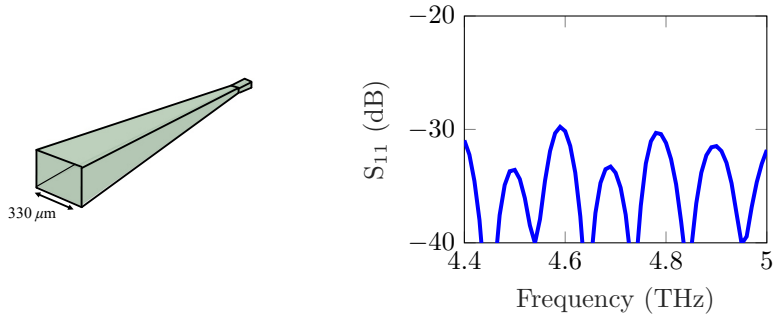

Figure 3.15: 4.7-THz Pyramidal horn. a) 3D-EM model of the pyramidal horn b) Simulated return loss versus frequency.

pyramidal horns has in the H-plane ($\phi = 90°$).

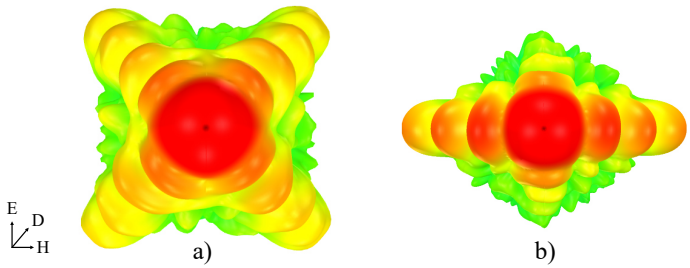

Figure 3.16: Co-polarisation radiation pattern of perfectly aligned antennas a) Diagonal horn b) Pyramidal horn.

3.2 Fundamental mixers

With all the sub-circuits optimised, the full EM model of the 3.5-THz fundamental mixer is shown in Fig. 3.17. The E-field probe's dimension and the waveguide backshort position are optimised for maximum coupling of RF signal to the diode. The E-probe is also extended as a beamlead providing RF/DC ground. The beamlead will be clamped when the split-block halves

are assembled, aiding heat dissipation. The fundamental mixer's design is more straightforward than the harmonic mixer because RF and LO signals are coupled to the diode via the same waveguide with an integrated feed horn. A Martin-Puplett diplexer spatially overlapped the RF (hot/cold loads) and LO signals (QCL) during experimental characterisation.

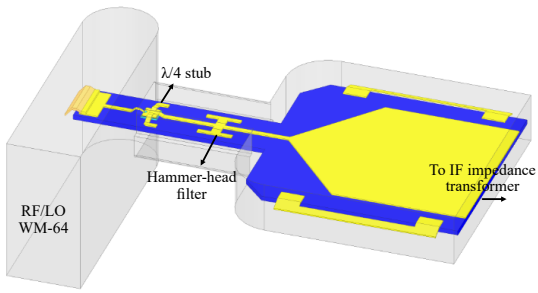

Figure 3.17: Picture of the full 3D-EM model of the 3.5-THz fundamental mixer

A quarter-wave stub was placed directly on the mesa in addition to the hammer-head filter, which improved the isolation, thereby reducing mixer conversion loss. The 4.7-THz fundamental mixer is a scaled version of this design. Fig.5.18 shows the scanned electron micrograph of the 3.5 THz and 4.7 THz fundamental mixers, highlighting the quarter-wave stub placed on the mesa. The large-signal harmonic balance simulation results of fundamental mixers and video responsivity measurements are presented in Chapter. 4.

3.3 Harmonic mixers

For a n^{th} harmonic mixer, the LO chain must be designed at a $1/n$ of the RF, making the simulation of the full EM model computationally intensive and challenging. To accurately predict the performance of harmonic mixers, it is essential to consider all the idlers spanning across a wide frequency band of n-octaves; refer to Section 3.3.1 about terminations at idlers. The 3D-EM model of the RF chain of a harmonic mixer with an RF waveguide of height b, width a, and backshort l is shown in Fig. 3.18a. The inset shows

the air-bridged finger, and the Schottky junction is modelled using a 50-Ω lumped port. Fig. 3.18b shows the RF embedding impedance presented to the diode versus frequency from 3.48 THz to 3.52 THz; the mark indicates the impedance at the centre frequency 3.5 THz.

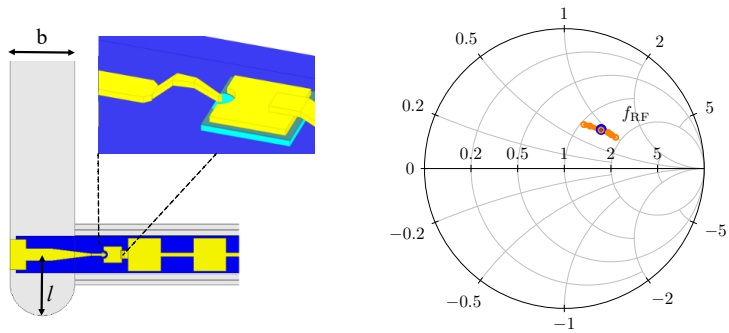

a) b)

Figure 3.18: Harmonic mixer. a) 3D-EM model of the RF chain showing the RF waveguide, RF E-probe and the diode. The inset shows the air-bridged finger and the mesa. b) RF embedding impedance presented to the diode from 3.48 THz to 3.52 THz.

Fig. 3.19 shows the full 3D-EM model of the 3.5-THz harmonic mixer, including the RF/LO waveguides and channels and the integrated mixer circuit, including the planar Schottky diode and choke filters. Note: to reduce the computational time, the feed horn and the LO access waveguide were excluded from the simulation. The 4.7-THz, ×8 harmonic mixer design is shown in Fig. 3.1, which has a WM-48 RF waveguide that is integrated into a pyramidal horn, and the RF choke is designed using the hammer-head filter [Paper E]. The simulation results of mixer performance are summarised in Chapter. 5.

3.3.1 Embedding impedances at idler frequencies

As mentioned in Section. 2.3, a mixer utilising higher harmonics for operation has a reduced sensitivity. Reactively terminating the idlers will result in improved mixer performance at the expense of having a complicated design.

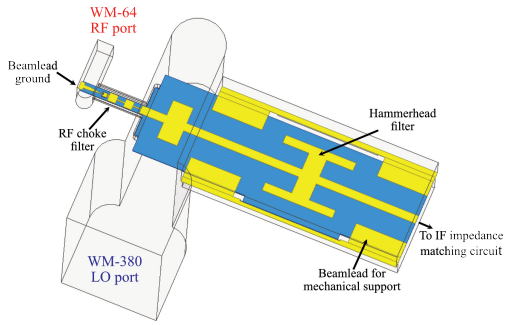

Figure 3.19: Full 3D-EM model of the 3.5-THz, ×6-harmonic Schottky diode mixer.

Given the fabrication challenges for circuits above 2 THz, specific measures were not implemented to terminate the idler frequencies reactively. The embedding impedances presented to the diode at different idler frequencies are presented in the Smith chart Fig. 3.20 for the circuit shown in Fig. 3.19. A blue dot indicates the optimum embedding impedance presented at the LO frequency.

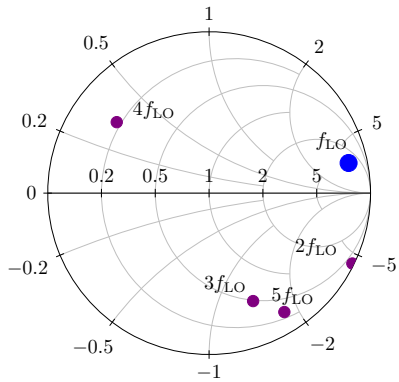

Figure 3.20: Embedding impedances presented to the diode at different idler frequencies

3.4 Robustness analysis

Sensitivity analysis was performed to check the robustness of the mixer design. The parameters with critical tolerances are varied by 10% of their original value to approximate the partial derivatives [125]. The relative sensitivity coefficient is given by,

$$S_x^L = \frac{\Delta L/L_0}{\Delta x/x_0} \tag{3.2}$$

where $\Delta L = L_x - L_0$ denotes the change in the conversion loss, L_0 the nominal conversion loss, Δx the relative variation of the parameter in the study, and x_0 the nominal value of the parameter. The relative sensitivity coefficient was then calculated by studying the harmonic mixer conversion loss and is given in [Paper B]. The diode ideality factor (η) has the strongest influence on the conversion loss of the mixer due to its influence on the diode non-linearity. A similar analysis for the 4.7-THz fundamental mixer design is summarised in [126].

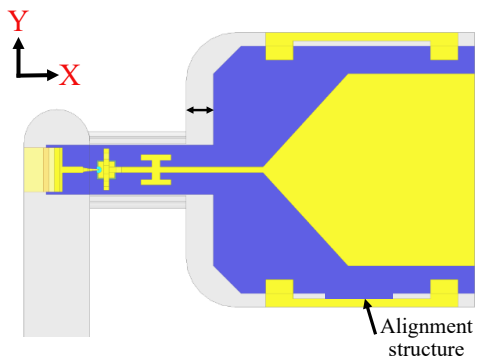

Figure 3.21: 3D-EM model of the 4.7-THz fundamental mixer circuit misaligned by 5 μm in the waveguide housing.

The sensitivity of the mixer's performance to misalignment caused during circuit assembly is discussed in Chapter 4. The integrated mixer circuitry was manually assembled in the mixer block using a microscope, with 1-2 µm alignment tolerances. Achieving such precise alignment is highly challenging. Although alignment cavities, see Fig.3.24 and asymmetric membrane designs

were implemented to aid the alignment, the circuit remains susceptible to misalignment in the +x-direction, as shown in Fig. 3.21.

3.5 Circuit fabrication

Fig. 3.23 and 3.22 shows the scanned electron micrograph of the planar, integrated fundamental mixer circuit on the supporting GaAs substrate fabricated by Mr. Vladimir Drakinskiy. [Paper B] presents the detailed fabrication process.

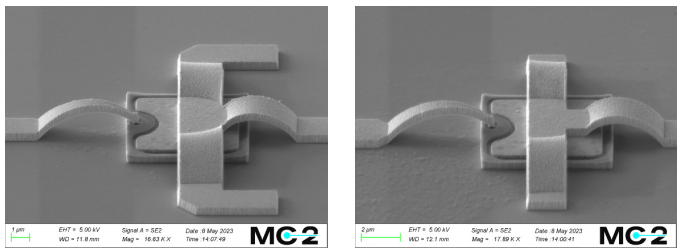

Figure 3.22: Scanned electron microscope (SEM) picture of 3.5/4.7 THz fundamental mixers highlighting the $\lambda/4$ stub and mesa.

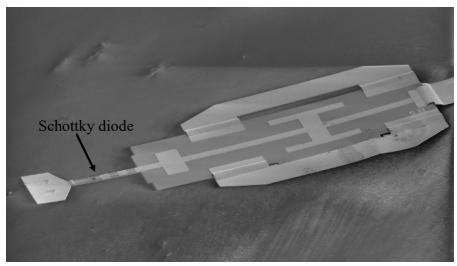

Figure 3.23: SEM picture of the 3.5-THz, ×6-harmonic mixer after releasing from the supporting substrate.

3.6 Mixer housing

The mixer was machined in an E-plane split aluminium block using a high-speed, micrometre precision CNC milling tool (KERN Evo) by Mr. Mats Myremark. For details of the milling tools used in this process, refer to [Paper B]. The mixer blocks were cleaned with an acetone and isopropanol solution in an ultrasonic bath, etched, and finally, sputtered with a 0.5-μm gold layer as shown in Fig. 3.24a. The sidewall of the mixer block that includes the diagonal horn aperture was slanted by a 10° angle to redirect the reflected incoming signal as shown in Fig. 3.24b.

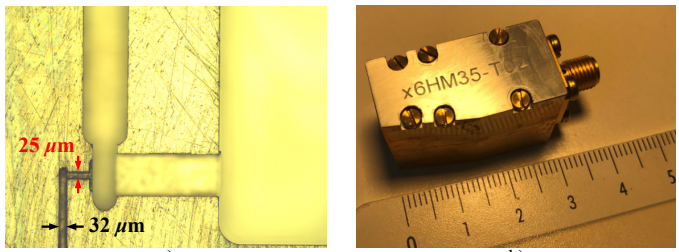

Figure 3.24: a) The micrograph of the harmonic mixer's E-plane split block (bottom part) shows the WM-64 waveguide and 25 μm channel. b) Photograph of the harmonic mixer block.

This was modified in the later iterations to reduce the optical feedback between the mixer and QCL. Fig. 3.25 shows the CAD model of the 4.7-THz, $\times 8$ harmonic mixer with integrated pyramidal horn and the assembled mixer is shown in Fig. 5.10.

3.7 Circuit assembly

The integrated harmonic and fundamental mixer circuits were assembled on an E-plane split block. The beamleads aid in heat transfer from the diode to the surrounding metal and provide mechanical support as the integrated circuit is suspended in the block, as shown in Fig.3.26. The IF beamlead is punched into the quartz circuit using a ceramic wedge. The quartz circuit and the PCB are connected using a small bond wire, and finally, the SMA connector

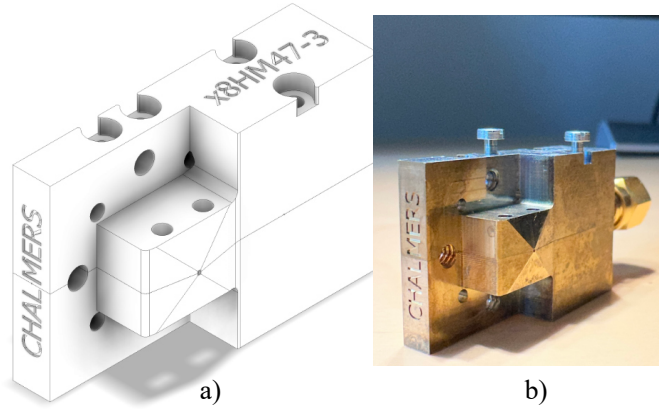

Figure 3.25: a) CAD model of the 4.7-THz, ×8 harmonic mixer. b) Photograph of the machined 4.7-THz harmonic mixer blocks with integrated pyramidal horn.

is soldered to the PCB board. The harmonic mixer block is connected to the 600-GHz LO multiplier chain as shown in Fig. 3.27b.

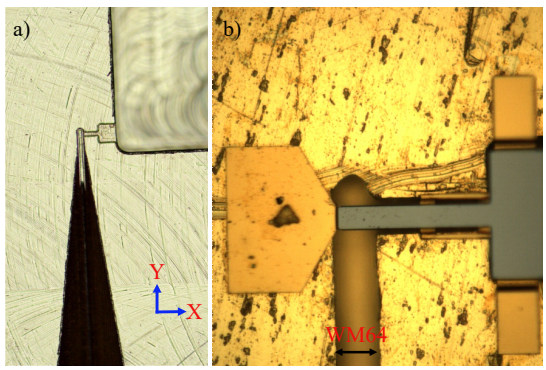

Figure 3.26: 3.5-THz fundamental mixer a) Aluminium block sputtered with gold b) Integrated mixer circuit assembled on an E-plane split-block.

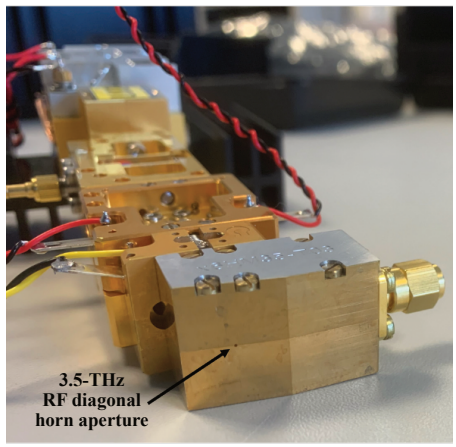

Figure 3.27: Photograph of the harmonic mixer connected with the 600-GHz, LO multiplier chain. The aperture of the 3.5-THz diagonal feedhorn is indicated in the picture.

Chapter 4

Diode and mixer characterisation

This chapter outlines the measurement techniques employed to assess diodes and mixers' DC and RF performance in this thesis.

4.1 DC characterisation

Estimation of parameters such as diode series resistance R_s, ideality factor η, and saturation current I_s are crucial to model the Schottky-barrier diode's non-linear DC behaviour. For accurate R_s measurements, removing the additional resistance (e.g., probe contact resistance) is essential, which is achieved by using four-point or Kelvin probe sensing. It consists of force-and-sense probe pairs used for current carrying and voltage sensing, respectively, as shown in Fig. 4.1a. A static current-voltage (I-V) measurement is carried out by either varying the DC voltage or current, refer to Fig. 4.1b. Self-heating effects in semiconductor devices considerably affect device performances [127]. In particular, the extraction of these parameters is greatly influenced by temperature variations in the Schottky junction. To isolate the effects of self-heating, pulsed I-V measurement is widely used. A voltage or current pulse with a width less than the device thermal time constant τ_{th} is applied across the diode. The thermal time constant is $\tau_{th} = R_{th}C_{th}$, where, R_{th} and C_{th}

are thermal resistance and capacitance, respectively.

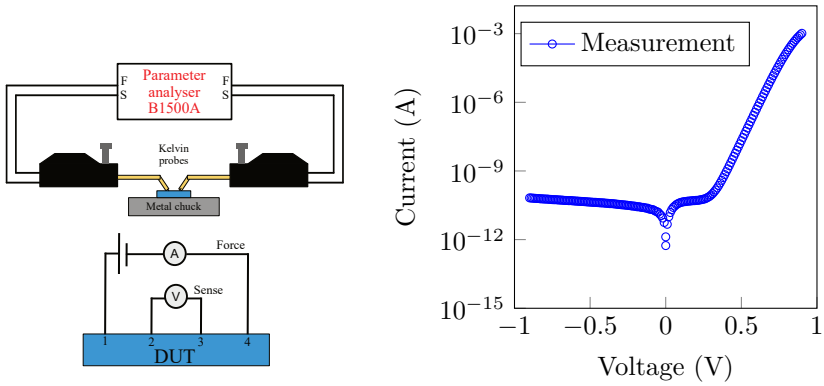

a) b)

Figure 4.1: DC characterisation. a) Illustration of the DC measurement setup and the principle of four-terminal sensing. b) $I-V$ measurement of a Schottky diode with sub-micron anode area.

Before releasing the integrated mixer circuits from the wafer, static I-V measurements were performed on-wafer using Kelvin probes at room temperature. The following parameters were extracted [128] by fitting the IV curves from the ideal diode model with the measurements shown in Fig. 4.1b.

4.1.1 Direct diode model parameter extraction

The diode I-V equation for forward bias $V_j > k_B T/q$ can be simplified to,

$$I_d = I_j = I_s \exp\left(\frac{qV_j}{\eta k_B T}\right) \tag{4.1}$$

where, $V_j = V_d - I_d R_s$. Typically, the ideality factor η is extracted from the slope of the I-V curve in logarithmic scale where R_s can be neglected [129]. From the two measured points (I_1, I_2) highlighted in Fig. 4.2, η was extracted,

$$\eta = \frac{q}{kT}\frac{(V_2 - V_1)}{\ln(I_2/I_1)} \tag{4.2}$$

The saturation current is given by,

$$I_s = \frac{I_1^{(V_2/V_2-V_1)}}{I_2^{(V_1/V_2-V_1)}} \tag{4.3}$$

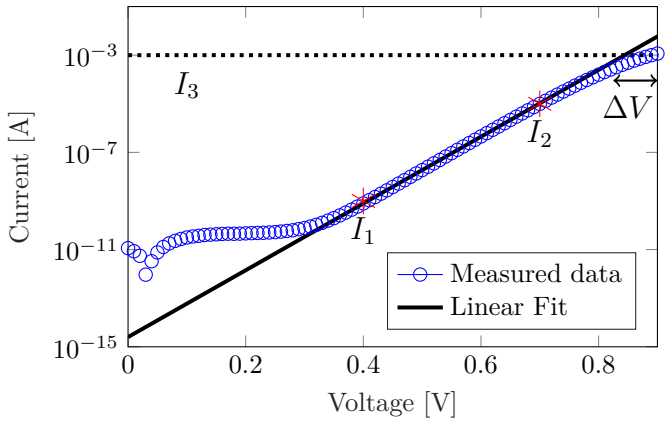

Figure 4.2: Direct extraction. I-V measurement data of 3.5-THz harmonic Schottky barrier diode mixer circuit with anode area 0.11 μm^2.

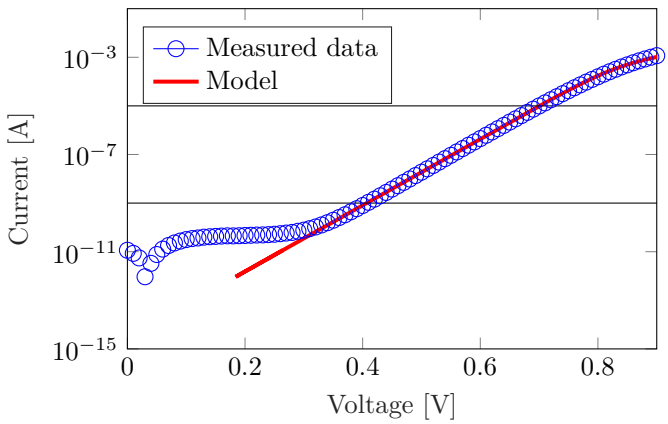

Figure 4.3: Least-square method. The horizontal lines indicate the range for ideality factor extraction.

The effect of series resistance is observable in the forward bias, refer Fig. 4.2 and is estimated by,

$$R_s = \frac{\Delta V}{I_3} \tag{4.4}$$

The extracted diode DC-parameters by direct method are $\eta = 1.3$, $R_s = 60\ \Omega$, and $I_s = 5\ fA$. Further optimisation is carried out using a least-square method shown in Fig. 4.3. The extracted diode DC-parameters by least-square method are $\eta = 1.25$, $R_s = 50\ \Omega$ and $I_s = 3\ fA$.

4.2 Conversion loss measurements

Conversion loss describes how efficiently a mixer converts the energy from the input RF frequency to the output IF frequency. The mixer conversion loss is given as the ratio of the IF output power to the RF input power for a given LO pump condition:

$$L_m = \frac{P_{\mathrm{RF,in}}}{P_{\mathrm{IF,out}}} \tag{4.5}$$

where, $P_{\mathrm{RF,in}}$ and $P_{\mathrm{IF,out}}$ are input RF frequency and output intermediate frequency respectively. When no energy is dissipated in the out-of-band frequencies, the theoretical limit of the conversion loss is 3 dB for a DSB mixer [130]. The mixer conversion loss is degraded due to various factors such as diode series resistance, self-heating effects [131], power loss into frequency bands other than the IF, and loss due to reflection at the input and output ports. Note: Frequency converters utilising higher harmonics for mixing have higher conversion loss.

4.2.1 Power-meter method

This is the most common method for characterising a mixer's conversion loss. External signal sources generate RF and LO signals. The desired IF signal is obtained using a band-pass filter. Absolute power measurements of the IF and RF signals are carried out using a power meter or spectrum analyser to estimate mixer conversion loss. Insertion loss of the cables and band-pass filter is estimated using a VNA.

4.2.1.1 Absolute power measurement

Absolute power measurements at THz frequencies have been challenging due to slow response time, atmospheric attenuation, poor sensitivity and temperature drift. This section describes the protocol for guided (waveguide) and free-space power measurements at millimetre-wave and terahertz frequencies [132].

Erickson power meter

The Erickson power meter is a calorimeter-based waveguide power sensor that works from ≈75 GHz to THz range [133]. It measures the temperature rise of a well-matched wideband absorber corresponding to the applied input power. The main advantage of calorimetry is that it is insensitive to frequency. However, for measurements above the WR-10 band (75 - 110 GHz), a waveguide taper transition is required to connect the power meter head to the device under test (DUT). Also, it is crucial to consider the losses in the 1-inch WR-10 waveguide attached to the power meter head and the waveguide taper.

Thomas Keating power meter

The TK power meter is based on an acousto-optic sensor for free-space measurements ranging from 30 GHz to 5 THz. The system has noise equivalent

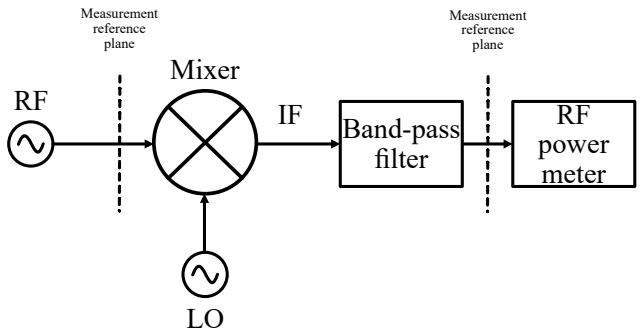

Figure 4.4: Schematic of the power-meter method.

power (NEP) of about 5 μW Hz$^{1/2}$. The suggested power measurement protocol is as follows:

- The beam should be amplitude modulated at its source or by a mechanical chopper operating at 10 to 50 Hz modulation frequency.
- The incoming signal is incident at the Brewster angle to avoid reflections from the power meter sensor head.
- Use frequency-dependent window loss correction.

4.2.2 Three-mixer method

The 'three-antenna' method proposed by Beatty [134] was adapted to characterise mixers. The method for conversion loss extraction is explained in this section.

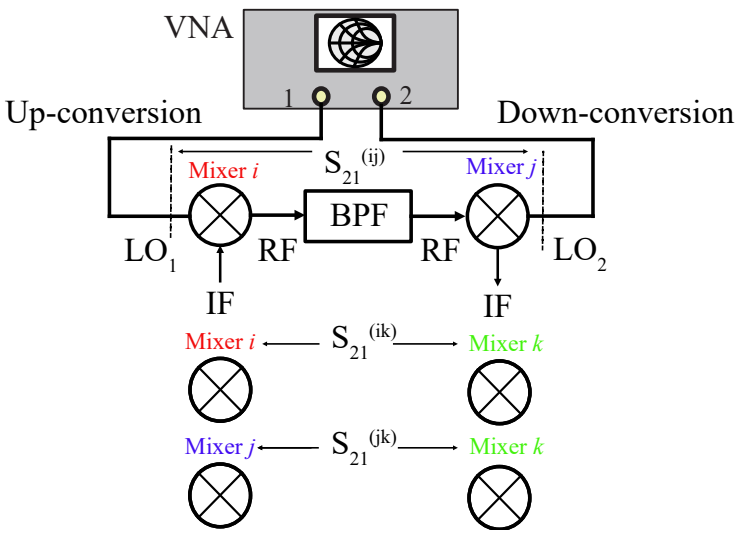

Figure 4.5: Schematic of the three-mixer measurement method.

By the 'magnitude reciprocity' principle, the mixer up- and down-conversion loss are assumed to be the same ($|L_i^{up} = L_i^{down}|$). Mixer i is used for the frequency up-conversion (i.e.) to generate an RF signal $f_{RF} = f_{LO} \pm f_{IF}$.

Then, the RF signal is down-converted by mixer j. This process is repeated for three different mixers, and the total signal transfer loss is measured. It results in a system of linear equations ($Ax = b$) as shown below, and the conversion loss of the three mixers L_i, L_j and L_k can be obtained. In ideal cases, when the mixer conditions are identical, we have a square matrix with three measurements and unknowns, yielding a unique solution.

$$\begin{bmatrix} 1 & 1 & 0 \\ 1 & 0 & 1 \\ 0 & 1 & 1 \end{bmatrix} \begin{bmatrix} L_i \\ L_j \\ L_k \end{bmatrix} = \begin{bmatrix} L_i^t \\ L_j^t \\ L_k^t \end{bmatrix}$$

Fig. 4.5 shows the simplified schematic of the 'Three-mixer' method; at low frequencies, a band-pass filter can achieve single side-band mixer operation. However, at THz frequencies, due to a lack of filters, a frequency offset was introduced in one of the LO frequencies $f_{LO}+2f_{IF}$ [Paper C]. However, in the measurements described in paper [C], one of the mixers was measured under different LO conditions. Therefore, it resulted in a non-square matrix, and the least-square method was used to solve the equation system.

4.2.3 Y-factor method

The Y-factor method is a standard measurement technique to measure the noise temperature of a receiver [122], and a simplified schematic is shown in Fig. 4.6.

Two blackbody calibration targets with known temperatures are employed, and the system output power is measured for both. By assuming the receiver

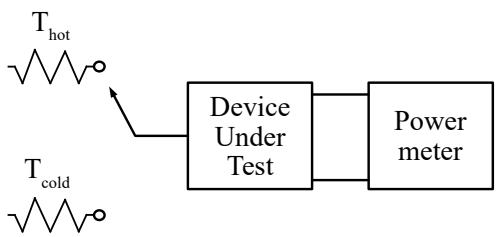

Figure 4.6: Schematic of Y-factor measurement setup.

has a linear response to change in the input noise temperature, the receiver noise temperature is calculated as follows:

$$T_{rec} = \frac{T_{hot} - YT_{cold}}{Y - 1} \quad \text{and} \quad Y = \frac{P_{hot}}{P_{cold}} \tag{4.6}$$

Performing noise temperature measurements above 1 THz is challenging due to high mixer noise temperature, atmospheric attenuations, and poor Gaussian beam coupling [31]. The lock-in technique described in [31] allows repeatable measurements, improves the system accuracy, and can evaluate high DSB receiver noise temperature ($\approx 500\,000$ K) [118].

In a heterodyne receiver, the mixer is followed by an IF amplifier, and then the receiver noise temperature is given by,

$$T_{rec} = T_M + L_M T_{IF} \tag{4.7}$$

where T_M and L_M are the mixer noise temperature and conversion loss and T_{IF} is the noise temperature of the IF amplifier. The mixer conversion loss can be determined by measuring a range of IF noise temperatures by placing an attenuator in the IF chain. Using linear least square fit, T_M and L_M are obtained.

4.3 Video detection

Video detection is a simple method of using a diode to detect a signal by rectifying the input AC signal to create a DC voltage proportional to the signal power. The DC voltage or video response V_R, as shown in Fig. 4.7, is the shift in the diode's IV response from un-pumped (without LO signal) to pumped (with LO signal) condition. The voltage responsivity of a diode is given as,

$$\Re_v = \frac{V_R}{P_{in}} \tag{4.8}$$

For an ideal diode with no parasitic elements, the video response is given by [135],

$$V_R = \frac{\eta kT}{q} \ln\left[J_0\left(\frac{qV_{ac}}{\eta kT}\right)\right] \tag{4.9}$$

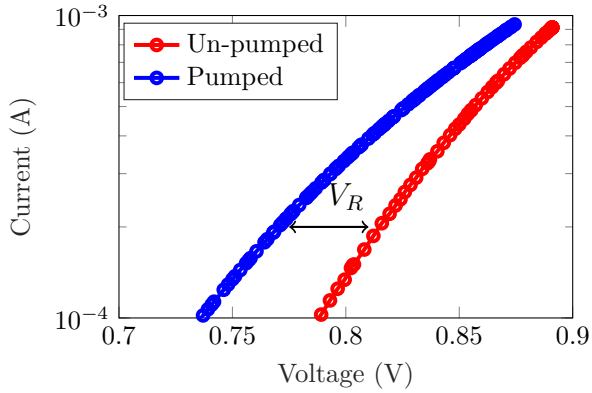

Figure 4.7: Comparison of a fundamental mixer's pumped and un-pumped measured IV curves with 0.1 μm^2 Schottky barrier diode at 3.5 THz.

where J_0 is the modified Bessel function of the first kind, V_{ac} is the junction voltage's AC component. The two limits of this equation,

$$\ln\left[J_0(CV_{ac})\right] \approx \begin{cases} \left(\frac{CV_{ac}}{2}\right)^2, & \text{for } (CV_{ac}) \to 0 \\ CV_{ac}, & \text{for } (CV_{ac}) \to \infty \end{cases} \tag{4.10}$$

The video response is proportional to the power (square-law region) for small AC voltages. For large AC voltages, it is proportional to the voltage or square root of the power (linear-detection region).

Chapter 5

Results

The first part of this chapter presents the experimental setup for characterising THz harmonic mixers from 2-5 THz. Measurement results are compared with the large-signal harmonic balance simulations to gauge the accuracy of high-frequency modelling techniques employed in this work and determine the cause of the discrepancies. The challenges in realising 3.5/4.7 THz fundamental mixers are discussed. Direct detection and preliminary noise temperature measurement results are presented. In the final part of the thesis, the impact of E-plane misalignment on the THz diagonal horn is studied, the near-field antenna measurement setup is described, and the results are compared to the simulated far-field radiation pattern of a WM-570 diagonal horn, showing excellent agreement.

5.1 Harmonic mixers

Before releasing the integrated mixer circuits from the substrate, static I-V measurements were performed on-wafer using Kelvin probes at room temperature. Following this, the integrated mixer circuit was mounted onto the mixer block using the alignment structures, as shown in Fig. 5.1. Note the Kelvin probe marks on the beamlead to the left. The top and bottom halves were aligned with the aid of mechanically integrated guide structures, and finally, I-V measurements were conducted to verify the functionality of the mixer.

The RF characterisation setup for evaluating the harmonic mixer is de-

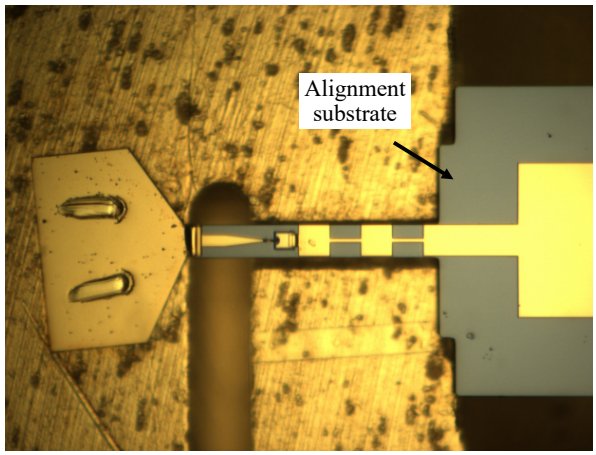

Figure 5.1: Micrograph of the integrated harmonic mixer circuit with 0.11 μm^2 Schottky contact area assembled on the mixer block (x6HM35-01).

scribed here. The 3.5/4.7-THz QCLs are placed in a compact Sterling cryocooler, which provides thermal stabilisation as shown in Fig. 5.2a. The typical operating temperature of the QCL is around 50 K with temperature stability $\approx$ 1 mK. The signal from the QCL was focused on the harmonic mixer using a Polymethylpentene (TPX) lens. The harmonic mixer has an integrated diagonal horn that couples the incoming THz signal to the single-ended Schottky diode. The harmonic mixer was pumped using a 600-GHz, $\times$64-active multiplier chain based on three cascaded Schottky $\times$2 MMIC multipliers from Chalmers University of Technology and a commercial $\times$8 active E-band drivers from Millitech (Smiths interconnect). The available output power of this multiplier chain versus frequency is presented in [Paper B].

The harmonic mixer and the last multiplier stage are connected through WM-380 (WR-1.5) waveguide interface with UG-387 flange designation [136]. The output power from the 600-GHz multiplier chain is measured using an Erickson power meter (PM5). A bias-tee was used to apply DC voltage to the harmonic mixer. The IF signal generated from the mixer is amplified using a low noise amplifier (LNA), and the signal is read out using a spectrum analyser.

5.1.1 3.5-THz, ×6-harmonic mixer

The THz beam from the QCL was focused using a TPX lens with an optimum beam waist of 165 μm [63]. The beam profile was evaluated using a microbolometer camera, as shown in Fig. 5.3. The side lobes are caused due to the diffraction from the lens.

The harmonic mixer connected to the 600-GHz multiplier chain was then aligned using an XYZ micrometre stage. The absolute power measurement was carried out using a Thomas Keating power meter at the mixer interface, eliminating the need to de-embed the atmospheric attenuation at 3.5 THz and loss from the lens. The THz beam from the QCL was amplitude-modulated using a mechanical chopper with a frequency of 15 Hz. The TPX lens was used to focus the beam, and the power meter head was aligned so the incoming signal was incident at the Brewster angle; see Chapter 4. The frequency of

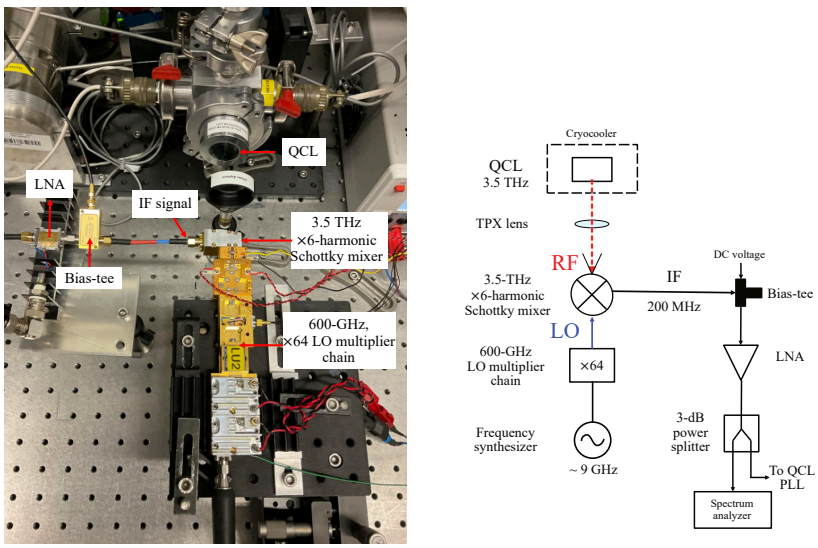

a) b)

Figure 5.2: RF harmonic mixer characterisation. a) A photograph of the measurement setup. The QCLs are placed in a Sterling cryocooler, and the THz beam generated from the QCL is focused on the harmonic mixer using a TPX lens. b) Schematic of the setup.

the QCL was determined with high precision (< 1 MHz) by measuring the absorption of the QCL radiation guided through an absorption cell filled with methanol (CH_3OH) and comparing this spectrum with a reference spectrum of methanol [36].

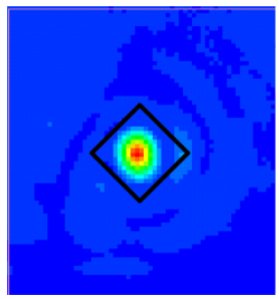

Figure 5.3: Picture of the THz beam profile from 3.5-THz QCL measured using a THz camera. The aperture of the RF diagonal feed horn of the harmonic mixer is indicated as a black line. The measured beam waist was ≈ 170 μm.

5.1.1.1 Conversion loss measurements

The conversion loss of the harmonic mixer was determined by taking the difference between the RF and IF power. Losses in the cables, as well as the connectors and LNA's gain, were considered. The applied DC voltage to the mixer and LO power is varied, and the corresponding conversion loss is plotted as a 2D contour in Fig. 5.4. At low LO power and bias, the conversion is higher than 100 dB. Increasing the LO power or DC bias improves the mixer performance. Conversion null features, caused by the destructive interference of competing mixing products, are also observed [137]. The current safety limit of the diode (1 mA) sets the higher limit on the LO power and DC bias that can be applied to the mixer. Conversion loss contours versus LO power and bias of mixer x6HM35-01 measured at an IF of 200 MHz, an RF of 3.443 THz, and for an LO signal at 573.3 GHz is shown in Fig. 5.4a. The measured RF power at the mixer interface was about -3 dBm, and the available LO power was about 5.6 dBm at 573 GHz. A large-signal harmonic balance simulation was performed to understand the harmonic mixer's performance, and Fig. 5.4b shows the conversion loss contours.

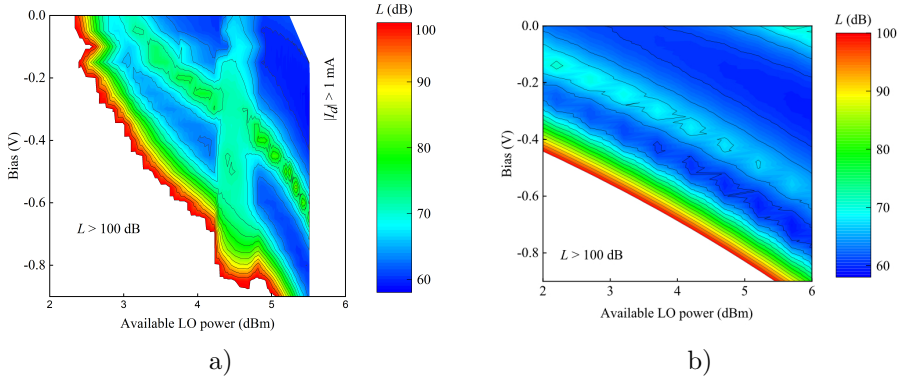

Figure 5.4: 3.5-THz, ×6-harmonic mixer. Conversion loss measurements of mixer x6HM35-01 with Schottky diode of contact area 0.11 μm^2. a) Measurement, b) Simulation.

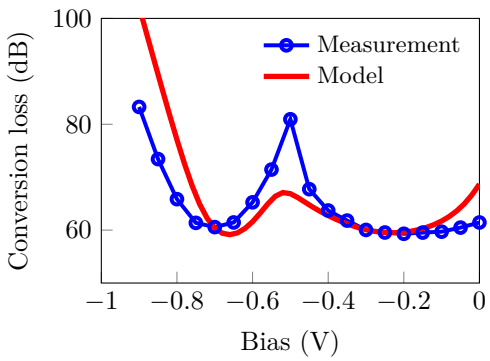

Figure 5.5: Comparison of conversion loss versus bias from measurements of x6HM35-01 and simulation at 5.2 dBm LO power.

The diode model in the simulation was assigned with parameters extracted from the DC measurements ($R_s = 50\ \Omega$, $\eta = 1.24$, $I_s = 9$ fA) and a junction capacitance $C_j = 0.35\ fF$. The simulated conversion loss contours are presented in Fig. 5.4b. A vertical cross-section from the measurements Fig. 5.4a and simulations Fig. 5.4b were taken at a constant LO power 5.2 dBm, and the corresponding cross-section is presented versus bias as shown in Fig. 5.5.

Note: the simulated conversion loss was about 45 dB. As discussed in [Paper B], considering losses in the high-doped buffer resulted in an additional loss of 5 dB. Fig. 5.5 was reproduced by including the losses in the LO access waveguide and IF chain and by assuming an additional loss of 8 dB on the RF side. This loss stems from several factors, which include optical coupling between the QCL beam and the RF diagonal feed horn [63], and conductor loss in the waveguide. However, a significant part of the discrepancy between model and measurement could be due to possible air gaps in the split plane of the mixer block. In addition, at high LO power levels, self-heating effects will also contribute to additional losses [131].

Fig. 5.6a shows the conversion loss versus IF. The synthesiser's input frequency was varied, changing the LO frequency while the RF was kept constant. In the first case, bias was kept constant, and the conversion loss was measured for different intermediate frequencies. In the second case, the bias was varied to obtain optimum conversion loss for each IF. The lowest measured conversion loss was 58 dB at an IF of 10 GHz. Fig. 5.6b shows the beat signal spectrum recorded with a resolution bandwidth of 510 kHz and a video bandwidth of 10 kHz. Both 3.5/4.7-THz QCLs were phase-locked, and the

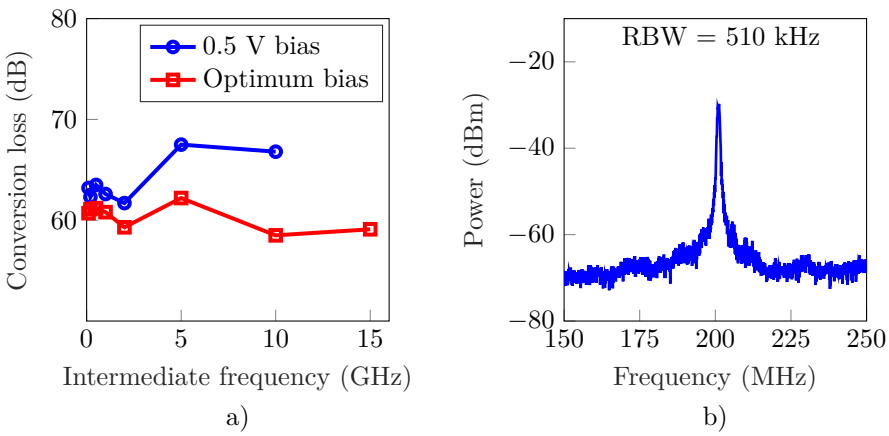

Figure 5.6: 3.5-THz, ×6-harmonic mixer. a) Conversion loss versus IF b) Down-converted IF signal at 200 MHz from the harmonic mixer recorded with a resolution bandwidth of 510 kHz and a video bandwidth of 10 kHz.

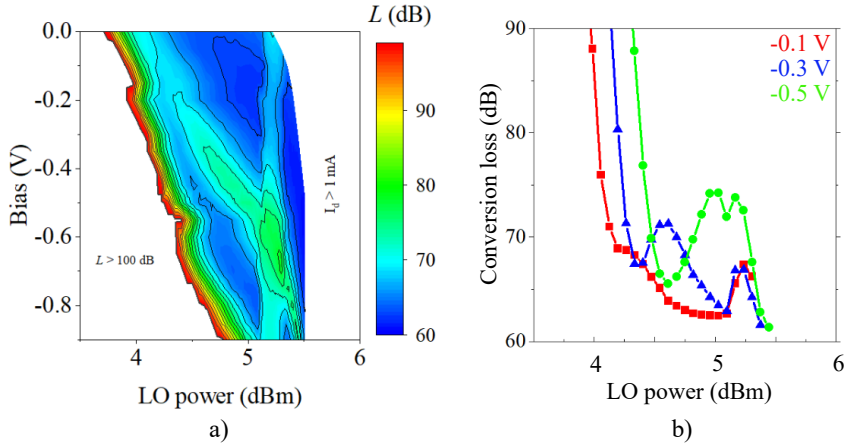

Figure 5.7: 3.5-THz, ×6-harmonic mixer. Conversion loss measurements of mixer x6HM35-02 with Schottky diode of contact area 0.14 μm^2.

experimental results are summarised in [36].

A second mixer was tested (x6HM35-02), which showed similar performance in terms of conversion loss under different LO pump power and bias conditions as shown in Fig.5.7a. Cross-sections along the x-axis are presented in Fig. 5.7b as line plots at different bias conditions showing the conversion loss roll-off at low LO power, followed by several peaks and valleys.

5.1.1.2 Measurement at 4.7 THz

The x6HM35-01 mixer was evaluated at 4.734 THz, and using the 8^{th} harmonic of the LO signal, an IF signal at 3.7 GHz was generated. The measured RF power from 4.734-THz QCL was about −2.2 dBm, and the operating temperature of the QCL was about 50 K. At 592.3 GHz, the available LO power from the multiplier chain is about 4.6 dBm. The DC bias applied to the mixer via bias-tee is varied, and the mixer conversion loss is plotted versus DC bias for a constant LO power, as shown in Fig. 5.8. At 0.4 V, a conversion loss of about 76 dB was measured.

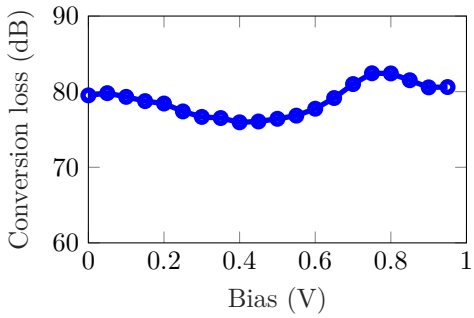

Figure 5.8: Measured conversion loss of x6HM35-01 at 4.734 THz versus DC bias at constant LO power of 4.6 dBm

5.1.2 4.7-THz ×8-harmonic mixer

Compared to the previous mixers with integrated diagonal horns, the new 4.7-THz, ×8-harmonic mixer design incorporates a pyramidal horn to mitigate sensitivity to E-plane misalignment that previously impacted mixer performance [Paper E].

Building on prior experience, an optimised design process was carried out. The radial LO probe was fine-tuned to achieve wideband LO matching with the diode at around 600 GHz [138] as shown in Fig. 3.1. The limited conductivity in the GaAs buffer layer was considered in the EM model. The

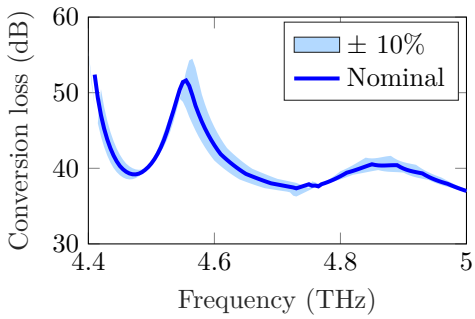

Figure 5.9: 4.7-THz ×8-harmonic mixer. Simulated Conversion loss versus frequency for ±10% variation of junction capacitance.

simulated conversion loss versus frequency for ±10% variation of junction capacitance is plotted in Fig. 5.9. The nominal junction capacitance is about 0.3 fF. The diode model incorporated the following measured DC parameters: $R_s = 75\ \Omega$, $\eta = 1.24$, and $I_s = 2\ fA$. Large-signal simulations were performed at an IF of 200 MHz, with an LO signal around 592 GHz, LO power of 4 dBm, and a bias of 0 V. Note: the available signal power from the multiplier chain at 592 GHz is 4.3 dBm. The conversion loss peak observed at 4.54 THz varies with pump and bias conditions [119]. The micrograph of the ongoing mixer assembly (when this thesis is written) is shown in Fig. 5.10.

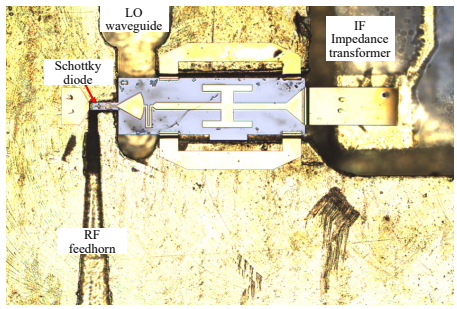

Figure 5.10: 4.7-THz, ×8-harmonic mixer circuitry assembled in the bottom E-plane split block.

5.2 Broadband conversion loss measurements

The lack of wideband, tunable sources at THz frequencies limits the characterisation of mixers over a wide range of frequencies. In Paper [C], the 'three-antenna method' proposed by Beatty in 1967 [134] was adopted to characterise THz harmonic mixers. This experiment features WM-86, ×4-harmonic mixers from VDI with integrated diagonal horns. These mixers have a standard diagonal configuration, approximately 5 mm long with a 0.56 mm × 0.56 mm aperture size, and a beam waist radius (w_o) of 0.21 mm [64]. Each mixer is biased with a constant current of 350 μA and is pumped using WM-380 VDI frequency extenders in the 550–750 GHz range. To perform SSB measurements, a frequency offset is introduced at $f_{LO} + 2f_{IF}$.

As depicted in Fig. 5.11, the mixers were aligned head-to-head rather than in a quasi-optical setup. This alignment approach introduces two main limita-

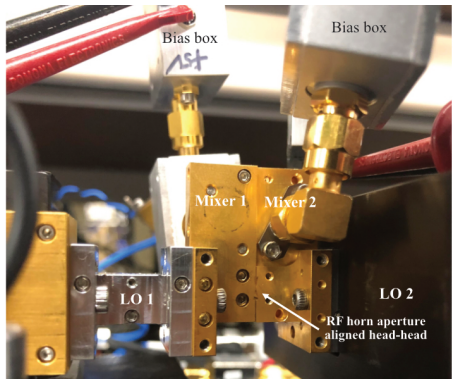

Figure 5.11: Photograph of the experimental setup showing VDI's WM86 mixers with integrated diagonal horn as up and down converter.

tions: a few decibels of coupling loss [63] and the formation of standing waves within the RF chain. Consequently, correcting for systematic errors arising from standing waves between the RF ports becomes difficult. The three mix-

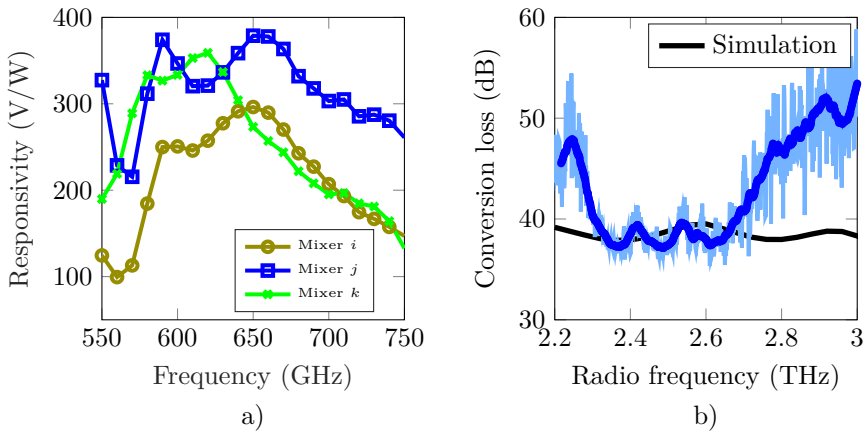

Figure 5.12: WM-86, ×4-harmonic mixers: a) Video responsivity; b) Conversion loss vs. frequency of mixer j. The shaded lines represent raw data, while the smoothed (blue) line is filtered data [Paper C], and the black line is from simulation.

ers were characterised iteratively to determine the conversion loss described in Section 4.2.2 and [Paper C]. This process generates a system of linear equations, which, once solved, yields the conversion loss of each mixer from 2.2 to 3 THz, as depicted in Fig.5.12b. For comparison, a large-signal harmonic balance simulation is included using the following measured DC diode parameters: $R_s = 45\ \Omega$, $\eta = 1.2$, $I_s = 2\ pA$ and $C_j = 0.75\ fF$. The simulation assumes a constant LO pump power of 0.1 mW, resulting in a flat conversion loss response. The video responsivity of the three mixers was measured, showing peak responsivity in the 600–650 GHz range, as shown in Fig. 5.12a. There is a clear correlation between responsivity and conversion loss response, with minimum conversion loss occurring in the 2.4–2.6 THz range, aligning with the peak responsivity.

5.2.1 Validation

Experimental characterisation of three WR-15 sub-harmonic ($\times 2$) mixers from VDI was carried out to validate the three-mixer method. An isolator was used to mitigate the standing waves between the mixers, as shown in Fig. 5.13. The results were compared with the standard single-mixer measurement performed with a calibrated source plotted in [Paper C].

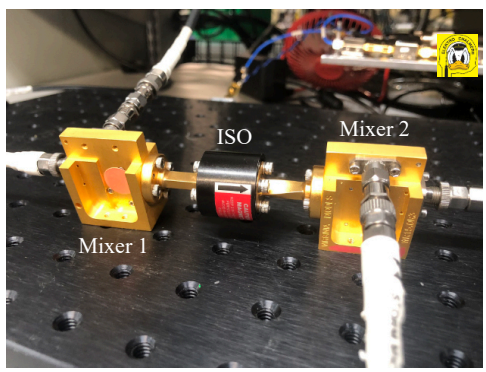

Figure 5.13: Validation using WR-15 VDI sub-harmonic mixers.

5.3 3.5-THz and 4.7-THz fundamental mixers

Realisation of fundamental mixers above 2 THz is challenging due to the high LO power requirements to pump the mixer. The 3D-EM design of both the fundamental mixers is presented in Section 3.17 and [Paper D]. The simulated conversion loss and RF return loss versus frequency are shown in Fig. 5.14. The estimated junction capacitance is 0.35 fF for an anode area of 0.11 μm^2, and the corresponding change in mixer performance for $\pm$10 % variation is presented in Fig. 5.14. The following parameters were used in this simulation: $R_s = 50\ \Omega$, $\eta = 1.25$, and $I_{sat} = 3$ fA, LO power of 0 dBm and DC bias of 0.7 V.

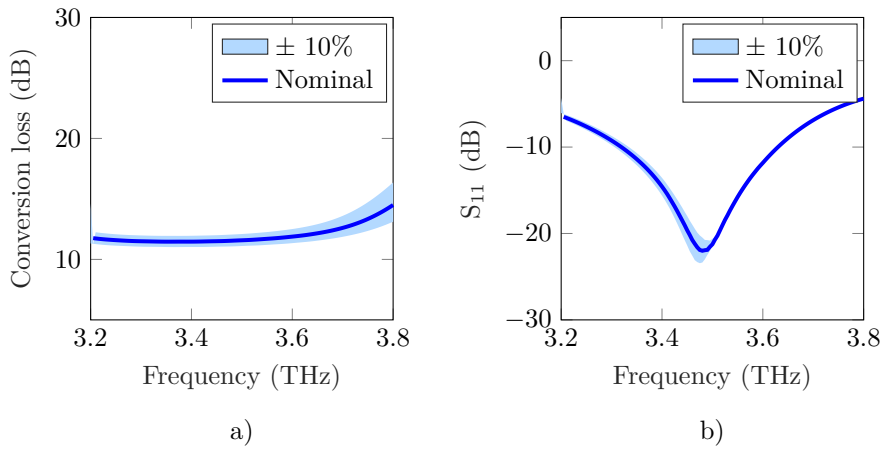

Figure 5.14: 3.5-THz fundamental mixer - Simulated mixer performance for variation of junction capacitance. a) Mixer conversion loss, b) RF return loss.

Fig. 5.15 shows the relative change in the simulated conversion loss of 4.7-THz fundamental mixer as a function of applied DC bias and LO power available to the diode. Losses in the waveguide and horn were excluded. This necessitates the need for providing efficient Gaussian beam coupling to the mixer. The estimated junction capacitance is 0.3 fF for an anode area of 0.1 μm^2. The following parameters were used in this simulation: $R_s = 75\ \Omega$, $\eta = 1.25$, and $I_{sat} = 3$ fA.

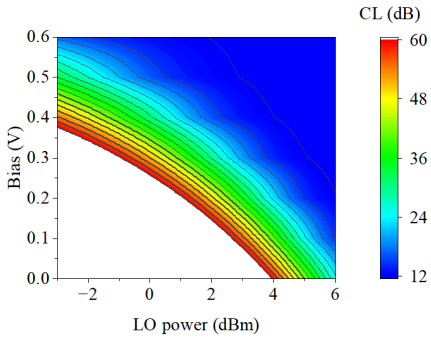

Figure 5.15: 4.7-THz fundamental mixer. Variation of conversion loss with LO power and DC bias.

5.3.1 Sensitivity to assembly variations

To understand the implications of circuit misalignment during assembly, the 4.7-THz fundamental mixer circuit was misaligned by 5 μm as shown in Fig. 3.21. At 4.74-THz, the conversion loss degraded by 6 dB, indicating the importance of achieving good alignment with 1-2 μm tolerance.

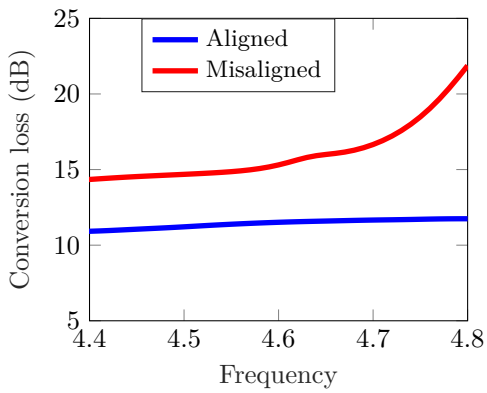

Figure 5.16: 4.7-THz fundamental mixer. Simulated conversion loss versus frequency for perfectly aligned and misaligned mixer circuit in the mixer housing.

5.3.2 Direct detection

The SEM picture of the 3.5-THz fundamental mixer circuit realised on a 2-μm GaAs membrane before being released from the supporting substrate is shown in Fig. 5.17. The general procedure described in Section 5.1 is followed for mixer assembly and functionality verification.

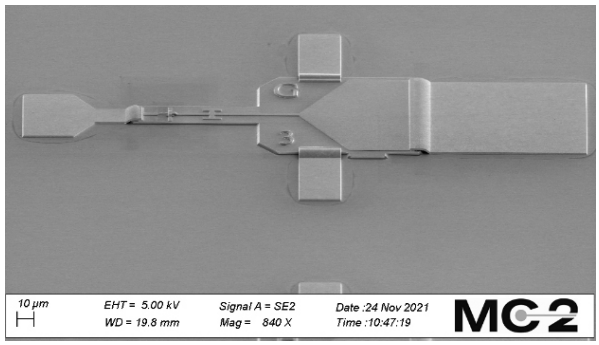

Figure 5.17: SEM picture of the 3.5-THz fundamental mixer circuit on the supporting wafer.

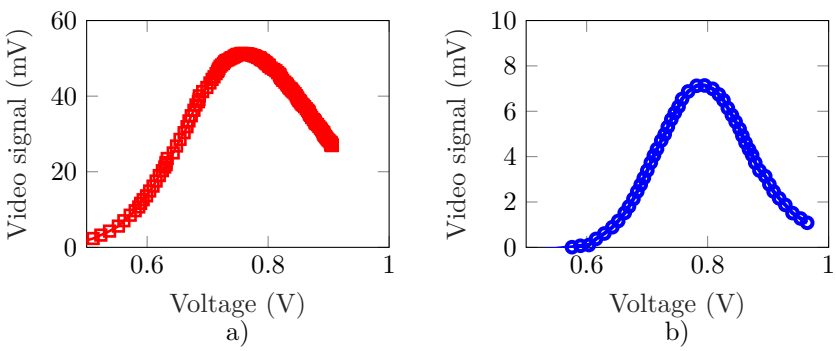

Figure 5.18: Video signal measurements. a) 3.5-THz fundamental mixer b) 4.7-THz fundamental mixer.

The mixer was mounted on a combination of a 3-axis stage with a resolution of 250 μm per revolution and a multi-axis stage from Thor labs, featuring a

tip and tilt resolution of ±5° and a rotation resolution of ±10°. Precise adjustments were made to maximize the video signal response, monitored using an oscilloscope and a lock-in amplifier [139]. Figure 5.18a shows the recorded video signal as a function of the applied DC voltage alongside the diode's corresponding *I-V* response. The current safety limit was set to 1 mA.

5.3.3 Noise temperature measurements

For noise temperature measurements, an off-axis parabolic mirror was used to focus the THz signal from the QCL. The signal was then split using a beam splitter, directing maximum power from the QCL to the fundamental mixer via a Martin-Puplett diplexer, as shown in Fig. 4.6. The remaining part of the signal was routed to the Schottky harmonic mixer for QCL frequency stabilisation. The total path length from the QCL to the fundamental mixer was approximately 80 cm, and the whole setup was purged with nitrogen. The QCL power at the mixer interface, measured with a Thomas Keating power meter, was about 5 mW at 3.5 THz. Preliminary noise temperature measurements carried out by DLR for the 3.5-THz fundamental mixer show a DSB noise temperature of around 140 000 K.

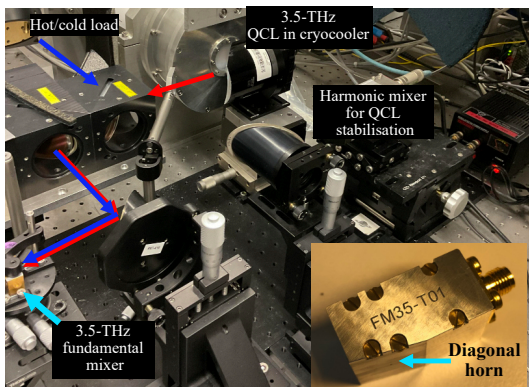

Figure 5.19: 3.5-THz fundamental mixer. Noise temperature measurement setup. The inset shows the 3.5-THz fundamental mixer with an integrated diagonal horn. (Courtesy of DLR).

For the 4.7-THz fundamental mixer, very low video signal response was measured, see Fig. 5.18b; therefore, noise temperature could not be mea-

sured. The discrepancies between measurement and EM simulation were attributed to high losses in the RF chain. Hence, a scaled-down measurement was performed at 470 GHz to quantify the impact of E-plane misalignment on diagonal horns.

5.4 Sensitivity analysis of THz horn antennas

A key challenge in realising components above 2 THz is its sensitivity to machining tolerances even in the order of a few microns. Asymmetry in constructing E-plane split-block components can lead to a detrimental impact on performance, yielding poor Gaussicity in multi-mode feed horns, as shown in Fig. 5.20. The diagonal and pyramidal horn designs are discussed in Chapter 3, and the smooth-walled conical spline horn design is based on [140]. In [Paper E], the effect of E-plane misalignment on THz diagonal horn antennas is experimentally quantified.

5.4.1 Diagonal horn

The diagonal horn's performance relies on the phase and amplitude balance between the two propagation modes TE_{10} and TE_{01}. Consequently, any form of asymmetry within the cross-section, such as that induced by misalignment in the E-plane, can result in different phase velocities for these modes. Consequently, this mismatch leads to a high cross-polarisation component, thereby

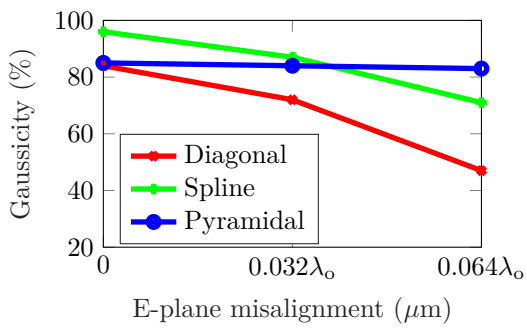

Figure 5.20: Effect of E-plane misalignment on commonly used THz horn antennas.

compromising the antenna's performance [141]. The E-plane misalignment is illustrated in Fig. 5.21. The magnitude of the co- and cross-polarised E-field at the aperture of the horn obtained using Eq. 2.5 is shown in Fig. 5.22. The analytical equation for determining the phase and amplitude imbalance caused by the E-plane misalignment is derived in Paper [E].

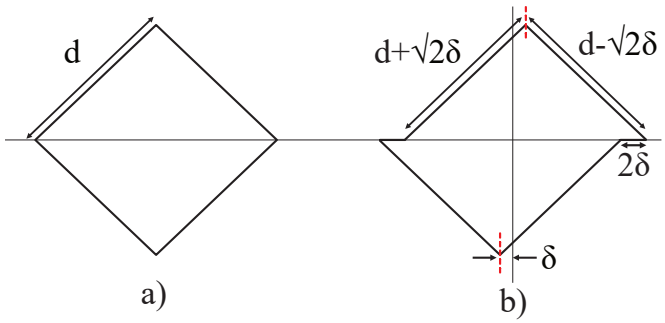

Figure 5.21: Illustration of E-plane misalignment in diagonal horn antennas. a) aligned and b) misaligned case.

A standard WM-570 diagonal horn was designed as described by Johansson and Whyborn [72]. A square aperture with the side, $d = 2.86$ mm, length $L = 15$ mm, and corresponding flare angle $\theta = \tan^{-1}(d/\sqrt{2}L) = 7.7°$ were used. The EM simulation of the horn was carried out by assigning a finite conductive

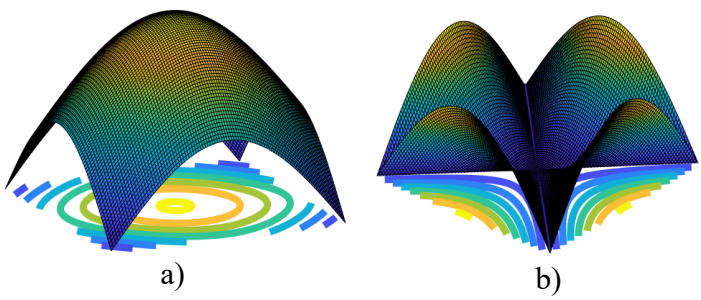

Figure 5.22: Magnitude of the electric field at the aperture of the horn obtained using Eq. 2.5. a) Copolar b) Cross polar.

boundary (aluminium) with electrical conductivity $\sigma = 3.8 \times 10^7$ S/m. A radiation boundary box was placed at the end of the horn to obtain the far-field responses. Simulated directivity is about 21.5 dB, and the E-plane half-power beam width is 13° at 400 GHz.

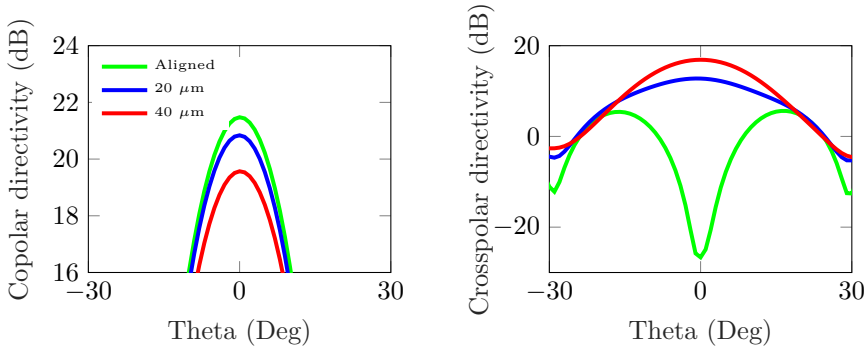

Figure 5.23: Copolar and cross-polar directivity of aligned and misaligned diagonal horn antennas at 400 GHz. a) E-plane ($\phi = 0°$) and b) D-plane ($\phi = 45°$).

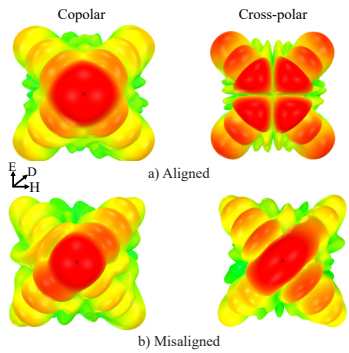

Figure 5.24: 3-D radiation pattern of aligned and misaligned diagonal horn antennas at 400 GHz. a) (Left) Copolar pattern and (Right) Cross-polar pattern of the aligned antenna with a null in the boresight. b) (Left) Copolar pattern and (Right) Cross-polar pattern of the misaligned antenna.

Fig. 5.23 shows the simulated far-field radiation pattern of the co and cross-polar component of the diagonal horn at 400 GHz, respectively, for both aligned and misaligned cases. Fig. 5.23a shows the copolar directivity for the E-plane cut ($\phi = 0°$), and the peak directivity reduces by 2 dB when the antenna is misaligned by 40 μm. In Fig. 5.23b, we see a null in the cross-polar component at boresight as expected for the aligned case [72], [142] and when misaligned, shows an increased cross-polar component at the boresight as shown in Fig. 5.24b.

5.4.1.1 Theoretical analysis

When the split blocks are misaligned, the two corresponding TE modes will have different propagation phase constants (β^+, β^-) and wave impedances, creating an imbalance along the length of the diagonal horn $\frac{E_{10}}{E_{01}} = \sqrt{\Omega} \cdot e^{j\varphi}$.

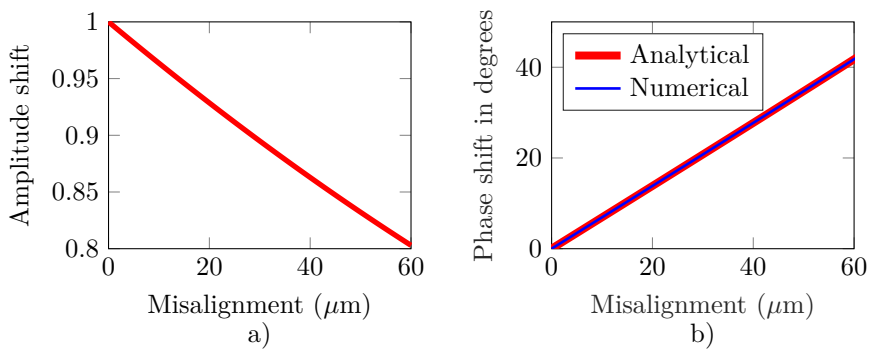

Figure 5.25: Amplitude and phase imbalance in a diagonal horn due to E-plane misalignment.

The phase imbalance between the two modes at the aperture [Paper E] can be expressed as,

$$\varphi = \int_{z_t}^{L} \Big(\beta^+(z) - \beta^-(z) \Big) dz$$

$$= \int_{z_t}^{L} \left[\sqrt{k^2 - \left(\frac{\pi}{z\frac{d}{L} + \frac{\delta}{\sqrt{2}}} \right)^2} - \sqrt{k^2 - \left(\frac{\pi}{z\frac{d}{L} - \frac{\delta}{\sqrt{2}}} \right)^2} \right] dz \qquad (5.1)$$

The amplitude imbalance is estimated based on the assumption that the power imbalance only depends on the ratio of mode impedances at the throat and using the power-voltage characteristic impedance definition, refer [Paper E] for a detailed explanation, the power balance (Ω) is defined as,

$$\Omega = \frac{Z^-(z_t)}{Z^+(z_t)}$$

5.4.1.2 Mechanical design

The horn antenna was realised in an E-plane split aluminium block. A 45° chamfer was implemented on the aperture plane to redirect the reflected signal away from the optical axis.

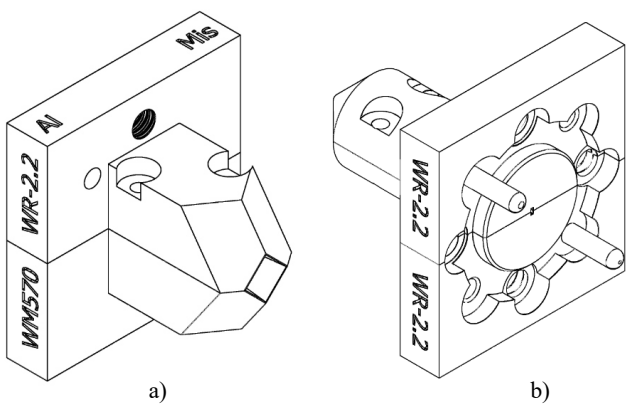

Figure 5.26: CAD model. a) WM-570 diagonal horn with integrated rectangular waveguide, b) UG-387 flange interface of an open-ended waveguide probe.

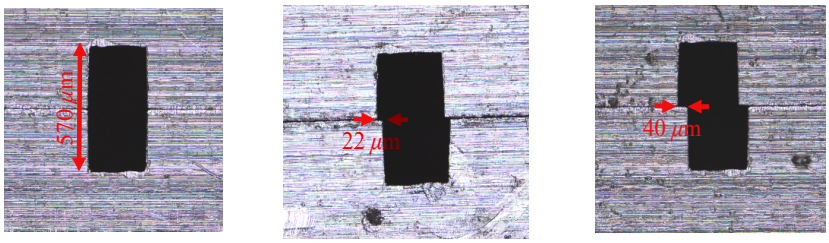

Figure 5.27: Micrograph showing the WM-570 rectangular waveguide integrated with the diagonal horn. a) Perfectly aligned, b) Misaligned by 22 μm and c) Misaligned by 40 μm.

Two rectangular guide structures were incorporated onto the top surface of the split blocks to facilitate accurate alignment. The intentional allowance in tolerance permits controlled sliding of the blocks, thus enabling effortless alignment and misalignment of the split blocks.

5.4.1.3 Near-field horn antenna measurements

The near field antenna measurement setup is shown in Fig. 5.28, consisting of Keysight Vector Network Analyser (VNA) N5242B and WM-570 VDI frequency extenders.

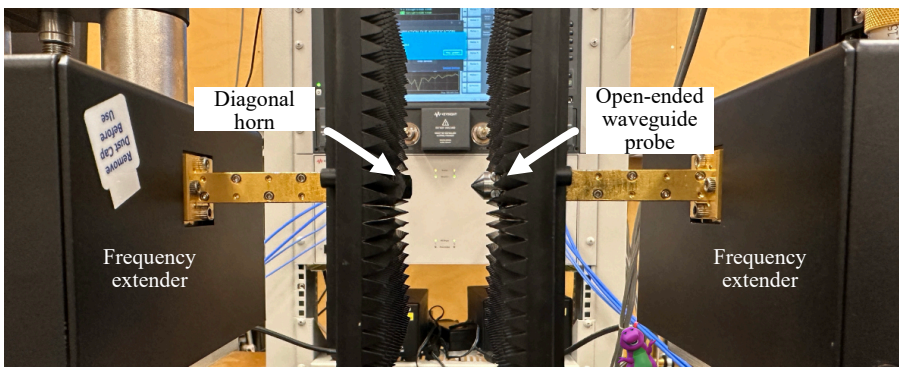

Figure 5.28: Near-field antenna measurement setup.

The antenna under test (AUT) was connected on the left side with extender

1, while the WM-570 open-ended rectangular waveguide was attached to the right side using extender 2, which was mounted on a motorised linear XY stage with a step resolution of 2.5 μm. The measurement protocol is outlined in detail in Paper [E].

The near-field pattern of the diagonal horn was measured, and a standard near-field to far-field transformation technique (NF/FF) [143], [144] was used to compute the antenna's far-field radiation pattern. For cross-polar measurements, a 90° WM-570 VDI waveguide twist was utilised. Fig. 5.29 shows the comparison between simulation and measurement of cross-polar directivity across three scenarios: a) aligned, b) misaligned by 22 μm, and c) misaligned by 40 μm. The simulation and measurement data show strong agreement, and as expected, an increase in the cross-polar component was observed when the antenna was misaligned.

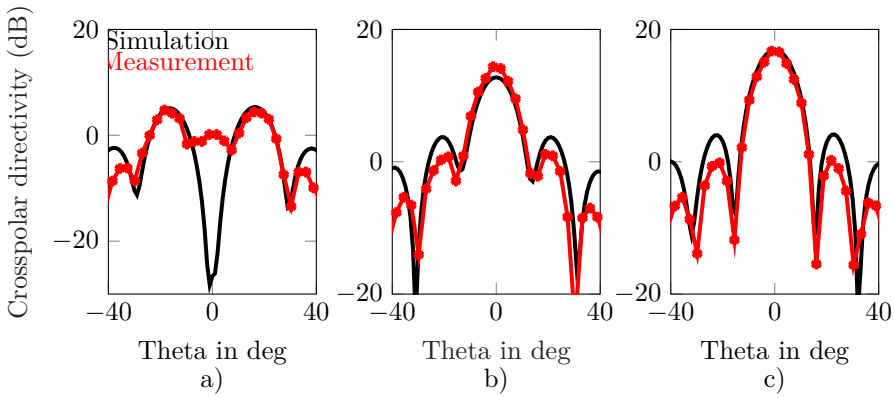

Figure 5.29: Comparison of simulation and measurement of cross-polar directivity in D-plane ($\phi = 45°$) for three cases. a) Aligned, b) Misaligned by 22 μm, and c) Misaligned by 40 μm.

An alternative to the split-block approach is to manufacture horns vertically in a single solid metal block, which may help reduce high cross-polarisation levels caused by lateral misalignment. This was demonstrated by Hammar *et al.* [140] using a custom broach tool to shape the horn profile at 340 GHz.

5.4.2 Pyramidal horn

Fig. 5.30 shows the simulated far-field radiation pattern of the co and cross-polar component of the pyramidal horn at 400 GHz, respectively, for both aligned and misaligned cases. Due to their 'single-mode' operation, pyramidal horns are much less susceptible to E-plane asymmetries [Paper F].

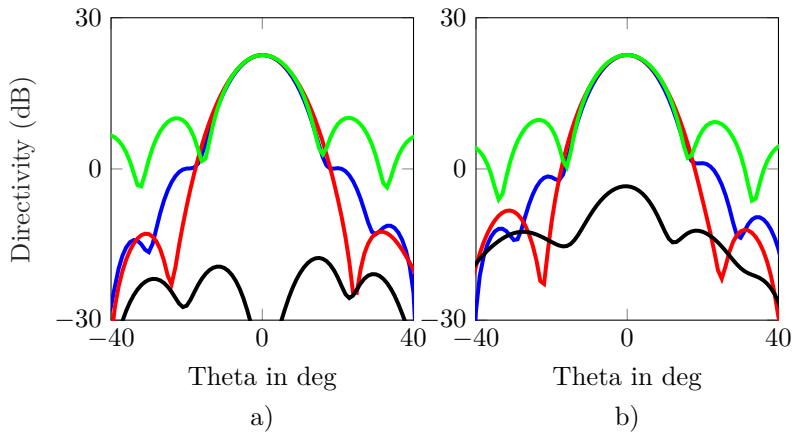

Figure 5.30: Far-field cuts of pyramidal horn. a) Aligned b) Misaligned by 40 μm. Copolar pattern of E-plane (red), H-plane (green), D-plane (blue) and cross-polar pattern in H-plane (black)

Chapter 6

Conclusion and future outlook

The advancement of THz heterodyne receivers capable of resolving emission and absorption lines at THz frequencies with high spectral resolution is critical for probing the composition, chemistry, and distribution of crucial atmospheric constituents. This dissertation has focused on the design and characterisation of THz harmonic and fundamental mixers at 3.5 THz and 4.7 THz. Initially, a comprehensive large-signal analysis was conducted on $\times 4$, $\times 6$, and $\times 8$ harmonic mixers operating between 2-5 THz. The impact of idler terminations (Z- and Y-mixers) on harmonic mixer performance was explored in [Paper A], presenting the corresponding diode embedding impedances at RF and LO frequencies. Based on this, a 3D-EM model of the 3.5-THz, $\times 6$-harmonic mixer was designed, and the critical parameters influencing the mixer performance were studied to evaluate the robustness of the design. The key factors that limit the realisation of mixers at THz frequencies are higher-order propagation modes and substrate loss. To circumvent this problem, the integrated mixer circuits were fabricated on a 2-μm GaAs substrate. Schottky contact with a sub-micron anode area was defined to reduce the junction capacitance. The fabricated mixer circuits were assembled on E-plane split blocks with integrated diagonal horns, and the mixer was pumped by a 600-GHz $\times 64$-cascaded active multiplier chain, resulting in a conversion loss of

about 60 dB. The conversion loss measurements under various pump and bias conditions aligned with simulation results as presented in [Paper B], and the successful phase-locking of both 3.5/4.7-THz QCLs are detailed in [36]. The harmonic mixer was also employed in the laboratory characterisation of QCLs that flew in OSAS-B, the first 4.7-THz heterodyne spectrometer on a stratospheric balloon, in 2022. [145].

However, the lack of wideband and tunable sources presents a significant challenge for characterising mixers across a broad frequency range. An alternative method was proposed to address this, and [Paper C] reports the first experimental demonstration of wideband THz harmonic mixer characterisation. In this study, three WM-86, $\times$4-harmonic mixers from VDI were characterised using an iterative up-down conversion scheme, with conversion loss evaluated between 2.2-3 THz. The design and challenges of realising 3.5 THz and 4.7 THz fundamental mixers are discussed in [Paper D]. The discrepancies between measurements and electromagnetic (EM) simulations were attributed to high losses in the RF chain. A scaled-down experiment was conducted to investigate the impact of E-plane misalignment on a diagonal horn antenna in the WM-570 frequency band (330-500 GHz), as presented in [Paper E]. Based on the results, we optimised the harmonic mixer with an integrated pyramidal horn and the results are summarised in [Paper F].

In the future, it is vital to work on a high-frequency device model to understand various loss mechanisms, including the effect of self-heating. Another critical improvement aspect in future designs is exploring different mixer topologies. For instance, a balanced mixer topology, such as a cross-bar waveguide, is beneficial as it suppresses amplitude-modulated (AM) noise. Investigating low band-gap materials like InGaAs could also help lower the LO power requirements. Alternatively, open-structure mounts with planar antennas integrated with Schottky diodes are an option. A quasi-optical design offers close antenna integration and eliminates significant uncertainties associated with fabricating RF/LO waveguides and horn antennas, which can be particularly challenging at short wavelengths. However, quasi-optical designs have poor Gaussian beam coupling, which must be addressed.

Developing compact, sensitive THz mixers operating at room temperature will pave the way for future satellite or balloon missions to detect atomic oxygen, a critical atmospheric constituent for advancing planetary and atmospheric science research.

Chapter 7

Summary of appended papers

This chapter summarises the appended papers and outlines my contribution to each paper.

Paper A

Effect of Idler Terminations on the Conversion Loss for THz Schottky Diode Harmonic Mixers

This paper investigates the impact of idler terminations on the conversion loss of various harmonic mixers operating within the 2-5 THz range. The study examines the optimum embedding impedances at RF and LO frequencies for different idler configurations: Z-mixers (open termination) and Y-mixers (short termination). The findings indicate that Z-mixer configurations achieve the lowest conversion loss compared to Y-mixers, as the idlers have no power dissipation. However, at higher frequencies, the diode's junction capacitance acts as a short circuit, making the realisation of a pure Z-mixer impractical.
My contribution: Schottky diode modelling: series resistance and junction capacitance, large signal modelling of harmonic mixers in different idler configurations, writing - original draft, review and editing.

Paper B

A 3.5-THz, ×6-Harmonic, Single-Ended Schottky Diode Mixer for Frequency Stabilization of Quantum-Cascade Lasers

This paper presents the design and characterisation of a 3.5-THz, ×6-harmonic mixer. Based on the theoretical study presented in [Paper A], a 3D EM design of the harmonic mixer was carried out. A sensitivity analysis was performed to evaluate the robustness of the design. The integrated harmonic mixer was realised on a 2-μm GaAs substrate and assembled on an E-plane split-block. The harmonic mixer with 0.11 μm^2 Schottky contact area exhibited a conversion loss of about 60 dB and was used in the QCL phase-locking experiment.
My contribution: 3D-EM design of the 3.5-THz, ×6-harmonic mixer, sensitivity analysis, mixer layout for circuit fabrication, CAD drawings of the mixer blocks, quartz, PCB design and assembly. DC measurements, wafer mapping, parameter extraction, experimental verification, data analysis and visualisation, Writing - original draft, review and editing.

Paper C

A Broadband Conversion Loss Measurement Technique for Terahertz Harmonic Mixers

This paper presents the experimental technique for characterising THz harmonic mixers over a wide range of frequencies. Three WM-86 ×4-harmonic mixers from VDI were characterised in an iterative up-and-down conversion scheme, resulting in a linear system of equations. Upon solving it, the conversion loss was estimated from 2.2 to 3 THz.
My contribution: Experimental characterisation of THz harmonic mixers, validation at mm-wave frequencies, data analysis and visualisation, Writing - original draft, review and editing

Paper D

Design and Characterisation of a 3.5-THz Fundamental Schottky mixers

This paper presents the 3D-EM design and characterisation results of a 3.5-THz fundamental Schottky diode mixer.
My contribution: 3D-EM design of the 3.5-THz fundamental mixer, sensitivity analysis, mixer layout for circuit fabrication, CAD drawings of the mixer blocks, quartz, PCB design and assembly. DC measurements, wafer mapping, parameter extraction, video signal measurements, and noise characterisation were carried out by Nick Rothbart (DLR), as well as data analysis and visualisation, Writing - original draft, review, and editing.

Paper E

Impact of E-plane misalignment on THz diagonal horns

This paper quantifies the effect of E-plane misalignment on the widely used THz diagonal horn antenna. The performance of the diagonal horn antenna depends on the phase and amplitude balance of TE_{10} and TE_{01} modes. Asymmetries arising when aligning the two E-plane split blocks can cause mode imbalance, leading to high cross-polarisation levels.
My contribution: 3D-EM design of the diagonal horn, CAD design of the blocks with intentional alignment and misalignment cases and open-ended waveguide probe, near-field radiation pattern measurements, data analysis and visualisation, Writing - original draft, review and editing.

Paper F

4.7-THz Schottky Diode Harmonic Mixer: Design, Fabrication, and Performance Optimisation

Based on papers [B] and [E], the updated design and characterisation of a 4.7-THz, $\times$8-harmonic mixer is presented. The new design has an integrated pyramidal horn, which is not sensitive to E-plane misalignment.

My contribution: 3D-EM design of the 4.7-THz, ×8-harmonic mixer, sensitivity analysis, mixer layout for circuit fabrication, CAD drawings of the mixer blocks, quartz, PCB design and assembly. DC measurements, wafer mapping, parameter extraction, data analysis and visualisation, Writing - original draft, review and editing.

References

[1] P. H. Siegel, "THz Instruments for Space," *IEEE Trans. Antennas Propag.*, vol. 55, no. 11, pp. 2957–2965, Nov. 2007.

[2] D. Farrah, K. E. Smith, D. Ardila, *et al.*, "Review: far-infrared instrumentation and technological development for the next decade," *J. Astron. Telesc. Instrumen. Syst.*, vol. 5, Apr. 2019, Art. no. 020901, DOI: 10.1117/1.jatis.5.2.020901.

[3] R. Voigt, M. Wienold, D. Jayasankar, *et al.*, "High-precision molecular spectroscopy with a phase-locked quantum-cascade laser," in *2024 49th International Conference on Infrared, Millimeter, and Terahertz Waves (IRMMW-THz)*, 2024, pp. 1–2. DOI: 10.1109/IRMMW-THz60956.2024.10697554.

[4] G. J. Stacey, "THz Low Resolution Spectroscopy for Astronomy," *IEEE Transactions on Terahertz Science and Technology*, vol. 1, no. 1, pp. 241–255, 2011. DOI: 10.1109/TTHZ.2011.2159649.

[5] H. Richter, C. Buchbender, R. Güsten, *et al.*, "Direct measurements of atomic oxygen in the mesosphere and lower thermosphere using terahertz heterodyne spectroscopy," *Commun. Earth Environment*, vol. 2, no. 1, Jan. 2021, Art. no. 19, DOI: 10.1038/s43247-020-00084-5.

[6] M. Wienold, A. D. Semenov, E. Dietz, *et al.*, "OSAS-B: A Balloon-Borne Terahertz Spectrometer for Atomic Oxygen in the Upper Atmosphere," *IEEE Transactions on Terahertz Science and Technology*, vol. 14, no. 3, pp. 327–335, 2024. DOI: 10.1109/TTHZ.2024.3363135.

[7] D. L. Wu *et al.*, "THz limb sounder (TLS) for lower thermospheric wind, oxygen density, and temperature," *Journal of Geophysical Research: Space Physics*, vol. 121, no. 7, pp. 7301–7315, Jul. 2016. DOI: 10.1002/2015ja022314.

[8] A. K. Smith, D. R. Marsh, M. G. Mlynczak, and J. C. Mast, "Temporal variations of atomic oxygen in the upper mesosphere from SABER," *Journal of Geophysical Research*, vol. 115, no. D18, Sep. 2010. DOI: 10.1029/2009jd013434.

[9] M. Anderberg, P. Sobis, V. Drakinskiy, *et al.*, "A 183-GHz Schottky Diode Receiver with 4 dB Noise Figure," in *2019 IEEE MTT-S International Microwave Symposium (IMS)*, 2019, pp. 172–175. DOI: 10.1109/MWSYM.2019.8701051.

[10] P. J. Sobis, N. Wadefalk, A. Emrich, and J. Stake, "A broadband, low noise, integrated 340 GHz Schottky diode receiver," *IEEE Microwave and Wireless Components Letters*, vol. 22, no. 7, pp. 366–368, 2012. DOI: 10.1109/LMWC.2012.2202280.

[11] A. Hammar, P. Sobis, V. Drakinskiy, *et al.*, "Low noise 874 GHz receivers for the international submillimetre airborne radiometer (ISMAR)," *Review of Scientific Instruments*, vol. 89, no. 5, p. 055 104, May 2018. DOI: 10.1063/1.5017583.

[12] H. Zhao, V. Drakinskiy, P. Sobis, *et al.*, "Development of a 557 GHz GaAs monolithic membrane-diode mixer," in *2012 International Conference on Indium Phosphide and Related Materials*, IEEE, Aug. 2012. DOI: 10.1109/iciprm.2012.6403330.

[13] B. Thomas, A. Maestrini, and G. Beaudin, "A low-noise fixed-tuned 300-360-GHz sub-harmonic mixer using planar Schottky diodes," *IEEE Microwave and Wireless Components Letters*, vol. 15, no. 12, pp. 865–867, 2005. DOI: 10.1109/LMWC.2005.859992.

[14] J. Treuttel, L. Gatilova, A. Maestrini, *et al.*, "A 520–620-GHz Schottky Receiver Front-End for Planetary Science and Remote Sensing With 1070 K–1500 K DSB Noise Temperature at Room Temperature," *IEEE Transactions on Terahertz Science and Technology*, vol. 6, no. 1, pp. 148–155, 2016. DOI: 10.1109/TTHZ.2015.2496421.

[15] J. Treuttel, L. Gatilova, S. Caroopen, *et al.*, "1200 GHz High Spectral Resolution Receiver Front-End of Submillimeter Wave Instrument for JUpiter ICy Moon Explorer: Part I - RF Performance Optimization for Cryogenic Operation," *IEEE Transactions on Terahertz Science and Technology*, vol. 13, no. 4, pp. 324–336, 2023. DOI: 10.1109/TTHZ.2023.3263623.

[16] M. Gaidis, H. Pickett, C. Smith, S. Martin, R. Smith, and P. Siegel, "A 2.5-THz receiver front end for spaceborne applications," *IEEE Transactions on Microwave Theory and Techniques*, vol. 48, no. 4, pp. 733–739, 2000. DOI: 10.1109/22.841966.

[17] E. Schlecht, J. V. Siles, C. Lee, *et al.*, "Schottky Diode Based 1.2 THz Receivers Operating at Room-Temperature and Below for Planetary Atmospheric Sounding," *IEEE Transactions on Terahertz Science and Technology*, vol. 4, no. 6, pp. 661–669, 2014. DOI: 10.1109/TTHZ.2014.2361621.

[18] J. V. Siles, K. B. Cooper, C. Lee, R. H. Lin, G. Chattopadhyay, and I. Mehdi, "A New Generation of Room-Temperature Frequency-Multiplied Sources With up to 10x Higher Output Power in the 160-GHz–1.6-THz Range," *IEEE Transactions on Terahertz Science and Technology*, vol. 8, no. 6, pp. 596–604, 2018. DOI: 10.1109/TTHZ.2018.2876620.

[19] J. Zmuidzinas and P. Richards, "Superconducting detectors and mixers for millimeter and submillimeter astrophysics," *Proceedings of the IEEE*, vol. 92, no. 10, pp. 1597–1616, 2004. DOI: 10.1109/JPROC.2004.833670.

[20] W. B. J. Hesler and T. Crowe, "Multiplier development for the upper alma local oscillator bands," in *2006 17th Int. Sym. on Space Terahertz Technology (ISSTT)*, 2006.

[21] C. Walker, C. Kulesa, P. Bernasconi, *et al.*, "The Stratospheric THz Observatory (STO)," in *Ground-based and Airborne Telescopes III*, L. M. Stepp, R. Gilmozzi, and H. J. Hall, Eds., International Society for Optics and Photonics, vol. 7733, SPIE, 2010, pp. 264–272. DOI: 10.1117/12.857765.

[22] S. Gulkis, M. Frerking, J. Crovisier, *et al.*, "MIRO: Microwave Instrument for Rosetta Orbiter," *Space Science Reviews*, vol. 128, no. 1-4, pp. 561–597, Nov. 2006. DOI: 10.1007/s11214-006-9032-y.

[23] U. Frisk, M. Hagström, J. Ala-Laurinaho, *et al.*, "The Odin satellite," *Astronomy & Astrophysics*, vol. 402, no. 3, pp. L27–L34, Apr. 2003. DOI: 10.1051/0004-6361:20030335.

[24] F. Maiwald, E. Schlecht, A. Maestrini, *et al.*, "Terahertz frequency multiplier chains based on planar Schottky diodes," in *Millimeter and Submillimeter Detectors for Astronomy*, T. G. Phillips and J. Zmuidzinas, Eds., International Society for Optics and Photonics, vol. 4855, SPIE, 2003, pp. 447–458. DOI: 10.1117/12.459355.

[25] B. Thomas, M. Brandt, A. Walber, *et al.*, "Submillimetre-wave receiver developments for ICI onboard MetOP-SG and ice cloud remote sensing instruments," in *2012 IEEE International Geoscience and Remote Sensing Symposium*, 2012, pp. 1278–1281. DOI: 10.1109/IGARSS.2012.6351306.

[26] D. Cuadrado-Calle *et al.*, "Solid-state diode technology for millimeter and submillimeter-wave remote sensing applications: Current status and future trends," 2022. DOI: 10.1109/MMM.2022.3155031.

[27] A. Betz and R. T. Boreiko, "A Practical Schottky Mixer for 5 THz (Part II)," *Softwaretechnik-trends*, p. 503, 1996.

[28] R. T. Boreiko and A. Betz, "Heterodyne Spectroscopy of the 63 μm O I Line in M42," *The Astrophysical Journal*, vol. 464, 1996.

[29] T. W. Crowe, R. J. Mattauch, H. P. Röser, W. L. Bishop, W. C. B. Peatman, and X. Liu, "GaAs Schottky diodes for THz mixing applications," *Proc. IEEE*, vol. 80, no. 11, pp. 1827–1841, Nov. 1992. DOI: 10.1109/5.175258.

[30] W. L. Bishop, T. W. Crowe, R. J. Mattauch, and P. H. Ostdiek, "Planar Schottky barrier mixer diodes for space applications at submillimeter wavelengths," *Microwave and Optical Technology Letters*, vol. 4, no. 1, pp. 44–49, Jan. 1991. DOI: 10.1002/mop.4650040113.

[31] P. H. Siegel *et al.*, "2.5-THz GaAs monolithic membrane-diode mixer," *IEEE Trans. Microw. Theory Techn.*, vol. 47, no. 5, pp. 596–604, May 1999. DOI: 10.1109/22.763161.

[32] M. Gaidis *et al.*, "A 2.5 THz receiver front-end for spaceborne applications," in *1998 IEEE Sixth International Conference on Terahertz Electronics Proceedings. THZ 98. (Cat. No.98EX171)*, IEEE, 2000. DOI: 10.1109/thz.1998.731652.

[33] G. Scalari *et al.*, "Far-infrared ($\lambda \simeq 87\,\mu$m) bound-to-continuum quantum-cascade lasers operating up to 90 k," *Applied Physics Letters*, vol. 82, pp. 3165–3167, 2003.

[34] L. Schrottke, X. Lü, B. Röben, *et al.*, "High-performance GaAs/AlAs terahertz quantum-cascade lasers for spectroscopic applications," *IEEE Trans. THz Sci. Technol.*, vol. 10, no. 2, pp. 133–140, Mar. 2020. DOI: 10.1109/TTHZ.2019.2957456.

[35] H.-W. Hübers, H. Richter, and M. Wienold, "High-resolution terahertz spectroscopy with quantum-cascade lasers," *Journal of Applied Physics*, vol. 125, no. 15, p. 151 401, Apr. 2019. DOI: 10.1063/1.5084105.

[36] H. Richter, N. Rothbart, M. Wienold, *et al.*, "Phase Locking of Quantum-Cascade Lasers Operating Around 3.5 and 4.7 THz With a Schottky-Diode Harmonic Mixer," *IEEE Transactions on Terahertz Science and Technology*, vol. 14, no. 3, pp. 346–353, 2024. DOI: 10.1109/TTHZ.2024.3385379.

[37] A. Cowley and H. Sorensen, "Quantitative comparison of solid-state microwave detectors," *IEEE Transactions on Microwave Theory and Techniques*, vol. 14, no. 12, pp. 588–602, 1966. DOI: 10.1109/TMTT.1966.1126337.

[38] H. Friis, "Noise figures of radio receivers," *Proceedings of the IRE*, vol. 32, no. 7, pp. 419–422, 1944. DOI: 10.1109/JRPROC.1944.232049.

[39] R. H. Dicke, "The Measurement of Thermal Radiation at Microwave Frequencies," *Review of Scientific Instruments*, vol. 17, no. 7, pp. 268–275, Jul. 1946. DOI: 10.1063/1.1770483.

[40] D. Allan, "Statistics of atomic frequency standards," *Proceedings of the IEEE*, vol. 54, no. 2, pp. 221–230, 1966. DOI: 10.1109/PROC.1966.4634.

[41] J. Kooi, "Advanced receivers for submillimeter and far infrared astronomy," English, Ph.D. dissertation, University of Groningen, 2008.

[42] J. Stake, A. Malko, T. Bryllert, and J. Vukusic, "Status and Prospects of High-Power Heterostructure Barrier Varactor Frequency Multipliers," *Proceedings of the IEEE*, vol. 105, no. 6, pp. 1008–1019, 2017. DOI: 10.1109/JPROC.2016.2646761.

[43] J. Vukusic, T. Bryllert, T. Arezoo Emadi, M. Sadeghi, and J. Stake, "A 0.2-W Heterostructure Barrier Varactor Frequency Tripler at 113 GHz," *IEEE Electron Device Letters*, vol. 28, no. 5, pp. 340–342, 2007. DOI: 10.1109/LED.2007.895376.

[44] T. Bryllert, A. Malko, J. Vukusic, and J. Stake, "A 175 GHz HBV Frequency Quintupler With 60 mW Output Power," *IEEE Microwave and Wireless Components Letters*, vol. 22, no. 2, pp. 76–78, 2012. DOI: 10.1109/LMWC.2011.2181494.

[45] J. Vukusic, T. Bryllert, Ø. Olsen, J. Hanning, and J. Stake, "Monolithic HBV-based 282-GHz tripler with 31-mw output power," *IEEE Electron Device Letters*, vol. 33, no. 6, pp. 800–802, 2012. DOI: 10.1109/LED.2012.2191385.

[46] A. Malko, T. Bryllert, J. Vukusic, and J. Stake, "A 474 GHz HBV frequency quintupler integrated on a 20 μm thick silicon substrate," *IEEE Transactions on Terahertz Science and Technology*, vol. 5, no. 1, pp. 85–91, 2015. DOI: 10.1109/TTHZ.2014.2378793.

[47] R. Dahlbäck, J. Vukusic, R. M. Weikle II, and J. Stake, "A tunable 240–290 GHz waveguide enclosed 2-D grid HBV frequency tripler," *IEEE Transactions on Terahertz Science and Technology*, vol. 6, no. 3, pp. 503–509, 2016. DOI: 10.1109/TTHZ.2016.2545519.

[48] E. Bryerton, S. Retzloff, and J. Hesler, "High-power submillimeter wave solid-state sources," in *2019 12th Global Symposium on Millimeter Waves (GSMM)*, 2019, pp. 29–31. DOI: 10.1109/GSMM.2019.8797648.

[49] D. Moro-Melgar, V. L. Rubio, O. Cojocari, I. Opra, and A. Negrus, "600 – 900 GHz Frequency Sources with up to 4 mW Output Power based on Flip-Chip Schottky Barrier Diodes Technology," in *2022 47th International Conference on Infrared, Millimeter and Terahertz Waves (IRMMW-THz)*, 2022, pp. 1–1. DOI: 10.1109/IRMMW-THz50927.2022.9895924.

[50] Y. Koyama, Y. Kitazawa, K. Yukimasa, *et al.*, "A high-power terahertz source over 10 mw at 0.45 thz using an active antenna array with integrated patch antennas and resonant-tunneling diodes," *IEEE Transactions on Terahertz Science and Technology*, vol. 12, no. 5, pp. 510–519, 2022. DOI: 10.1109/TTHZ.2022.3180492.

[51] S. Suzuki, M. Shiraishi, H. Shibayama, and M. Asada, "High-power operation of terahertz oscillators with resonant tunneling diodes using impedance-matched antennas and array configuration," *IEEE Journal of Selected Topics in Quantum Electronics*, vol. 19, no. 1, 2013. DOI: 10.1109/JSTQE.2012.2215017.

[52] K. Kasagi, S. Suzuki, and M. Asada, "Large-scale array of resonant-tunneling-diode terahertz oscillators for high output power at 1 THz," *Journal of Applied Physics*, vol. 125, no. 15, Mar. 2019, 151601. DOI: 10.1063/1.5051007.

[53] H. Richter, M. Greiner-Bär, S. G. Pavlov, *et al.*, "A compact, continuous-wave terahertz source based on a quantum-cascade laser and a miniature cryocooler," *Opt. Express*, vol. 18, no. 10, pp. 10 177–10 187, 2010. DOI: 10.1364/OE.18.010177.

[54] S. Kumar, B. S. Williams, S. Kohen, Q. Hu, and J. L. Reno, "Continuous-wave operation of terahertz quantum-cascade lasers above liquid-nitrogen temperature," *Applied Physics Letters*, vol. 84, no. 14, pp. 2494–2496, Apr. 2004. DOI: 10.1063/1.1695099.

[55] S. Kumar, B. S. Williams, Q. Qin, A. M. Lee, Q. Hu, and J. L. Reno, "Surface-emitting distributed feedback terahertz quantum-cascade lasers in metal-metal waveguides," *Opt. Express*, vol. 15, no. 1, pp. 113–128, 2007. DOI: 10.1364/OE.15.000113.

[56] Pütz, P., Honingh, C. E., Jacobs, K., Justen, M., Schultz, M., and Stutzki, J., "Terahertz hot electron bolometer waveguide mixers for GREAT," *A&A*, vol. 542, p. L2, 2012. DOI: 10.1051/0004-6361/201218916.

[57] H.-W. Hübers, H. Richter, R. Eichholz, *et al.*, "Heterodyne spectroscopy of frequency instabilities in terahertz quantum-cascade lasers induced by optical feedback," *IEEE Journal of Selected Topics in Quantum Electronics*, vol. 23, no. 4, pp. 1–6, 2017. DOI: 10.1109/JSTQE.2017.2684078.

[58] K. Akiyama, A. Alberdi, W. Alef, *et al.*, "First M87 Event Horizon Telescope Results. VI. The Shadow and Mass of the Central Black Hole," *The Astrophysical Journal Letters*, vol. 875, no. 1, p. L6, Apr. 2019. DOI: 10.3847/2041-8213/ab1141.

[59] T. J. Reck *et al.*, "Design of a 2.5 THz Schottky-Diode Fourth-Harmonic Mixer," *IEEE Trans. THz Sci. Technol.*, pp. 580–586, 2023. DOI: 10.1109/TTHZ.2023.3307566.

[60] B. N. Ellison, A. Valavanis, O. Auriacombe, *et al.*, "3.5 THz quantum-cascade laser emission from dual diagonal feedhorns," *International Journal of Microwave and Wireless Technologies*, vol. 11, no. 9, pp. 909–917, May 2019. DOI: 10.1017/s175907871900028x.

[61] C. A. Balanis, *Antenna theory: analysis and design*. Wiley-Interscience, 2005.

[62] H. Kogelnik and T. Li, "Laser beams and resonators," *Appl. Opt.*, vol. 5, no. 10, pp. 1550–1567, Oct. 1966. DOI: 10.1364/AO.5.001550.

[63] P. F. Goldsmith, "Quasi-optical techniques," *Proc. IEEE*, vol. 80, no. 11, pp. 1729–1747, Nov. 1992.

[64] J. F. Johansson, "A Comparison of Some Feed Types," in *Multi-Feed Systems for Radio Telescopes*, D. T. Emerson and J. M. Payne, Eds., ser. Astronomical Society of the Pacific Conference Series, vol. 75, Jan. 1995, pp. 82–89.

[65] P. Clarricoats and A. Olver, *Corrugated horns for microwave antennas*. IEEE Electromagnetic Wave Series, 1984.

[66] R. Wylde, "Millimetre-wave Gaussian beam-mode optics and corrugated feed horns," *IEE Proceedings H Microwaves, Optics and Antennas*, vol. 131, no. 4, p. 258, 1984. DOI: 10.1049/ip-h-1.1984.0053.

[67] P. Potter, J. P. L. (U.S.), U. S. N. Aeronautics, and S. Administration, *A New Horn Antenna with Suppressed Sidelobes and Equal Bandwidths* (JPL technical report). Jet Propulsion Laboratory, California Institute of Technology, 1963.

[68] K. K. Davis, J. L. Kloosterman, C. Groppi, J. H. Kawamura, and M. Underhill, "Micromachined integrated waveguide transformers in thz pickett–potter feedhorn blocks," *IEEE Transactions on Terahertz Science and Technology*, vol. 7, no. 6, pp. 649–656, 2017. DOI: 10.1109/TTHZ.2017.2760103.

[69] A. King, "The Radiation Characteristics of Conical Horn Antennas," *Proceedings of the IRE*, vol. 38, no. 3, pp. 249–251, 1950. DOI: 10.1109/JRPROC.1950.230734.

[70] A. Love, "The diagonal horn antenna," *Microwave Journal*, pp. 117–122, 1962.

[71] E. Muehldorf, "The phase center of horn antennas," *IEEE Transactions on Antennas and Propagation*, vol. 18, no. 6, pp. 753–760, Nov. 1970, DOI: 10.1109/tap.1970.1139799. DOI: 10.1109/tap.1970.1139799.

[72] J. Johansson and N. D. Whyborn, "The diagonal horn as a sub-millimeter wave antenna," *IEEE Transactions on Microwave Theory and Techniques*, 1992. DOI: 10.1109/22.137380.

[73] A. A. M. Saleh, "Theory of resistive mixers," Ph.D. dissertation, Dept. Elect. Eng., MIT, Cambridge, MA, USA, 1970.

[74] S.Maas, *Nonlinear microwave and RF circuits. Artech House, Inc.* 2003.

[75] N. R. Erickson and T. M. Goyette, "Terahertz Schottky-diode balanced mixers," in *Terahertz Technology and Applications II*, K. J. Linden, L. P. Sadwick, and C. M. O'Sullivan, Eds., International Society for Optics and Photonics, vol. 7215, SPIE, 2009, pp. 41–45. DOI: 10.1117/12.807505.

[76] M. Cohn, J. Degenford, and B. Newman, "Harmonic mixing with an antiparallel diode pair," *IEEE Transactions on Microwave Theory and Techniques*, vol. 23, no. 8, pp. 667–673, 1975. DOI: 10.1109/TMTT.1975.1128646.

[77] R. Bauer, M. Cohn, J. Cotton, and R. Packard, "Millimeter wave semiconductor diode detectors, mixers, and frequency multipliers," *Proceedings of the IEEE*, vol. 54, no. 4, pp. 595–605, 1966. DOI: 10.1109/PROC.1966.4779.

[78] N. Erickson, "Low-noise submillimeter receivers using single-diode harmonic mixers," *Proceedings of the IEEE*, vol. 80, no. 11, pp. 1721–1728, 1992. DOI: 10.1109/5.175251.

[79] H. J. Gibson, A. Walber, R. Zimmerman, B. Alderman, and O. Cojocari, "Harmonic Mixers for VNA extenders to 900GHz," in *2010 21th Int. Sym. on Space Terahertz Technology (ISSTT)*, 2010.

[80] R. J. Gilmore and M. B. Steer, "Nonlinear circuit analysis using the method of harmonic balance—a review of the art. part i. introductory concepts," *International Journal of Microwave and Millimeter-Wave Computer-Aided Engineering*, vol. 1, no. 1, pp. 22–37, 1991. DOI: 10.1002/mmce.4570010104.

[81] K. Braun, "On the current conduction in metal sulphides (title translated from german into english," *Ann. Phys. chem.*, vol. 153, 1874. DOI: 10.1002/andp.18752291207.

[82] E. Eastwood, "Marconi: His Wireless Telegraphy and the Modern World," *Journal of the Royal Society of Arts*, vol. 122, no. 5217, pp. 599–611, 1974.

[83] J. Bose, "Detector for electrical disturbances patent," *Proceedings of the IEEE*, vol. 86, no. 1, pp. 229–234, 1998. DOI: 10.1109/JPROC.1998.658774.

[84] W. Schottky, "Halbleitertheorie der Sperrschicht," *Naturwissenschaften*, vol. 26, no. 52, pp. 843–843, Dec. 1938. DOI: 10.1007/BF01774216.

[85] V. Rideout, "A review of the theory, technology and applications of metal-semiconductor rectifiers," *Thin Solid Films*, vol. 48, no. 3, pp. 261–291, Feb. 1978. DOI: 10.1016/0040-6090(78)90007-x.

[86] A. M. Cowley and S. M. Sze, "Surface states and barrier height of metal-semiconductor systems," *Journal of Applied Physics*, vol. 36, no. 10, pp. 3212–3220, Oct. 1965. DOI: 10.1063/1.1702952.

[87] W. Mönch, "On the physics of metal-semiconductor interfaces," *Reports on Progress in Physics*, vol. 53, no. 3, pp. 221–278, Mar. 1990. DOI: 10.1088/0034-4885/53/3/001.

[88] D. Young and J. Irvin, "Millimeter frequency conversion using Au-n-type GaAs Schottky barrier epitaxial diodes with a novel contacting technique," *Proceedings of the IEEE*, vol. 53, no. 12, pp. 2130–2131, 1965. DOI: 10.1109/PROC.1965.4511.

[89] V. Rideout, "A review of the theory and technology for ohmic contacts to group III-V compound semiconductors," *Solid-State Electronics*, vol. 18, no. 6, pp. 541–550, Jun. 1975. DOI: 10.1016/0038-1101(75)90031-3.

[90] D. Pardo, J. Grajal, and S. Pérez, "Nonequilibrium transport in GaAs Schottky mixers at 2.5 THz," *Journal of Physics: Conference Series*, vol. 647, p. 012 038, Oct. 2015. DOI: 10.1088/1742-6596/647/1/012038.

[91] P. Penfield and R. Rafuse, *Varactor applications*. MIT press, 1962.

[92] A. Maestrini, B. Thomas, H. Wang, *et al.*, "Schottky diode-based terahertz frequency multipliers and mixers," *Comptes Rendus Physique*, vol. 11, no. 7-8, pp. 480–495, Aug. 2010. DOI: 10.1016/j.crhy.2010.05.002.

[93] E. Carlson, M. Schneider, and T. McMaster, "Subharmonically pumped millimeter-wave mixers," *IEEE Transactions on Microwave Theory and Techniques*, vol. 26, no. 10, pp. 706–715, 1978. DOI: 10.1109/TMTT.1978.1129474.

[94] W. Bishop, E. Meiburg, R. Mattauch, T. Crowe, and L. Poli, "A micron-thickness, planar Schottky diode chip for terahertz applications with theoretical minimum parasitic capacitance," in *IEEE International Digest on Microwave Symposium*, 1990, 1305–1308 vol.3. DOI: 10.1109/MWSYM.1990.99818.

[95] P. Siegel, R. Dengler, I. Mehdi, *et al.*, "Measurements on a 215-GHz subharmonically pumped waveguide mixer using planar back-to-back air-bridge Schottky diodes," *IEEE Transactions on Microwave Theory and Techniques*, vol. 41, no. 11, pp. 1913–1921, 1993. DOI: 10.1109/22.273416.

[96] V. Drakinskiy, P. Sobis, H. Zhao, T. Bryllert, and J. Stake, "Terahertz GaAs Schottky diode mixer and multiplier MIC's based on e-beam technology," in *2013 International Conference on Indium Phosphide and Related Materials (IPRM)*, May 2013, pp. 1–2. DOI: 10.1109/ICIPRM.2013.6562606.

[97] O. H. Richardson, "The emission of electricity from hot bodies," *Nature*, vol. 98, no. 2452, pp. 146–146, Oct. 1916. DOI: 10.1038/098146a0.

[98] H. A. Bethe, "Theory of the boundary layer of crystal rectifiers," 1991.

[99] J. Louhi, "The capacitance of a small circular Schottky diode for submillimeter wavelengths," *IEEE Microw. Guided Wave Lett.*, vol. 4, no. 4, pp. 107–108, Apr. 1994. DOI: 10.1109/75.282574.

[100] D. Moro-Melgar, A. Maestrini, J. Treuttel, *et al.*, "Monte carlo study of 2-D capacitance fringing effects in GaAs planar Schottky diodes," *IEEE Transactions on Electron Devices*, vol. 63, no. 10, pp. 3900–3907, 2016. DOI: 10.1109/TED.2016.2601341.

[101] K. S. Champlin *et al.*, "Cutoff frequency of submillimeter Schottky-barrier diodes," *IEEE Trans. Microw. Theory Techn.*, vol. 26, no. 1, pp. 31–34, Jan. 1978. DOI: 10.1109/TMTT.1978.1129302.

[102] L. E. Dickens, "Spreading resistance as a function of frequency," *IEEE Trans. Microw. Theory Techn.*, vol. 15, no. 2, pp. 101–109, Feb. 1967. DOI: 10.1109/TMTT.1967.1126383.

[103] K. Bhaumik, B. Gelmont, R. Mattauch, and M. Shur, "Series impedance of GaAs planar schottky diodes operated to 500 GHz," *IEEE Transactions on Microwave Theory and Techniques*, vol. 40, no. 5, pp. 880–885, 1992. DOI: 10.1109/22.137393.

[104] E. Kolberg, T. Tolmunen, M. Frerking, and J. East, "Current saturation in submillimeter-wave varactors," *IEEE Transactions on Microwave Theory and Techniques*, vol. 40, no. 5, pp. 831–838, 1992. DOI: 10.1109/22.137387.

[105] H. Murrmann and D. Widmann, "Current crowding on metal contacts to planar devices," *IEEE Transactions on Electron Devices*, vol. 16, no. 12, pp. 1022–1024, 1969. DOI: 10.1109/T-ED.1969.16904.

[106] J. Johnson, "Thermal agitation of electricity in conductors," *Phys. Rev.*, vol. 32, no. 1, pp. 97–109, 1928.

[107] H. Nyquist, "Thermal agitation of electric charge in conductors," *Phy. Rev.*, vol. 32, no. 1, pp. 110–113, 1928.

[108] A. V. Der Ziel, "Theory of shot noise in junction diodes and junction transistors," *Proceedings of the IRE*, vol. 43, no. 11, pp. 1639–1646, 1955. DOI: 10.1109/JRPROC.1955.277990.

[109] H. Zirath, "High-frequency noise and current-voltage characteristics of mm-wave platinum $n - n + -$GaAs schottky barrier diodes," vol. 60, no. 4, pp. 1399–1407, Aug. 1986. DOI: 10.1063/1.337317.

[110] S. Adachi, *Properties of group-IV, III-V and II-VI semiconductors*. John Wiley and Sons, 2005.

[111] E. D. Palik, "Gallium arsenide (GaAs)," in *Handbook of Optical Constants of Solids*, E. D. Palik, Ed., Boston, MA, USA: Academic Press, 1985, pp. 429–443. DOI: 10.1016/B978-0-08-054721-3.50020-4.

[112] M. Sotoodeh *et al.*, "Empirical low-field mobility model for iii–v compounds applicable in device simulation codes," *Journal of Applied Physics*, vol. 87, no. 6, pp. 2890–2900, 2000. DOI: 10.1063/1.372274.

[113] J. Hesler, W. Hall, T. Crowe, *et al.*, "Fixed-tuned submillimeter wavelength waveguide mixers using planar schottky-barrier diodes," *IEEE Transactions on Microwave Theory and Techniques*, vol. 45, no. 5, pp. 653–658, 1997. DOI: 10.1109/22.575581.

[114] S. Cherednichenko, V. Drakinskiy, T. Berg, P. Khosropanah, and E. Kollberg, "Hot-electron bolometer terahertz mixers for the Herschel Space Observatory," *Review of Scientific Instruments*, vol. 79, no. 3, p. 034 501, Mar. 2008. DOI: 10.1063/1.2890099.

[115] D. Büchel, P. Pütz, K. Jacobs, *et al.*, "4.7-THz Superconducting Hot Electron Bolometer Waveguide Mixer," *IEEE Transactions on Terahertz Science and Technology*, vol. 5, no. 2, pp. 207–214, 2015. DOI: 10.1109/TTHZ.2014.2382434.

[116] D. Jayasankar, V. Drakinskiy, P. Sobis, and J. Stake, "Development of supra-THz Schottky diode harmonic mixers," pp. 1–2, 2021. DOI: 10.1109/IRMMW-THz50926.2021.9567206.

[117] A. R. Kerr, "Elements for e-plane split-block waveguide circuits," 2001.

[118] J. Hesler, "Planar schottky diodes in submillimeter-wavelength waveguide receivers," English, Ph.D. dissertation, University of Virginia, 1996.

[119] J. Hesler, D. Kurtz, and R. Feinsaugle, "The cause of conversion nulls for single-diode harmonic mixers," *IEEE Microwave and Guided Wave Letters*, vol. 9, no. 12, pp. 532–534, 1999. DOI: 10.1109/75.819422.

[120] S. A. Schelkunoff, "Impedance concept in wave guides," *Quarterly of Applied Mathematics*, vol. 2, no. 1, pp. 1–15, 1944.

[121] T. C. Edwards, *Foundations for Microstrip Circuit Design*. New York: John Wiley & Sons, 1985.

[122] D. Pozar, *Microwave Engineering, 4th Edition*. Wiley, 2011.

[123] P. J. Sobis, N. Wadefalk, A. Emrich, and J. Stake, "A Broadband, Low Noise, Integrated 340 GHz Schottky Diode Receiver," *IEEE Microwave and Wireless Components Letters*, vol. 22, no. 7, pp. 366–368, 2012. DOI: 10.1109/LMWC.2012.2202280.

[124] J. F. Johansson *et al.*, "The diagonal horn as a sub-millimeter wave antenna," *IEEE Trans. Microw. Theory Techn.*, vol. 40, no. 5, pp. 795–800, May 1992. DOI: 10.1109/22.137380.

[125] E. D. Smith, F. Szidarovszky, W. J. Karnavas, and A. T. Bahill, "Sensitivity analysis, a powerful system validation technique," *Open Cybern. Syst. J.*, vol. 2, pp. 39–56, Jan. 2008. DOI: 10.2174/1874110x00802010039.

[126] D. Jayasankar, V. Drakinskiy, P. Sobis, and J. Stake, "A 4.7-thz fundamental schottky diode mixer," in *2022 47th International Conference on Infrared, Millimeter and Terahertz Waves (IRMMW-THz)*, 2022, pp. 1–2. DOI: 10.1109/IRMMW-THz50927.2022.9895685.

[127] J. Stake, L. Dillner, S. Jones, *et al.*, "Effects of self-heating on planar heterostructure barrier varactor diodes," *IEEE Transactions on Electron Devices*, vol. 45, no. 11, pp. 2298–2303, 1998. DOI: 10.1109/16.726644.

[128] S. K. Cheung and N. W. Cheung, "Extraction of Schottky diode parameters from forward current-voltage characteristics," *Applied Physics Letters*, vol. 49, no. 2, pp. 85–87, Jul. 1986. DOI: 10.1063/1.97359.

[129] M. Missous *et al.*, "On the Richardson constant of intimate metal-GaAs Schottky barriers," *Semiconductor Science and Technology*, vol. 7, no. 2, pp. 218–221, Feb. 1992. DOI: 10.1088/0268-1242/7/2/007.

[130] A. Kelly, "Fundamental limits on conversion loss of double sideband resistive mixers," *IEEE Transactions on Microwave Theory and Techniques*, vol. 25, no. 11, pp. 867–869, 1977. DOI: 10.1109/TMTT.1977.1129233.

[131] A. Y. Tang, E. Schlecht, R. Lin, *et al.*, "Electro-thermal model for multi-anode Schottky diode multipliers," *IEEE Trans. THz Sci. Technol.*, vol. 2, no. 3, pp. 290–298, May 2012. DOI: 10.1109/TTHZ.2012.2189913.

[132] Z. Popovic *et al.*, "THz Metrology and Instrumentation," *IEEE Transactions on Terahertz Science and Technology*, vol. 1, no. 1, pp. 133–144, 2011. DOI: 10.1109/TTHZ.2011.2159553.

[133] N. Erickson, "A fast and sensitive submillimeter waveguide power meter," in *1999 10th Int. Sym. on Space Terahertz Technology (ISSTT)*, 1999.

[134] R. Beatty, "Discussion of errors in gain measurements of standard electromagnetic horns," *NBS, Boulder, Colo., Tech. Note 351*, 1967.

[135] A. Kreisler *et al.*, "Parameters influencing far infrared video detection with submicron-size Schottky diodes," *International Journal of Infrared and Millimeter Waves*, vol. 5, no. 4, pp. 559–584, Apr. 1984. DOI: 10.1007/bf01010152.

[136] "IEEE Standard for Rectangular Metallic Waveguides and Their Interfaces for Frequencies of 110 GHz and Above–Part 1: Frequency Bands and Waveguide Dimensions," *IEEE Std 1785.1-2012*, pp. 1–22, Mar. 2013. DOI: 10.1109/IEEESTD.2013.6471987.

[137] R. Feinäugle, H.-W. Hübers, H. P. Röser, and J. L. Hesler, "On the effect of IF power nulls in Schottky diode harmonic mixers," *IEEE Trans. Microw. Theory Techn.*, vol. 50, no. 1, pp. 134–142, Jan. 2002. DOI: 10.1109/22.981257.

[138] C. Risacher *et al.*, "Waveguide-to-microstrip transition with integrated bias-T," *IEEE Microwave and Wireless Components Letters*, vol. 13, no. 7, pp. 262–264, 2003. DOI: 10.1109/LMWC.2003.815182.

[139] H.-W. Hübers *et al.*, "Video detection and mixing performance of GaAs Schottky-barrier diodes at 30 THz and comparison with metal-insulator-metal diodes," *Journal of Applied Physics*, vol. 75, no. 8, pp. 4243–4248, Apr. 1994. DOI: 10.1063/1.355980.

[140] A. Hammar, Y. Karandikar, P. Forsberg, A. Emrich, and J. Stake, "A 340 GHz high Gaussicity smooth spline horn antenna for the STEAMR instrument," in *2014 IEEE Antennas and Propagation Society International Symposium (APSURSI)*, DOI: 10.1109/APS.2014.6904655, 2014, pp. 649–650. DOI: 10.1109/APS.2014.6904655.

[141] S. Withington and J. Murphy, "Analysis of diagonal horns through Gaussian-Hermite modes," *IEEE Transactions on Antennas and Propagation*, vol. 40, no. 2, pp. 198–206, 1992, DOI: 10.1109/8.127404. DOI: 10.1109/8.127404.

[142] A. Ludwig, "The definition of cross polarization," *IEEE Transactions on Antennas and Propagation*, vol. 21, no. 1, pp. 116–119, 1973. DOI: 10.1109/TAP.1973.1140406.

[143] A. Yaghjian, "An overview of near-field antenna measurements," *IEEE Transactions on Antennas and Propagation*, 1986. DOI: 10.1109/TAP.1986.1143727.

[144] H. J. Gibson, B. Thomas, L. Rolo, M. C. Wiedner, A. E. Maestrini, and P. de Maagt, "A novel spline-profile diagonal horn suitable for integration into thz split-block components," *IEEE Transactions on Terahertz Science and Technology*, vol. 7, no. 6, pp. 657–663, 2017. DOI: 10.1109/TTHZ.2017.2752423.

[145] M. Wienold, A. D. Semenov, E. Dietz, *et al.*, "OSAS-B: A Balloon-Borne Terahertz Spectrometer for Atomic Oxygen in the Upper Atmosphere," *IEEE Transactions on Terahertz Science and Technology*, vol. 14, no. 3, pp. 327–335, 2024. DOI: 10.1109/TTHZ.2024.3363135.